COMPUTER SIMULATION OF THE HUMAN ERYTHROCYTE CYTOSKELETON

by

Seng Kee Boey

B.Sc. Simon Fraser University 1990

M.Sc. McMaster University 1992

THESIS SUBMITTED IN PARTIAL FULFILLMENT OF THE REQUIREMENTS FOR THE DEGREE OF DOCTOR OF PHILOSOPHY IN THE DEPARTMENT OF PHYSICS

Simon Fraser University

April 1997

Approval

Name: Seng Kee Boey

Degree: Doctor of Philosophy

Title of Thesis: Computer Simulation of the Human Erythrocyte Cytoskeleton

Examining Committee:

Prof. J. C. Irwin
Chair

Prof. David Boal
Senior Supervisor

Prof. Michael Plischke

Prof. Michael Wortis

Prof. Jenifer Thewalt
Internal Examiner

Dr. Mike Saxton
External Examiner
University of California, Davis

Abstract

The human erythrocyte cytoskeleton, a scaffolding of proteins attached to the cytoplasmic side of the bilayer, is modeled as a triangulated network of polymer chains, in which the coupling to the bilayer can be either at the polymer chains' midpoints, the network sixfold junction complexes or both. The geometrical and elastic response of the model network is determined through computer simulation by applying both isotropic and anisotropic stresses. Near zero stress, the model cytoskeleton behaves much like a two-dimensional network of springs, while at large tensions it can be described as a network of equilateral triangles with square-well interactions between the nodes.

Elastically, the model cytoskeleton which has membrane linkages at both the chains' midpoints and sixfold junction complexes is the stiffest. This difference, in comparison to cases where the membrane linkage is either at the chains' midpoints or at the sixfold junction complexes, is as much as a factor of 2.5 for the out-of-plane elastic moduli, namely the volume compression modulus and the transverse Young's modulus. The effect of a precompression built into the rest-state of the cytoskeleton has also been investigated and found not to significantly affect the predicted elastic properties of the cytoskeleton.

The model has also been used to probe the effect of the cytoskeleton in constraining the membrane proteins to localised regions. The simulation method used to probe this effect is similar to the protein

dragging techniques used in single-particle tracking experiments. Large proteins are found to be mostly confined in a local region (or corral) due to steric interactions, a typical corral radius being about 20 nm. Small proteins on the other hand, are able to slip past polymer chains and are stopped mostly by the membrane attachment sites of the cytoskeleton. We interpret the mean-free path of directed protein motion as a two-dimensional scattering problem and the extracted in-plane diameters of the attachment sites are found to range from 12 nm to 32 nm, depending on the type of membrane linkage mechanism present in the model.

I would like to dedicate this work to

my wife Shirley

and

my son Nathan

Acknowledgements

I would like to thank my supervisor Professor David Boal for his invaluable insight into my research, for his open door approach which made learning much more accessible, and also for the many times he has help me out of difficult situations (especially those involving use of campus computers). I would also like to thank him for his assistance in my job search: writing of reference letters and bringing to my attention any potential research position openings.

Dennis Discher, Professor Boal's former postdoctoral fellow, has been an invaluable part of my research. I deeply appreciate those many stimulating discussions we had and the many suggestions he made during my research time at SFU. I also thank him for making time available for me to answer the questions I had in my research.

I would like to next thank Professor Plischke for helping me in understanding the approach to solving some of the questions I had. He has also provided valuable suggestions to my research during our soft condensed matter meetings. I also thank Professor Wortis for a mind-boggling time on our road trip to the Biophysics conference at the University of Washington, which helped me to look into certain aspects of my research more carefully.

I would like to thank my friend Julian Shillcock for the many stimulating research discussions we had in our computer lab and also over coffee breaks.

Much thanks also goes to Sharon Beever and Audrey Reid for their excellent administrative support and for just being my friends.

I thank my wife, most of all, for being so supportive and patient, during these four and a half years.

This work is supported in part through postgraduate fellowships provided by the Natural Sciences and Engineering Research Council of Canada and by Simon Fraser University.

Contents

List of tables

List of figures

Chapter 1
INTRODUCTION

1.1 The human erythrocyte

The human erythrocyte has long intrigued biophysicists, cell biologists and biochemists by its relatively simple geometry and its fascinating mechanical and physiological properties. There is still much to be understood about the pronounced resilience of the erythrocyte as it undergoes marked deformation in the circulatory system (see Fig. 1.1) and rapidly recovers its resting shape once the

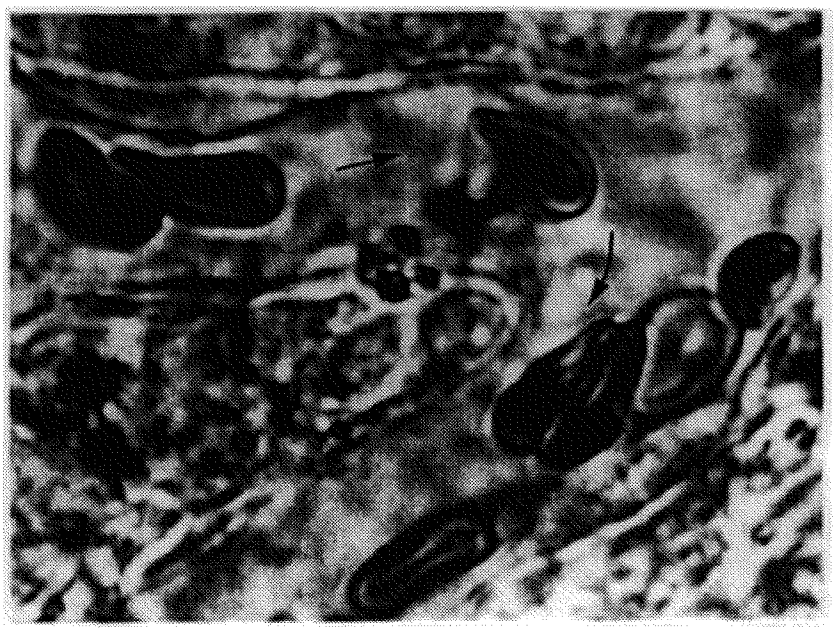

Fig. 1.1 Micrograph of human erythrocytes moving through small blood vessels. Notice the deformations that each red cell undergoes. Arrows show direction of blood flow. The cells in the image have a diameter of approximately 10 microns. (Steck 1989)

shear stress is removed. These large deformations have been observed by many investigators. Krogh (Krogh, 1959) observes that mammalian red cells in 4-5 μm capillaries can achieve lengths more than double the normal, undeformed diameter of the cell of 8 μm. The life span of a normal human red cell is approximately 120 days during which time it passes through the heart roughly 200,000 times (Steck, 1989). The human erythrocytes arise from stem cells located in the bone marrow and are missing the nucleus which is pinched off enroute in the erythrocyte's journey from the stem cells into the bloodstream. The shape of a normal red cell is biconcave (see Fig. 1.2) and about one third of its interior volume is occupied by hemoglobin.

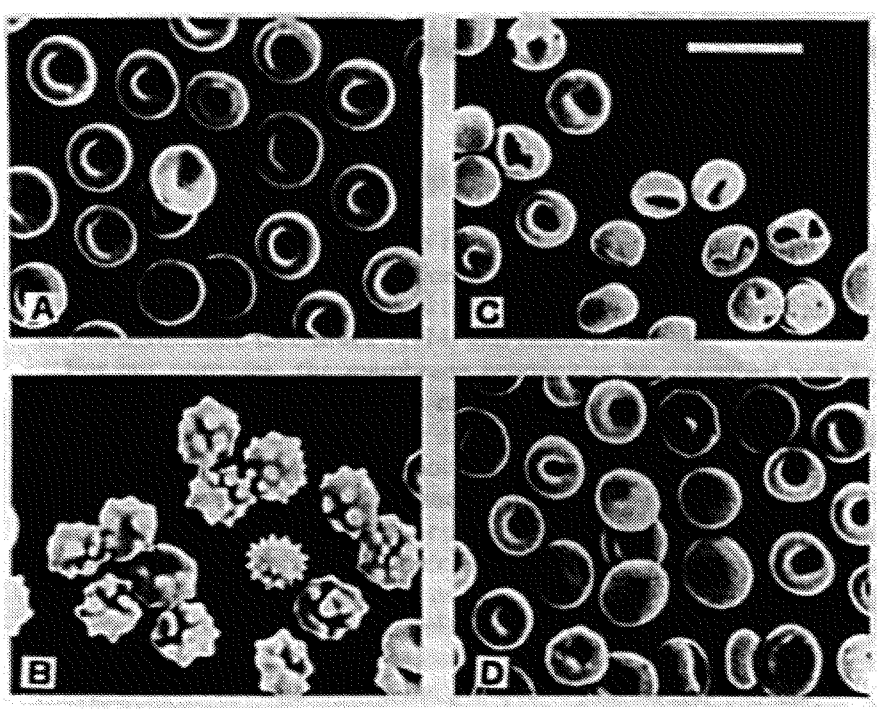

Fig. 1.2 (A) Normal red cells. (B) Echinocytes. (C) Cells depleted of 37% of their cholesterol, leading to invaginations (stomatocytes). (D) Restoration of biconcave shape of cells in (C) treated with lysolecithin. Calibration bar in (c) is 10 μm. (Steck, 1989)

The red cell has an average membrane area of $\approx$ 135 μm^2 and a cytoplasmic volume of approximately 94 μm^3; it can swell to a volume of about 160 μm^3.

The plasma membrane of a red cell can be described as a lipid bilayer in which is associated with a diverse number of different proteins. The bilayer provides solute impermeability to the membrane. The lipids that make up the bilayer are amphiphilic structures, that is, a lipid has both a hydrophobic (water insoluble) tail and a hydrophilic (water soluble) head. The lipids are asymmetrically distributed in the two monolayers that make up the bilayer. The outer monolayer is made up mostly of lipids which are zwitterions, principally phosphatidylcholine (PC) and sphingomyelin (SM); while the cytoplasmic surface is rich in anionic lipids such as phosphatidylserine (PS) and phosphatidylethanolamine (PE). The PC, PS and PE lipids consist of two hydrocarbon chains (hydrophobic tails) linked through a glycerol to a polar head group (hydrophilic head). The SM lipid, on the other hand, has a serine link instead of glycerol. The red cell structure is highly stable, due to the fact that lipids may spontaneously form closed structures in an aqueous environment.

Analysis of the red cell membrane by sodium dodecyl sulfate-polyacrylamide gel electrophoresis (SDS-PAGE, for an explanation of this technique, see Gennis, 1989) has shown that the red cell membrane contains a number of species of proteins, most of which have been characterized (Fairbanks, Steck and Wallach, 1971).

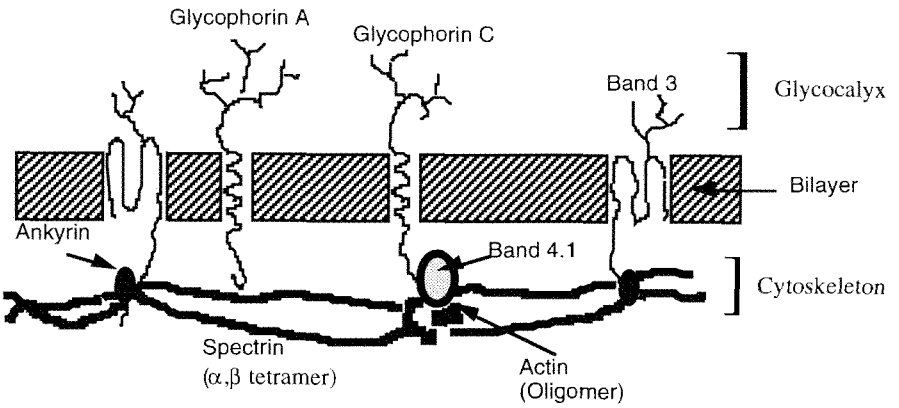

(A)

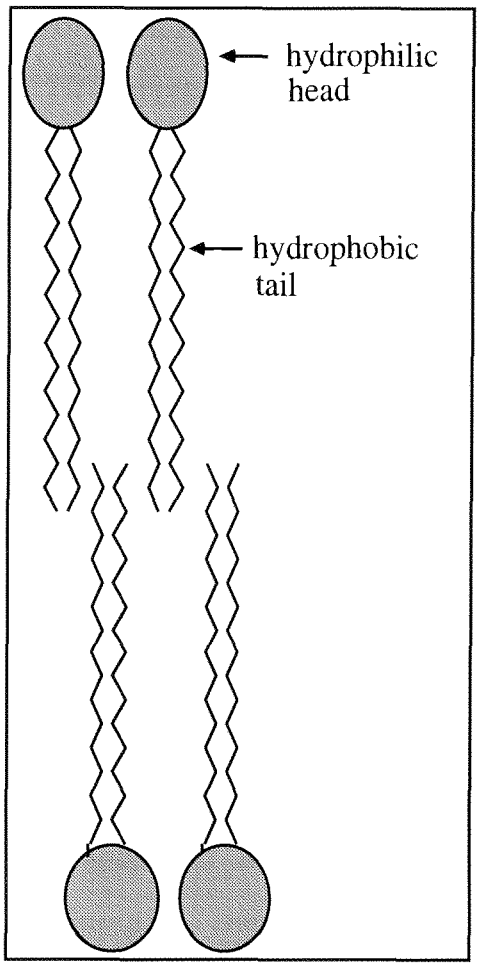

(B)

Fig. 1.3 (A) A schematic diagram of the red cell plasma membrane. (B) A section of the bilayer consisting of dual chain lipid molecules, whose head groups are short chains.

These proteins are divided into two general groups: integral and peripheral proteins. The integral proteins, such as band 3 and glycophorin A, pass through the membrane and are tightly bound to the membrane through hydrophobic interactions with lipids in the bilayer. In a typical red cell, there are approximately 10^6 copies of band 3. Peripheral proteins, on the other hand, are bound to one face of the membrane by noncovalent interactions with other proteins. Spectrin, actin and band 4.1 are typical examples of peripheral proteins and they form most of the membrane skeleton. There are approximately 2 x 10^5 copies of spectrin monomers, 2 x 10^5 copies of actin and 2 x 10^5 copies of band 4.1 in a typical red cell. (See Fig. 1.3). The durability of the red cell is attributed to the extensive reinforcement provided by a scaffolding network of these peripheral proteins (Steck, 1989).

The mechanical behavior of the erythrocyte membrane has been studied extensively (Evans, 1973; Waugh and Evans, 1979; Zilker *et al.*, 1992), yielding elastic parameters that are manifestations of the molecular composition and organization of the plasma membrane. Numerous studies have shown that the protein spectrin plays a crucial role in determining the mechanical properties of the membrane (Branton *et al.*, 1981) and also in controlling the lateral mobility of integral membrane proteins (Sheetz, 1983) by forming a meshwork at the cytoplasmic (or interior) side of the membrane lipid bilayer. The diffusion of proteins within the membrane (Kusumi *et al.*, 1993; Saxton, 1995) is thought to be affected by the cytoskeleton through the formation of domains

where some proteins are corralled for a significant amount of time.

1.2 Membrane cytoskeleton

It has been well established that the proteins, spectrin, actin and band 4.1, are the major components of the human erythrocyte membrane skeleton (Steck, 1989; see Fig. 1.4). The two spectrin

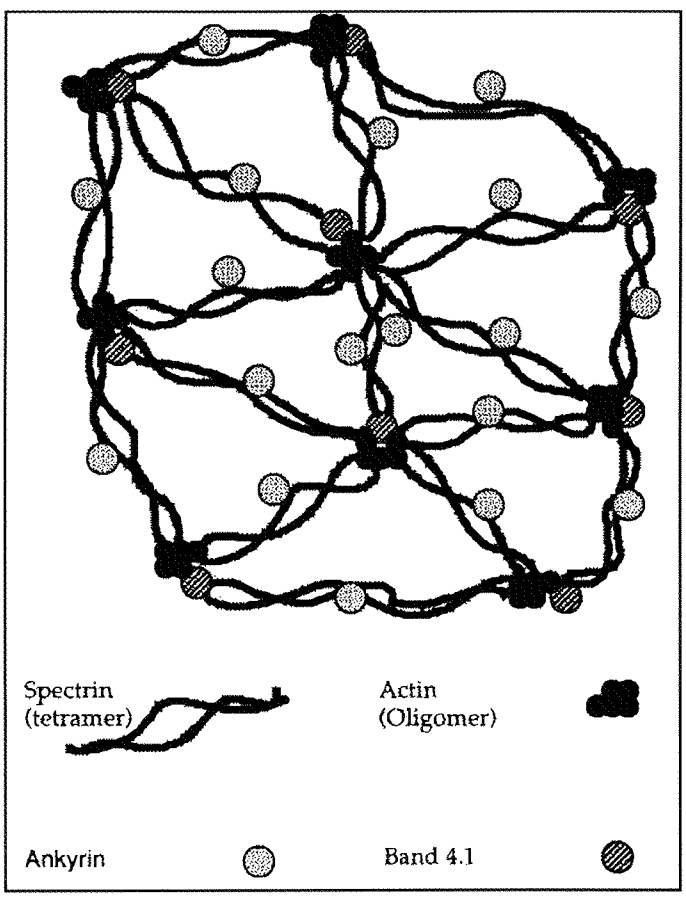

Fig. 1.4 A schematic diagram of the red cell cytoskeleton. Ankyrin and band 4.1 are proteins that are directly or loosely attached to the cytoskeleton and the bilayer.

chains α and β are ≅ 250000 and 220000 daltons in molecular weight, respectively, associated side by side, forming a dimer. Experimental evidence (Speicher, 1986) seems to suggest that each α and β chain is organized into 18 to 20 independently folded domains, each containing 106 residues (amino acids). The dimers associate head-to-head to form $(\alpha\beta)_2$ tetramers, with a contour length of approximately 200 nm (~ 3 nm in diameter). In its native conformation, the spectrin tetramer has an end-to-end displacement of 76 nm, which is about one-third of its contour length. The two tail-ends of these tetramers are associated with actin filaments to form a junction complex (stabilized by the protein band 4.1). On the average, there are six spectrin tetramers joining at the junction complexes, giving rise to the mean sixfold connectivity observed in red cells (see Fig. 1.4; Byers and Branton, 1985; Liu *et al.*, 1987). Experimental evidence suggests that the protein ankyrin links the membrane skeleton through specific transbilayer proteins like band 3. The complete picture of how the skeleton attaches itself to the bilayer, both statically and dynamically, remains to be fully understood.

1.3 Elasticity of the red cell membrane

In recent years, the elasticity of the erythrocyte has been analyzed extensively, and it has been suggested that the resistance to both area dilation and bending of the plasma membrane is borne by the lipid bilayer (Evans and Skalak, 1980). However, the bilayer is

basically a surface fluid and, thus, contributes very little to the extensional elasticity of unswollen (flaccid biconcave shape) red cells. The spectrin network attached to the bilayer is suggested to be primarily responsible for bearing this extensional rigidity of the red cell membrane (Mohandas and Evans, 1994), and this extensional elasticity is the major restoring force for a red cell after it undergoes a large deformation during its route through the blood system (Evans, 1973; Evans and Hochmuth, 1978). This suggestion follows from experimental evidence that: (1) Spectrin has been shown to behave like a highly flexible filament which can be drawn linear or collapsed into a compact form (Bennett, 1985; Elgsaeter *et. al.*, 1986). The intact cytoskeleton was also shown to be capable of sustaining numerous cycles of extensions and contractions of the erythrocyte by varying the pH of the buffer in which it was suspended (Johnson *et al.*, 1980; Lange *et al.*, 1982). (2) Murine (mouse) cells congenitally devoid of spectrin have been found to be rather inelastic (Schmid-Schonbein *et al.*, 1986). (3) There is direct correlation between the modulus of extensional elasticity and the spectrin content of red cells from patients with hereditary hemolytic anemias (Waugh and Agre, 1988). In these experiments, the erythrocyte shear modulus decreases by 30-40% when the ratio of the density of spectrin molecules taken with respect to the density of band 3 molecules present in the red cell plasma membrane decreases by a factor of 2.

Numerous experiments have been carried out to probe the elastic properties of the red cell plasma membrane. Micropipette aspiration of red cells (Waugh & Evans, 1979) can be used to

measure elastic parameters such as bending, area compression and shear moduli. Typically, the red cells are sucked into a micropipette via a suction pressure applied externally (see Fig. 1.5). The length of the red cell inside the micropipette is measured as a function of the suction pressure. The density profile of a spectrin network can also be studied in these experiments via fluorescent microscopy. In these particular microscopy experiments, the cytoskeleton network is subject to a variety of stresses, including simple shear, pure shear and isotropic dilation (Discher *et al.*, 1994).

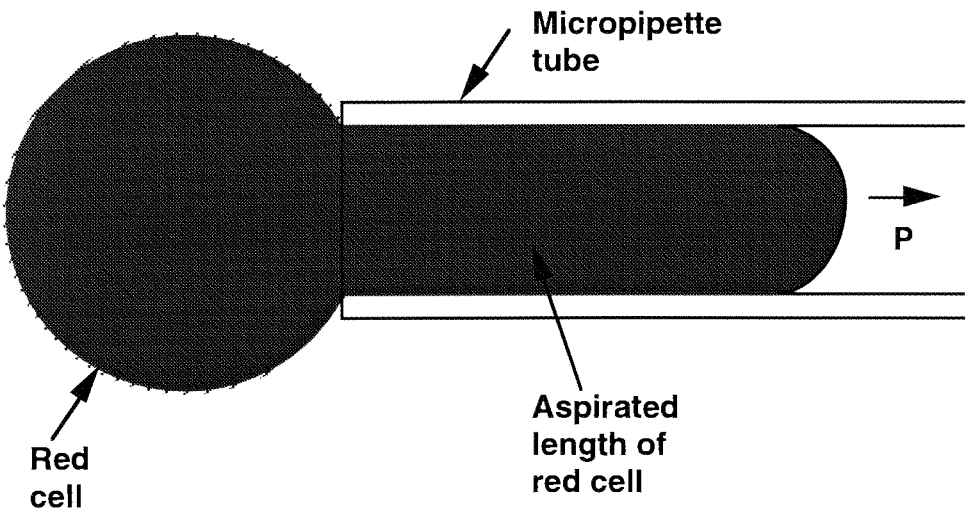

Fig. 1.5 A schematic diagram showing the aspiration of a red cell into a micropipette through the application of a suction pressure P. The micropipettes typically have a diameter of 1/2 to 1 μm.

It has been argued that spectrin filaments behave like entropic springs (Elgsaeter *et al.*, 1986), by which we mean random coils which become more ordered when stretched and regain their

disorder when relaxed. The energy used to deform an entropic spring by stretching is stored as an unfavorable decrease in its configuration entropy. It is easy to show that the elastic moduli of a cross-linked network of ideal polymer chains are proportional to $\rho k_B T$, where ρ is the density of cross-links, k_B is the Boltzmann constant and T is the temperature. Assuming that, on the average, the red cell cytoskeleton is a hexagonal network of spectrin chains, there are approximately 32,000 sixfold junction complexes in an average membrane area of 135 μm^2. The compression modulus, K_A, thus calculated is of the order $\approx 10^{-2}$ dyn/cm (see also Evans, 1979), which is much smaller than that of a liquid and in the range measured experimentally.

1.4 Lateral motion of integral membrane proteins

Integral proteins, such as band 3, are proteins that cross the lipid bilayer. Approximately 40% of the band 3 molecules are bound to the spectrin network, and these molecules show no rotational diffusion (rotating about an axis perpendicular to the plane of the bilayer; Nigg and Cherry, 1980) or lateral diffusion (moving laterally within the membrane). The remaining 60% of the band 3 molecules are not attached to the network and are free to diffuse through the membrane. The rate of diffusion of membrane components is relevant to the transport of membrane-bound enzymes (a number of which are proteins) to various parts of the membrane serving as catalysts to processes essential to the survival of the cell.

Over the past decade, there has been increased research on the subject of lateral motion of membrane proteins (Sheetz *et al.*, 1980; Jacobson *et al.*, 1982; Jacobson *et al.*, 1987, Edidin *at al.*, 1991; Saxton, 1994). The focus has been on what the measured diffusion rates of the proteins within the membrane might imply about the membrane structure and dynamics and also on the development of techniques for lateral mobility measurement.

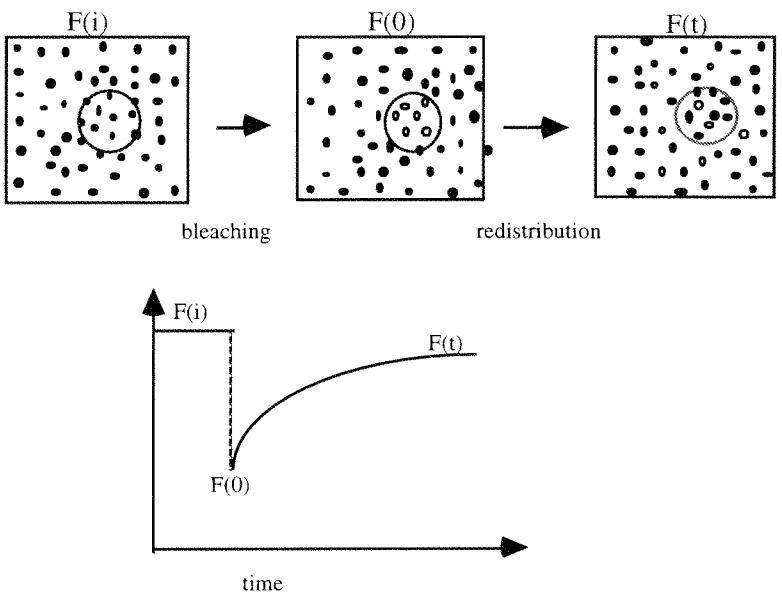

Fig. 1.6 Schematic diagram describing the principle of a typical FRAP experiment. The initial fluorescence intensity F(i) arising from fluorophores within a small area of the membrane surface is measured. The next step involves an irreversible photobleaching of a fraction of the fluorophores (withing dotted circle) by an intensified laser beam. This is followed by monitoring the postbleach fluoroscence intensity as a function of time, F(t).

The main technique that has been used to extract the diffusion rates of proteins is fluorescence recovery after photobleaching or

FRAP (Sheetz *et al.*, 1980). Basically, a laser beam is used to bleach a spot (diameter $\approx 1\ \mu m$) in a uniformly labelled membrane. The increasing flourescence from that spot is monitored as a function of time after bleaching, and the rate of recovery is a direct measure of the lateral diffusion of the flourescent species from the surrrounding medium into the previously bleached spot. The FRAP technique is illustrated in Fig. 1.6. FRAP measurements show that proteins typically diffuse approximately 50 times slower in normal mouse erythrocytes than in spherocytic erythrocytes, which are deficient in the membrane skeleton matrix (Sheetz, 1983). There is also evidence from FRAP measurements that proteins diffuse much more quickly in a pure lipid bilayer than in a membrane with an associated skeleton network (Poo and Cone, 1974).

Recently, restricted motion of proteins has been observed via single particle tracking (SPT) experiments (Gross and Webb, 1986; Kusumi *et al.*, 1993, Sako and Kusumi, 1994) which may involve diffusion of proteins or directed motion with optical tweezers. In the optical tweezer experiments, a membrane protein with a gold particle attached is moved across the plasma membrane in a straight line by optical tweezers (Edidin *et al.*, 1991; Sako and Kusumi, 1995). The optically guided protein is observed to escape from its optical trap at some point in its directed motion. The optical tweezer experiments show that proteins tend to be corraled in specific regions of the membrane. These corrals are presumed to arise from the steric interactions between the guided proteins and the membrane cytoskeleton. Restricted motion of membrane proteins

plays an important role in the life span of a cell. In some cases, the membrane localizes enzymes in regions where soluble substrates can be highly concentrated and subsequently absorbed. An example of this occurs in the intestinal microvillar membrane, which contains numerous enzymes serving to digest starch and proteins.

SPT experiments also allow characteristic length scales of protein motion to be extracted. The tagged protein, at some point of its dragged motion, encounters a barrier (interaction with components of the membrane skeleton) which overcomes the optical trapping force and forces the protein out of the trap. A characteristic length scale, the barrier-free path (BFP), can be obtained from the path length distribution of an optically guided protein motion. For example, Edidin *et al.* (1991) find that the BFPs of two different proteins in the plasma membrane of murine HEPA-OVA cells (hepatoma cells from the lining of the liver of mice, not erythrocytes) are in the micron range. On the other hand, BFPs of tagged transferrin receptors in rat kidney fibroblastic cells are hundreds of nanometers in length (Sako and Kusumi, 1995).

Quantitative analysis of the data taken from FRAP and SPT experiments has proven to be a non-trivial task. This is due to the viscous and hydrodynamic effects which are not easily incorporated into the analysis. Theoretically speaking, BFPs are much easier to analyze than diffusion constants, being less affected by many dynamical attributes of the cytoskeleton. To this end, many

theoretical models have examined the general properties of particle diffusion through barriers, rather than specific cell/protein systems (Saxton, 1982, 1994a,b; Pink, 1985).

1.5 Overview of thesis

This research is focused on the use of computer simulations to examine the geometry and elasticity of the human erythrocyte. The investigation is based on large-scale simulations, involving systems of up to 6500 particles, and took up to 2 years of CPU (central processing unit) time to complete. The simulations were carried out on a combination of 80MHz, 132MHz and 200MHz MIPS processors incorporated into Silicon Graphics machines.

In Chapter 2, the model that is used to represent the erythrocyte membrane cytoskeleton as a network of connected polymer chains is described in detail. The numerical algorithm used to obtain the equilibrated (zero-stress) model network in the stress ensemble is also described.

Chapter 3 uses the cytoskeleton model developed in Chapter 2 to determine the response of the model network to extensional and compressional stresses applied both isotropically and anisotropically. Simple mean field (MF) models of Hooke's-law springs are presented to interpret the simulation results for the membrane cytoskeleton's elastic properties under both small and large deformations. Through

this comparison with the MF models, an effective spring constant of the chains in the model cytoskeleton network is extracted. The effects of a precompression in the rest-state of the cytoskeleton on the geometrical and elastic properties are also investigated.

In Chapter 4, the simulation that is used to probe the barrier-free paths of proteins guided through the membrane skeleton is described. This chapter looks into the constraining effects of the cytoskeleton and also the method of extracting some geometrical parameters of the model network, such as the effective diameter of the network elements attached to the bilayer. A simple scattering theory is proposed to interpret the data obtained in these directed-protein-motion simulations.

There is still debate as to how the cytoskeleton network attaches itself to the lipid bilayer. The dependence of the cytoskeleton's geometry and elasticity on the nature of its attachment to the bilayer is explored by simulation in Chapter 5. The simulations contrast the use of the sixfold junctions as attachment sites to that of the chain midpoints.

A summary of the thesis research is given in Chapter 6 and then followed by three appendices that outline the simple models that are used to fit the simulation results.

Chapter 2
THE CYTOSKELETON MODEL

2.1 Introduction

For the past few decades, numerous experiments and (more recently) computer simulations have been carried out to study the mechanical and in-plane diffusion properties of the red cell plasma membrane. Experimental techniques such as micropipette aspiration (Waugh and Evans, 1979; Discher *et al.*, 1994) and flicker microscopy (Strey *et. al.*, 1995) have been used to measure the shear modulus of the erythrocyte cytoskeleton and the bending modulus of lipid bilayers and plasma membranes. Other viscoelastic properties of the plasma membrane have been explored using the FRAP and SPT techniques described in Chapter 1. Studies of in-plane motion of labelled proteins and lipids also have yielded information on the steric interaction between the cytoskeleton and in-plane membrane components (Kusumi *et al.*, 1993; Sheetz *et al.*, 1980). While the experimental results cannot be interpreted unambiguously with a microscopic model of the cytoskeleton, nevertheless they provide stringent tests for the components of such models.

In this chapter, we present a computational model of the erythrocyte cytoskeleton attached to the bilayer. This reference model will be used to investigate the geometry and elasticity of the cytoskeleton, as well as the in-plane protein-diffusion properties of

the plasma membrane. Geometrical properties of the cytoskeleton that can be obtained from the model include the transverse thickness, the equilibrium separation of the junction complexes and the magnitude of the steric interaction between different spectrin elements. The latter property affects the motion of large proteins in the bilayer and will be described in Chapter 3. The model predicts elastic properties including the shear modulus as well as the area and volumetric compression moduli. The model also is used to probe the effect of externally applied stresses on the elastic moduli (as will be discussed in detail in Chapter 5). In addition, the reference model described in this chapter can be modified to examine the dependence of the cytoskeleton elasticity and geometry on the attachment points of the membrane skeleton to the bilayer.

The model cytoskeleton in this thesis is viewed on the scale of ten nanometers, but is computationally restricted to investigate systems on length scales of half a micron at the most. Although this is not sufficiently large to allow direct comparison with some of the experimental data, such as micropipette aspiration (Discher *et al.*, 1994) or flicker eigenmode decomposition (Strey *et al.*, 1995), the microscopic model can be used as a basis to develop effective two-dimensional models applicable on length scales of 0.1 to 10 μm. In an effective model of the cytoskeleton, a spectrin tetramer is viewed as a single component, such as a harmonic spring, rather than as an object with many subcomponents, such as a polymer chain. While an effective network may not possess all of the characteristics of a microscopic computational model, it does allow one to investigate

systems on larger length scales and to compare the microscopic model with the known properties of two-dimensional networks. For example, the elastic properties of triangular networks confined to a plane have been determined as a function of stress (Boal, Seifert and Shillcock, 1993), while the elastic and geometrical properties of two-dimensional triangulated networks fluctuating in three dimensions have been computed at zero stress (Le Doussal & Radzihovsky, 1992; Gompper and Kroll, 1991).

The chapter is organised as follows. In Sec. 2.2, we describe the microscopic model of the cytoskeleton/bilayer system as a triangulated network of polymer chains and the Monte Carlo technique used to generate a set of configurations that properly samples the fixed-stress ensemble. Next, the behaviour of the geometrical properties of the model cytoskeleton is studied in Sec. 2.3. This is then followed by Sec. 2.4, in which physical values are assigned to the model parameters such as the number of segments on each chain and also the polymer potential parameters. A summary of Chapter 2 is found in Sec. 2.5.

2.2 The reference model

The computational reference model that we use in probing the structural characteristics of the erythrocyte cytoskeleton under stress is similar to one that has been used to predict cytoskeleton properties at zero stress (Boal, 1994). The two main components of

the plasma membrane that make up our computational reference model are the bilayer and the attached network of spectrin tetramers.

In our computational model, the bilayer is flat and lies in the computational xy plane. The rationale for the flatness assumption is as follows. In the treatment of the elasticity of bilayers, it was conjectured by Canham (Canham, 1970) and others, that the statistical behavior of a fluid membrane, freely fluctuating in a solvent, can be studied within a continuum model based on the following Hamiltonian:

$$H_{el} = \int dA \, [(\kappa_b/2)(C_1+C_2-C_0)^2 + \kappa_G C_1 C_2], \qquad (2.1)$$

where C_1 and C_2 are the principal curvatures at a given point in the membrane surface and C_0 is the spontaneous curvature. In the continuum model, C_0, κ_b (the bending rigidity) and κ_G (the Gaussian bending coefficient) are intrinsic characteristics of the membrane arising from its chemical composition. The ground state of the continuum model, for fixed values of C_0, κ_b and κ_G, is found by varying C_1 and C_2 across the membrane surface to minimize H_{el}.

Experimental evidence shows that the bending modulus κ_b of a pure (DMPC) phospholipid bilayer is of the order of 10-25 $k_B T$ (Evans and Rawicz, 1990). The persistence length ξ of a membrane governed by Eq. 2.1 has been estimated by de Gennes & Taupin (1982), to be

approximately

$$\xi \approx a_o \exp(2\pi\kappa_b / k_B T) \qquad (2.2)$$

where a_o is a molecular lengthscale ($\sim$ 1 nm). For $\kappa_b \sim 10\ k_B T$, this yields an astronomically large value of 10^{15} km for ξ. This value for ξ may seem unphysically large; but it does tell us that the persistence lengths of bilayers are not small and that the bilayer does resist (if not strongly) bending in the transverse direction. Based on this observation, it is not inappropriate to make our computational bilayer flat on the simulation length scale of approximately one micron.

With respect to the RBC membrane cytoskeleton, studies (see Steck, 1989) have shown (*in situ*) that the cytoskeleton has a high degree of extensibility. The span of the spectrin tetramers on the intact RBC membrane is $\sim$ 76 nm, which is approximately 37% of the contour length of the 200 nm tetramer, a ratio of 1:2.6 (see also Liu *et al.*, 1987). On the other hand, photographs (taken via transmission electron microscopy) of the RBC cytoskeleton (Heuser, 1983), have also shown that spectrin tetramers are highly convoluted filaments connecting short, linear actin filaments. Recall (from Chapter 1) that isolated spectrin behaves much like a highly flexible filament; besides being able to be collapsed into a compact form, it can also be drawn linear. As pointed out by Stokke *et al.*, (1986a,b), this behavior of the spectrin filament is similar to what is expected from

a polymer chain in a solvent, in which the elasticity of the chain is governed by the entropy of the chain configurations.

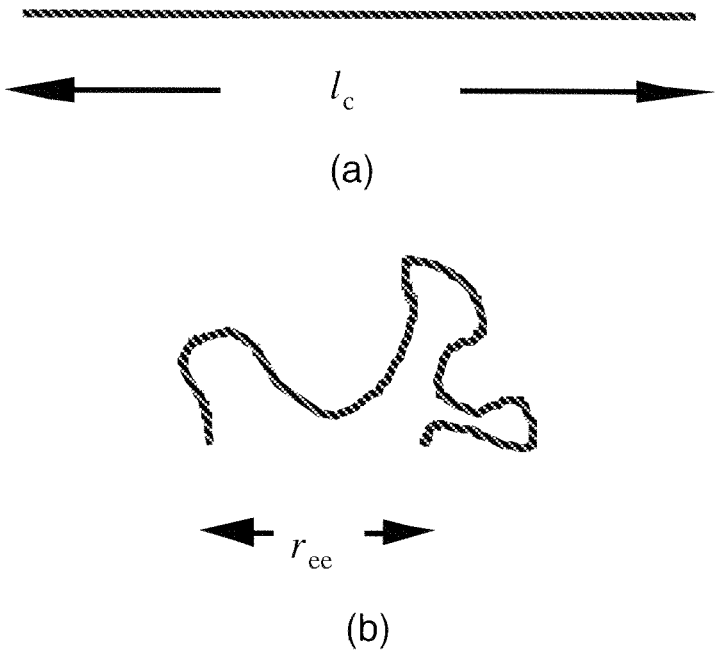

Fig. 2.1 Diagram shows two different configurational states of a polymer chain. (a) Chain fully extended and its end-to-end distance l_c is defined as the contour length. (b) Chain in its natural relaxed state; its mean end-to-end distance $<r_{ee}>$ is much smaller than its contour length l_c.

From the behavior of random walks (for a review, see Doi and Edwards, 1986), entropic considerations result in the average end-to-end distance $<r_{ee}>$ of a polymer chain being shorter than its contour length l_c. This is seen as follows. Consider an ideal chain (no self-avoidance) with n_{seg} segments each of length a: $<r_{ee}/a>$ grows like $n_{seg}{}^{1/2}$, while l_c/a is equal to $n_{seg}{}^{1}$. Thus, $<r_{ee}>/l_c$ scales like

$n_{seg}^{-1/2}$, showing that $<r_{ee}>$ is shorter than l_c. Thus, the polymer chain, in its natural resting state, is convoluted (see Fig. 2.1)

Stretching a freely-jointed chain from its equilibrium configuration decreases its entropy and hence increases its free energy. This means that, if we were to constrain a polymer chain by having its ends fixed at specified points, the chain will be acted on by a tensile force (in the direction of the line joining its ends) which is proportional to the end-to-end distance of the chain. The effective spring constant of an ideal chain (n_{seg} segments) at modest deformations is given by $k_{sp} = dk_BT/r_{ee}^2$, where k_B is Boltzmann's constant, T is the temperature, r_{ee} is the average end-end distance of the chain and d is the embedding dimension. We refer to the polymer chain, therefore, as an entropic spring. (For a more detailed development of this, please see Appendix A).

The shear modulus of the RBC cytoskeleton network has been observed experimentally to be approximately $\beta\mu<A_v> \approx 7\text{-}11$, where β is the inverse temperature $(k_BT)^{-1}$ and A_v is the mean area per junction vertex if the cytoskeleton network is taken to be a uniform triangular network ($A_v \approx 5x10^3$ nm^2). If one were to treat the spectrin tetramers as ideal polymer chains with an effective spring constant $k_{sp} = 3k_BT/<r_{ee}^2>$ (see above) and $<r_{ee}^2> = a^2n_{seg}$, then a network of such chains has $\beta\mu<A_v> \approx 1.1$ (see Appendix B for review of the calculation). Of course, a network of truly ideal chains collapses (Kantor, Kardar and Nelson, 1986), and self-avoidance of the chains must be included to describe physical systems. However,

the above order-of-magnitude description of the erythrocyte cytoskeleton elasticity shows that the use of polymer chains with excluded volume effects would be a reasonable model for the actual RBC cytoskeleton.

In our reference model, then, each spectrin tetramer is modeled by a single polymer chain with n_{seg} segments, and the ends of the chains are linked together at sixfold-coordinated junction complexes. The vertices defined by the segment endpoints can be either 2-fold coordinated (along the chain) or 6-fold coordinated (at the junction complexes). To mimic the way the cytoskeleton appears to be attached to the bilayer of the red blood cell, the midpoint of each chain is constrained to move exclusively in the computational xy plane representing the bilayer. All other chain elements are restricted to move in the positive z direction (that represents the cytoplasmic side of the bilayer) through elastic collisions with the bilayer. Since the way the cytoskeleton actually attaches itself to the bilayer is not known unambiguously, two alternate attachment models are described in Chapter 5: (1) attachment of the cytoskeleton to the bilayer at the junction complexes and (2) attachment at both the midpoints of the chains and the junction complexes. The reference model as described in this chapter (and also in Chapters 3 and 4) has the attachment point only at the midpoints of the chains.

In a previous study of the elastic properties of the erythrocyte cytoskeleton (Boal, 1994), the chains were modeled by bead-and-

tether potentials, which is efficient for Monte Carlo (MC hereafter) type simulations. But, we would like eventually to extend our study to dynamical phenomena such as diffusion. To incorporate explicit time evolution of the system, the simulations in this thesis are based on molecular dynamics (MD hereafter) techniques, which require a smoother interparticle potential than the step-functions used in the bead-and-tether models. We use a potential developed by Bishop, Kalos and Frisch (BKF hereafter; Bishop, Kalos and Frisch, 1979) and well documented in other recent simulation work on polymers (Grest and Kramer, 1986). In the BKF potential, any two vertices are subject to a short-range repulsive potential,

$$\begin{aligned} V_{\text{rep}}(r) &= 4\varepsilon\{(\sigma/r)^{12} - (\sigma/r)^{6} + 1/4\} \qquad 0 < r < 2^{1/6}\sigma \\ &= 0 \qquad\qquad\qquad\qquad\qquad\qquad\qquad\qquad r > 2^{1/6}\sigma \end{aligned} \tag{2.3}$$

where ε and σ are the fundamental energy and length scales of the simulation and r is the inter-vertex distance. In general, modelling the complete bond potential of a polymer chain involves a length and energy scale as determined by Eqs. (2.3) and (2.4). Each individual spectrin chain (in our reference model) is being modelled as a freely-jointed chain, whose segment lengths are determined from the known geometry of the RBC cytoskeleton. Thus, no direct mapping of the simulation potential parameter ε onto experiment is necessary. To facilitate the implementation of the simulation, the energy scale ε is then set equal to $k_{\text{B}}T$ and the force is measured in units of ε/σ.

Each vertex along the chain is connected either to two (along the chain) or six (at the junction points) nearest-neighbour vertices through the potential

$$V_{att}(r) = -0.5\Gamma R_c^2 \ln[1-(r/R_c)^2] \qquad (2.4)$$

where Γ and R_c are parameters. Choosing the parameter set $R_c/\sigma =$ 1.5 and $\Gamma\sigma^2/\varepsilon =$ 30 (Grest and Kramer, 1986), the combined potential Eq. (2.3) and (2.4) has a minimum at $r/\sigma =$ 0.97. A leapfrog algorithm (Allen & Tildesley, 1981) is used to integrate the equations of motion with time step $\Delta t = 0.005(m\sigma^2/\varepsilon)^{1/2}$, where m is the vertex mass. Fixing values for σ and the temperature allows the presentation of simulation results in physical units. The investigation of time-dependent phenomena, such as diffusion, would necessitate the incorporation of viscous (hydrodynamic) effects to determine the parameters such as m, which is beyond the scope of this thesis.

In the simulations, 16 (4 rows of 4 vertices each) junction vertices are used; and n_{seg}, the number of segments along a given chain, is varied over the range from 10 to 26. The simulation to determine the geometrical and elastic properties of the model network is carried out at constant temperature and pressure via a combined MC and MD algorithm with periodic boundary conditions (PBC hereafter) in both x and y directions. The MD algorithm is used to speed up the relaxation of the network, as it allows the system to probe configuration space more efficiently. The lengths L_X and L_Y of

the periodic rectangular boundaries are allowed to fluctuate independently following a MC algorithm developed by Wood (Wood, 1968). A set of configurations with varying L_x and L_y selected with the appropriate Boltzmann weights are generated for each pressure and chain segmentation of interest. Testing of the accuracy of the simulation program described above is done through comparison of selected simulation results with that obtained using a independently written simulation code (private communications with Boal, 1993).

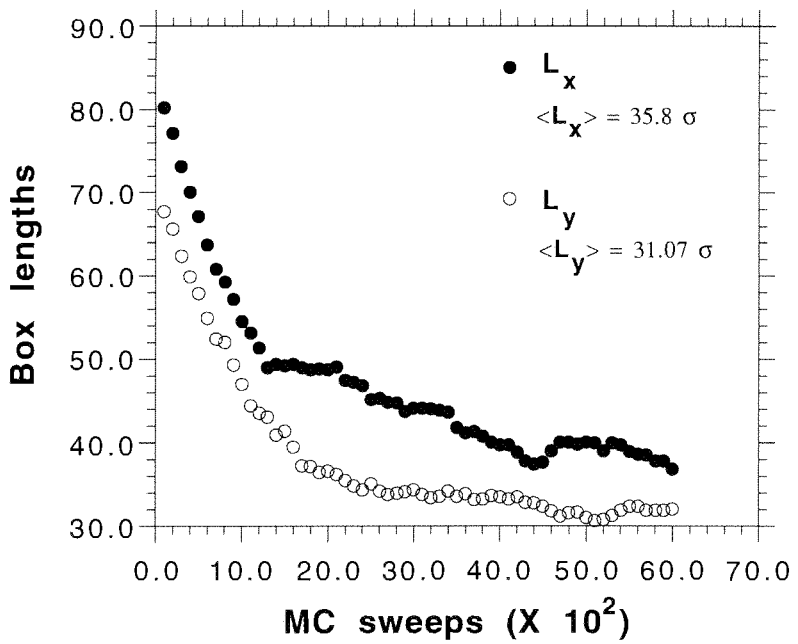

Fig. 2.2 Plot showing the relaxation of the simulation box lengths L_x and L_y as a function of the number of MC sweeps. Here, the plot is for n_{seg} = 20.

For the purpose of analysing ensemble averages of observables, between 300 to 600 configurations are stored for each parameter set, with each configuration separated by $\tau = 2.5 \times 10^4$ MC sweeps to reduce the correlation between successive configurations. The choice for τ above is based on the following observation. The longest relaxation (Rouse model) time of an ideal polymer chain in a solvent grows like n_{seg}^2 (De Gennes, 1979) MC steps, so the relaxation time for our polymer network is expected to be large. Though systematic relaxation studies were not done, we observed that, for example (see Fig. 2.2), it takes approximately 5×10^3 MC sweeps (coupled with 5000 interleaved MD steps, with 1 MD step per MC step) for the network ($n_{seg} = 20$) to relax from a cold start (perfect hexagonal network) to its equilibrium state.

The primary assumptions that go into setting up the microscopic reference model of the RBC membrane cytoskeleton are: (1) the natural resting state of the cytoskeleton network is its zero stress equilibrium state, $P = 0$. (2) The ratio of the contour area to the resting state area is equal to seven (Steck, 1989). Here, in the reference model, the contour area is obtained by having the network lie flat in the computational xy plane, with all the links in the chains straightened out and the length of each segment equal to its zero temperature value of 0.97σ. Hence, the contour area per junction complex A_c is given by

$$A_c = (3^{1/2}/2)(0.97 n_{seg}\sigma)^2. \qquad (2.5)$$

A snapshot of an equilibrated network (with $n_{seg} = 20$) of the reference model at zero stress is shown in Fig. 2.3, which shows a face-view of the network, looking down the positive z-axis towards the computational xy plane representing the bilayer. Note that the chains are highly convoluted as one might expect from a network of polymer chains. The out-of-plane thickness is a couple of segment lengths.

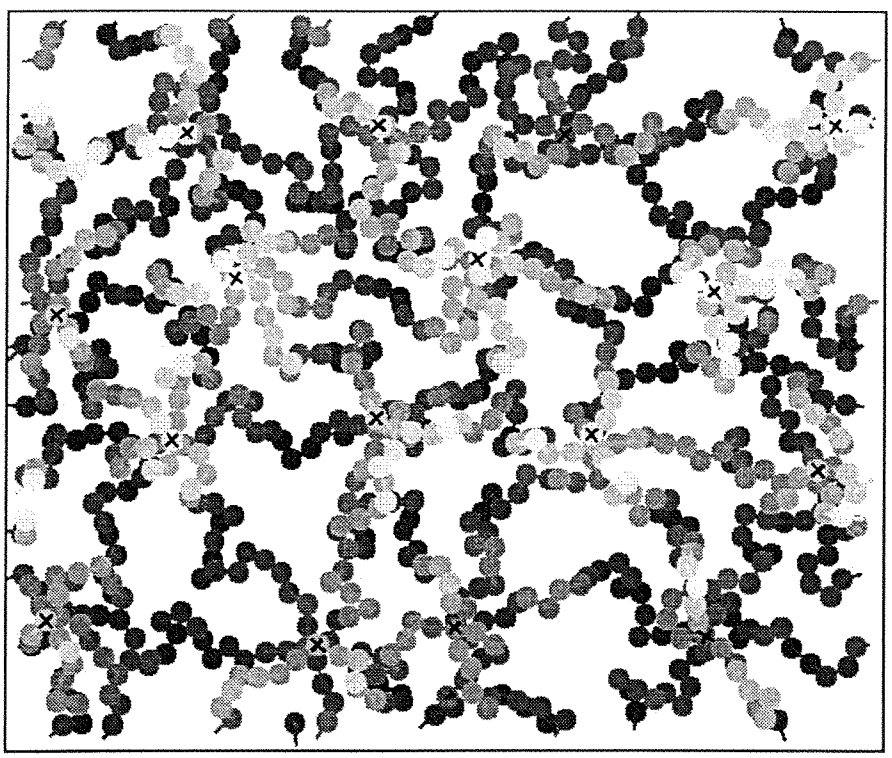

Fig. 2.3 (a) Diagram showing (+z axis view) an equilibrated configuration of the reference model network of the RBC cytoskskeleton. The chains with the darker shade lie further back into the background. Here $n_{seg} = 20$. The crosses represent the locations of the sixfold junctions.

2.3 Network geometry

In order to determine the value of n_{seg} which would allow us to model the geometrical and elastic properties of the RBC cytoskeleton, we would need to know how the mean area of the network scales with n_{seg}. As discussed previously in Sec. 2.2, the end-to-end distance of an ideal chain is smaller than its contour length l_c. The same general type of behaviour is also expected for a network of polymer chains (the reference model) described in Sec. 2.2. From the simulations, we find the equilibrium network area per junction $<A_j>$ as a function of the n_{seg} to be given by (see Fig. 2.4),

$$<A_j/\sigma^2> = 2.0 n_{seg}^{1.2}, \qquad (2.6)$$

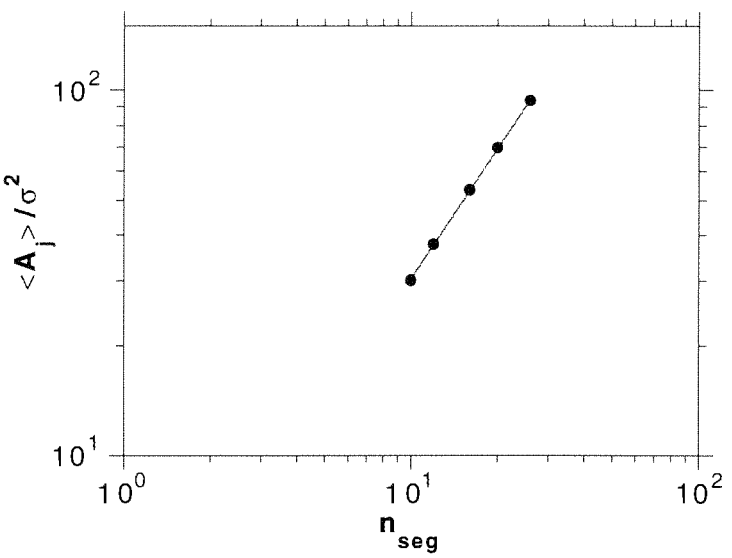

Fig. 2.4 Behavior of the mean network area per junction complex $<A_j>$ as a function of the number of segments n_{seg} in each chain. The solid line through the data points is the equation $2.0 n_{seg}^{1.2}$.

which shows that the mean area per junction complex of the network does indeed increase with n_{seg}. Even though the network area increases with n_{seg}, the network area shrinks relative to its contour area. This can be seen as follows. The contour length of an ideal chain is approximately $n_{seg}\sigma$, so that the contour area per junction complex A_c is $(3^{1/2}/2)(n_{seg}\sigma)^2$ (see Eq. (2.5)). The end-to-end distance $<r_{ee}>$ of an ideal chain is approximately equal to $n_{seg}^{1/2}\sigma$ and, hence, the equilibrium area per junction complex A_j^{ideal} scales like n_{seg}^{1}. The ratio A_j^{ideal}/A_c then scales as n_{seg}^{-1}, which clearly shows that the area of a network of ideal chains does shrink relative to its contour area as n_{seg} grows.

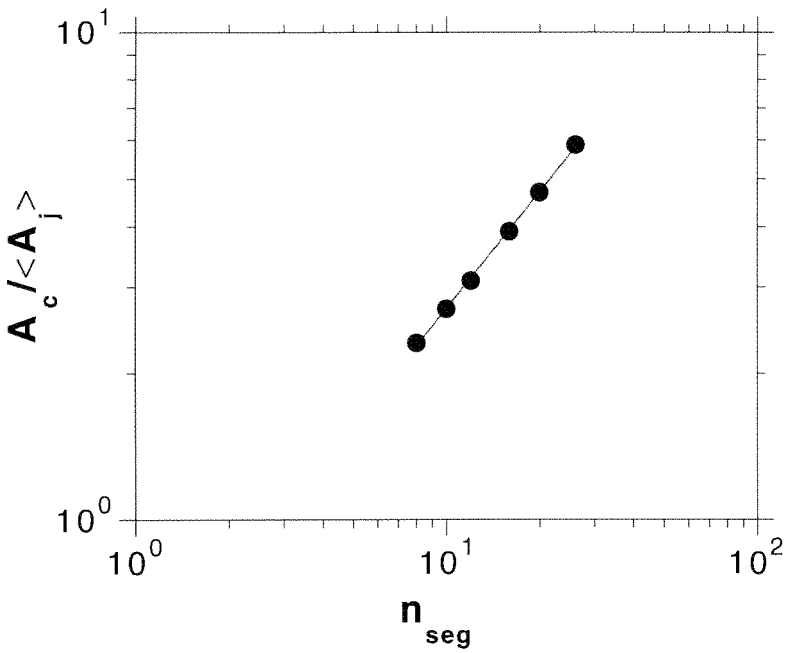

Fig. 2.5 The contour area per junction A_c is compared with the mean area per junction vertex $<A_j>$. The solid line through the data points is the equation $A_c/<A_j> = 0.4n_{seg}^{0.8}$.

Now, consider the case with self-avoidance of the chains included. In this case, the end-to-end distance $<r_{ee}>$ of an isolated chain scales approximately as $n_{seg}^{0.6}$ (see de Gennes, 1979) so that the equilibrium network area $<A_j>$ should scale like $n_{seg}^{1.2}$ (which agrees well with the simulation result in Eq. (2.6)). The ratio $<A_j>/A_c$ scales like $n_{seg}^{-0.8}$, showing again that $<A_j>$ decreases relative to A_c as n_{seg} increases, much like the former case of the ideal polymer chain network. Fig. 2.5 shows the ratio of $A_c/<A_j>$ for the reference model network as a function of n_{seg} at zero pressure. We find that $A_c/<A_j>$ can be fitted by $0.4n_{seg}^{0.8}$ (solid line in figure).

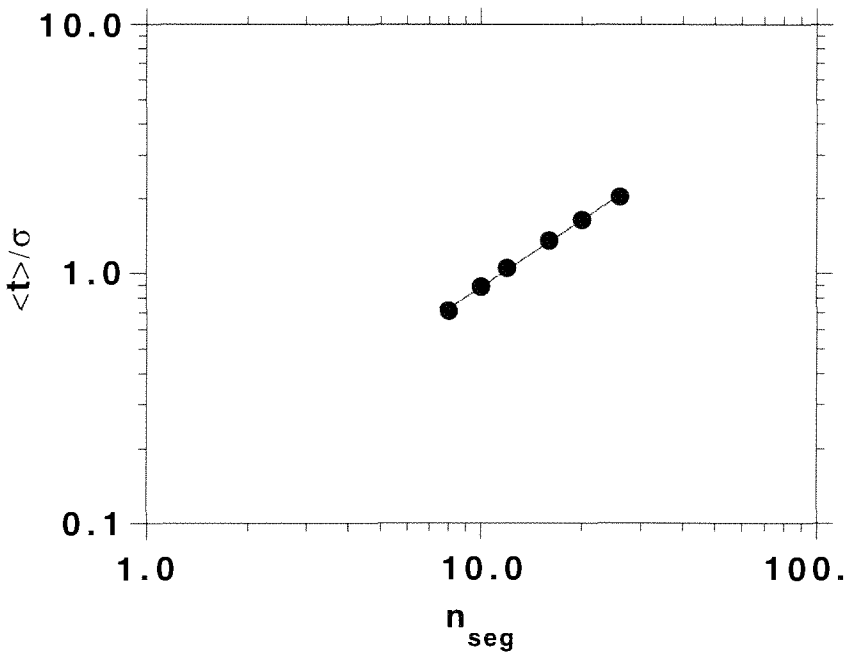

Fig. 2.6 The mean height $<t>$ of the network as a function of the number of segments n_{seg} along the chain. The straight line shows the fit $<t>/\sigma = 0.11n_{seg}^{0.9}$.

Since the mean in-plane area per junction vertex $<A_j>$ of the network is significantly less than its contour area per junction vertex A_c, it is no surprise that the network has, on the average, a finite displacement from the computational xy plane. The average displacement $<t>$ of the network from the xy plane (bilayer) may be estimated as follows. For a single network configuration, the displacement t is defined as the average displacement in the $+z$ direction of all the vertices in the network, including the ones that are tacked to the xy plane. Note that, hereafter, the thickness of the network is defined as $2<t>$. The ensemble average $<t>$ is found to scale with n_{seg} as (see Fig. 2.5),

$$<t>/\sigma = 0.11 n_{seg}^{0.9}. \qquad (2.7)$$

It should be noted that the scaling behavior of both $<A_j>$ and $<t>$ as a function of n_{seg} is similar to what was observed in a previous study of the network using square-well potentials (Boal, 1994).

As mentioned in Sec. 2.2, one of the requirements used to set the parameter of the reference model is that the ratio $A_c/<A_j>$ should be equal to seven. This allows us to fix n_{seg} at 32 (see Fig. 2.5). The physical value of σ, on the other hand, is fixed by the contour length of the spectrin tetramers, taken to be approximately equal to 200 nm (see Steck, 1989). The contour length, together with $n_{seg} = 32$, gives $\sigma = 6.4$ nm. Using the values of n_{seg} and σ obtained above, we find that the mean displacement of the erythrocyte

cytoskeleton from the bilayer is predicted to be approximately 16 nm (see Eq. 2.5). With the bead-and-tether model (Boal, 1994), $\langle t \rangle \approx$ 15 nm. Thus far, the mean displacement of the RBC cytoskeleton has not been measured.

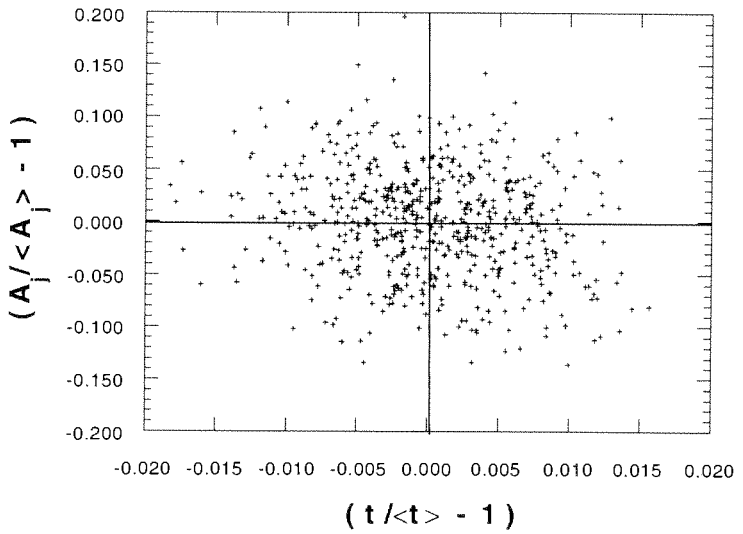

Fig. 2.7 Scatter plot of the area per junction vertex A_j and displacement t for $n_{seg} = 20$ for 600 configurations. Each point represents a pair of values $(A_j/\langle A_j \rangle)-1$ and $(t/\langle t \rangle)-1$. Note that the dispersion of the network area A_j and displacment t is less 15%.

We also find that the fluctuations of A_j and t around their mean values are not large. In Fig. 2.7, we show a scatter plot of the values of A_j and t for the particular choice, $n_{seg} = 20$. What is shown are the values of $(A_j/\langle A_j \rangle)-1$ and $(t/\langle t \rangle)-1$ for each configuration used in calculating the ensemble average. As expected, the data points cluster near the origin, and few configurations fluctuate more than 15% away from the mean. Fig. 2.7 shows that there is no

observable correlation between A_j and t. This tells us that, in our simulations, the reference model does not maintain an approximately constant volume per junction vertex; i.e, when the area of the network is larger than average, the displacement t of the network does not necessarily compensate by becoming smaller than average. This is in contrast to the bead-and-tether network (Boal, 1994), where there is a reasonably strong correlation between A_j and t, thus providing relations between several of the network elastic constants (this point will be explored further in Sec. 2.4).

2.4 Network elasticity

The elastic moduli K_A (area compression modulus), μ (shear modulus), K_V (volume compression modulus) and $Y_\perp$ (Young's modulus for network thickness) can be obtained from fluctuations in the PBC box size and network thickness (for a review of the definitions of the elastic moduli and the method of extraction from the simulation, see Appendix D). Because the moduli are determined from fluctuations, there is a greater uncertainty in their values than there is for $<A_j>$ or $<t>$. The errors in the moduli quoted below are approximately 20%.

The elastic moduli plotted in Figs. 2.8, 2.9, 2.10 and 2.11 are rendered unitless by multiplying each of those quantities by the appropriate powers of σ and by the inverse temperature β. Fits to the data which go into Figs. 2.8 and 2.9 show that the in-plane

moduli are described approximately as,

$$\beta K_A \sigma^2 = 192\, n_{seg}^{-2.0} \tag{2.8}$$

$$\beta \mu \sigma^2 = 81\, n_{seg}^{-2.0}. \tag{2.9}$$

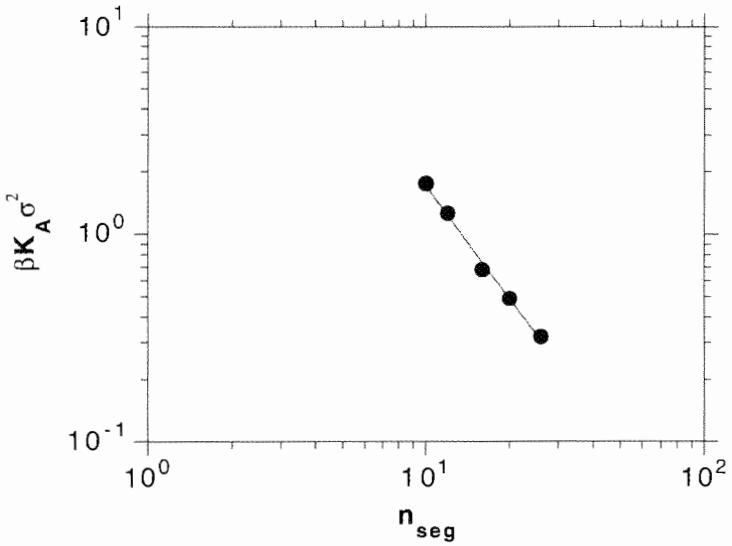

Fig. 2.8 In-plane area compression modulus K_A measured for the reference model as a function of n_{seg}. Data are obtained for a system of 16 sixfold junction vertices. The straight line is the fit $\beta K_A \sigma^2 = 192 n_{seg}^{-2.0}$.

This gives a ratio of the in-plane compression modulus to the shear modulus of 2.4. It is known (Boal, Seifert and Shillcock, 1993) that for two-dimensional networks of Hooke's law springs, the ratio K_A/μ, at zero pressure, is exactly equal to 2. Recent work carried out on a similar type of network (Hansen, Skalak, Chien and Hoger, 1996), which included defects in the network's connectivity, also found $K_A/\mu \approx 2$, indicating that inclusion of randomness in

connectivity may not necessarily affect some of the characteristics of the network.

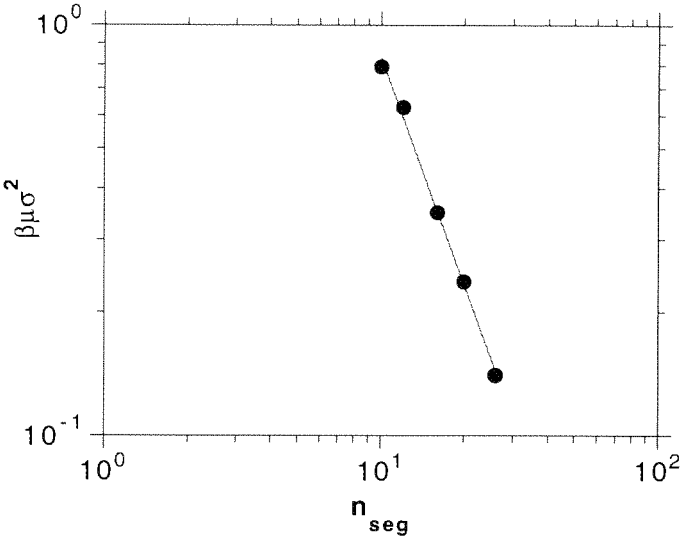

Fig. 2.9 In-plane area shear modulus μ measured for the reference model as a function of n_{seg}. Data are obtained for a system of 16 sixfold junction vertices. The straight line is the fit $\beta\mu\sigma^2 = 81 n_{seg}^{-2.0}$.

A dimensionless quantity that allows comparison of the simulation results with known experimental data and also with networks of ideal chains is $\beta G\langle A_j\rangle$, where G is the appropriate in-plane elastic modulus (namely K_A and μ) and A_j is the network area per junction complex. Table 2A shows the values of $\beta\mu\langle A_j\rangle$ and $\beta K_A\langle A_j\rangle$ for the three different cases: (1) triangulated network of ideal chains (see Appendix B), (2) physical RBC cytoskeleton (Waugh and Evans, 1979) and (3) simulation results of the reference model.

	Triangulated network of ideal chains	RBC cytoskeleton (experiments)	Reference model
$\beta\mu\langle A_j\rangle$	$\approx$ 1	7–11	10
$\beta K_A\langle A_j\rangle$	$\approx$ 2	14–22	24

Table 2A Comparison of simulation results ($n_{seg} = 32$) with an ideal network model and with the micropipette aspiration experiments. Measurement of RBC flicker at long length scales gives a vanishing shear modulus.

From Table 2A above, one can see that the normalised in-plane elastic moduli for a network of ideal chains differ by an order of magnitude from those of a RBC cytoskeleton and also from those of the reference model (evaluated for $n_{seg} = 32$). Furthermore, there is no dependence, in the ideal chain case, of the normalised in-plane elastic moduli on n_{seg} (see Appendix B), while over the range of n_{seg} investigated in the simulation, Eqs. (2.6) and (2.9) predict that

$$\beta\mu\langle A_j\rangle \sim n_{seg}^{-0.8}. \tag{2.10}$$

This apparent difference in the scaling behaviour between ideal networks and the simulation is expected, since the simulation includes steric interaction among the chains and between the chains and the bilayer, which is absent in the ideal chain case. Table 2A shows, however, that the normalised in-plane moduli agree well with the experiments (within the uncertainties of the simulation and experiment).

The other moduli which can be extracted from the simulation are the volume compression modulus, K_V, and transverse Young's modulus, $Y_\perp$, which scale with n_{seg} as (see Appendix D for defintions):

$$\beta K_V \sigma^3 \approx 1583\, n_{seg}^{-2.8} \tag{2.11}$$

$$\beta Y_\perp \sigma^3 \approx 44\, n_{seg}^{-0.6}. \tag{2.12}$$

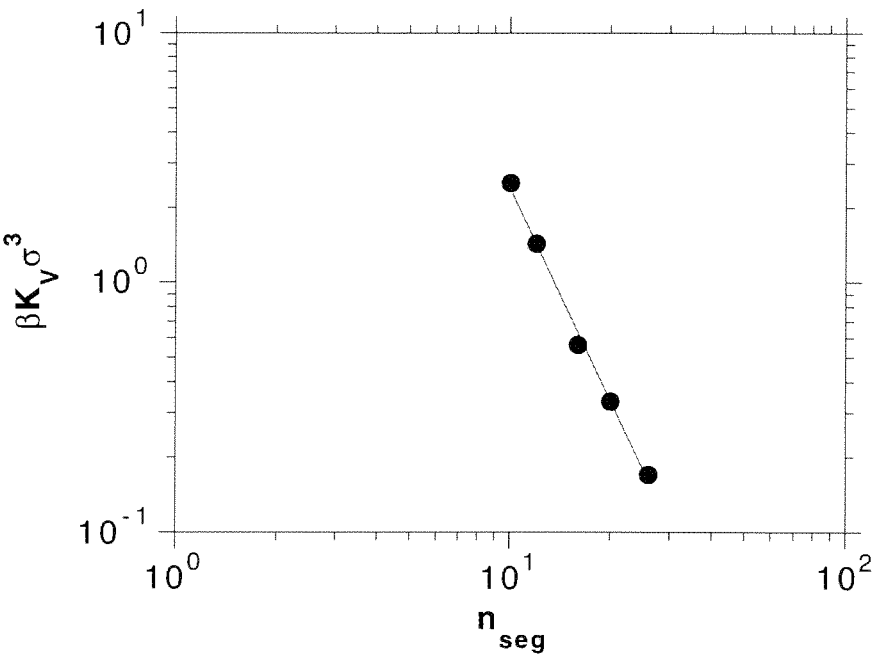

Fig. 2.10 Volume compression modulus K_V obtained in the reference model as a function of n_{seg}. Data are obtained for a system of 16 sixfold junction vertices. The straight line is the fit $\beta K_V \sigma^3 = 1583 n_{seg}^{-2.8}$.

The data for these two moduli are shown in Figs. 2.10 and 2.11, respectively. The uncertainty in the exponents of the elastic moduli in Eqs. (2.8)–(2.9) and (2.11)-(2.12) is about 10%.

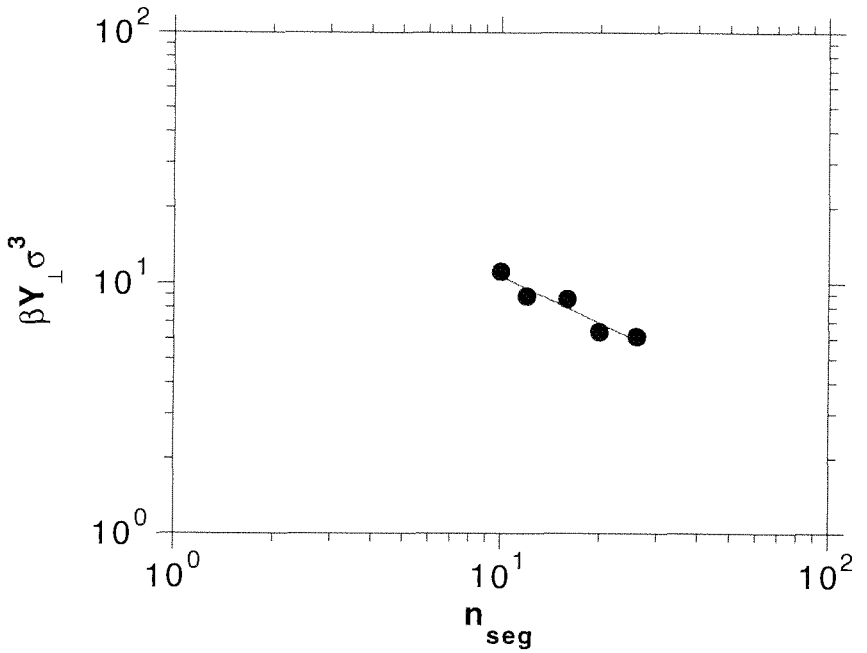

Fig. 2.11 Transverse Young's modulus $Y_\perp$ measured for the reference model as a function of n_{seg}. Data are obtained for a system of 16 sixfold junction vertices. The straight line is the fit $\beta Y_\perp \sigma^3 = 44 n_{seg}^{-0.6}$.

The decrease in the moduli with n_{seg}, as observed in the simulations, is expected. Recalling the analogous case of an ideal chain, we know from statistical considerations that the elastic spring constant is inversely proportional to n_{seg}. That is to say, as n_{seg} increases (with the segment length kept constant), it becomes easier to pull on the chain. Taking this idea a little further, if we have two

polymer chains of different lengths and consisting of different numbers of segments (with identical segment lengths on both chains), the longer chain will be less resistant to tensile stress. This is due to the longer chain being "floppier", i.e., the available configuration space for the longer chain in moving from one state to another is significantly larger than that for the chain with a smaller number of segments. Consider now applying this analogy to a triangulated network consisting of such chains. One would expect that, as n_{seg} increases, the network expands, becomes more open, and thus offers less resistance to stress. Thus, the moduli are expected to decrease with increase in n_{seg}.

In Sec. 2.3, no observable correlation was found between the network area A_j and the thickness t for BKF polymer networks. This is in contrast to the bead-and-tether model (Boal, 1994), where there was a definite correlation between A_j and t, a fact that allowed the connection $Y_\perp \approx K_V$ to be made (see Appendix D). This equality is not observed in Eqs. (2.11) and (2.12), which is consistent with the results extracted from the stress dependence of the moduli (in particular, K_V and $Y_\perp$) presented in Chapter 3.

Using $\sigma = 6.4$ nm and $n_{seg} = 32$, the simulation predicts $K_A = 1.8 \times 10^{-5}$ J/m^2 and $\mu = 7.7 \times 10^{-6}$ J/m^2 at $T = 300$ °K. Experimentally, deformation of an RBC induced by micromechanical manipulation (Waugh and Evans, 1979) gave a measured value of the shear modulus to be approximately 6-9 x 10^{-6} J/m^2. A related experiment (Engelhardt and Sackmann, 1988), using deformations

induced by high frequency electric fields, yields $6\pm1 \times 10^{-6}$ J/m^2. However, recent experiments on RBC flickering (Strey *et al.*, 1995) give a shear modulus approximately equal to 10^{-7} J/m^2. We do not believe that this difference in the value of the shear modulus is an inconsistency, since the various methods of extracting the shear modulus were carried out on different lengthscales. In particular, the lengthscales for measurements in our simulations and the micropipette aspiration experiments are fractions of a micron; while the flicker experiments measure fluctuations in the micron range.

From Eq. (2.11) and Fig. 2.10, the simulation predicts $K_V = 1.4 \times 10^3$ J/m^3 for the human erythrocyte. A measurement of this compression modulus is currently being performed (Evans and Ritchie, private communication). The transverse Young's modulus is predicted to be $Y_\perp = 8.7 \times 10^4$ J/m^3 (see Eq. (2.12) and Fig. 2.11); however, there is currently no available experimental data to compare with. While there may not be complete experimental data available for comparison, the elastic moduli (with exception of the transverse Young's modulus) agree well with the bead-and-tether model (Boal, 1994). We believe that the discrepancy in the Young's modulus is related to the ensemble used in our simulations. The value of $Y_\perp$ obtained though a pure MC algorithm (private communications with Boal, 1997) for an identical model network of the cytoskeleton is found to be not much different from that for K_V. The two ensembles, canonical (pure MC) and microcanonical/canonical (MD/MC) give different distribution of the

values for t, leading to significant differences in the value of $\langle t^2 \rangle - \langle t \rangle^2$, which is crucial to the calculation of $Y_\perp$.

2.5 Summary

In this chapter, we have presented a reference model designed to mimic the geometrical and elastic properties of the red blood cell cytoskeleton. The membrane skeleton is modeled by a hexagonal network of polymer chains with the number of segments n_{seg} on each chain fixed by the known geometry of the cytoskeleton. The network is attached to the computational xy plane (representing the bilayer) at the midpoints of the chains. Other possible attachment points will be discussed later, in Chapter 5. Simulations, utilizing the Monte Carlo algorithm in the stress ensemble, predict that the number of segments required to properly model the geometrical and elastic properties of the RBC cytoskeleton is 32 and that the elementary segment length is ~ 6.4 nm.

Furthermore, the elastic moduli of the network, at zero stress, have been extracted. The area compression modulus K_A is measured to be approximately 1.8 x 10^{-5} J/m^2, while the shear modulus is equal to 7.7 x 10^{-6} J/m^2. The volume compression modulus K_V is predicted to be equal to 0.9 x 10^3 J/m^3 and the transverse Young's modulus is equal to 6.1 x 10^4 J/m^3. The value obtained for the shear modulus is in agreement with one set of experiments carried out on the RBC cytoskeleton. All the moduli extracted from the reference

model, with exception of the transverse Young's modulus, compare well with those obtained with the bead-and-tether model (Boal, 1994).

Thus far, we have established the basic parameters of the reference model that will be used to describe the RBC cytoskeleton. In the following chapters, the reference model will be used to analyze the geometrical and elastic properties of the network under large deformations (isotropic and anisotropic). Comparisons will be made between different models of attachment to the bilayer. The known geometry of the reference model permits it to be used as a computational laboratory for studying a number of aspects of directed protein motion.

Chapter 3
MODEL NETWORK SIMULATIONS AT FINITE DEFORMATIONS

Sec. 3.1 Introduction

As mentioned in Chapter 1, the red cell undergoes a long tortuous journey through numerous tiny capillaries, delivering oxygen and removing carbon dioxide from the cells in the human body. As the red cell passes through a capillary, it is often put under a diverse range of shear stresses. The protein scaffolding (cytoskeleton), which is attached to the cytoplasmic side of the bilayer, bears the full impact of the shear stresses and, thus, helps to prevent the RBC membrane from rupturing.

Numerous experiments (including micropipette aspiration and flicker microscopy) have been used to measure the RBC cytoskeletal network in-plane elastic constants at small (Zilker *et al.*, 1992; Peterson *et al.*, 1992; Strey *et al.*, 1995) and moderate stress (Waugh and Evans, 1979; Hochmuth, 1987; Engelhardt and Sackmann, 1988; Discher *et al.*, 1994). In particular, micropipette aspiration (Discher *et al.*, 1994), coupled with flourescent labelling techniques, have been used to visualise the response of the cytoskeletal network to applied stresses. The experiment, termed flourescence-imaged micropipette aspiration, was used to map the redistribution of the proteins and lipids in highly extended human RBC membranes. At the entrance to the micropipette, the cytoskeleton is condensed above its equilibrium

density. However, the cytoskeleton density decreases steadily along the surface of the RBC that is pulled into the tube and is below the equilibrium density at the end or "cap" of the extended segment. This variation of the surface density of the spectrin network along the projection inside the tube indicates that the cytoskeletal network is, indeed, compressible and also that the response of the network depends on the kind of stress fields under which it is placed. One can easily see this response by pushing a finger into a loosely woven fabric (*e.g.*, a sock). Complementary to the above experiments, computer simulations of two-dimensional triangulated networks have shown that the elastic moduli are stress-dependent (Boal *et al.*, 1993).

Our investigation into the elastic properties of the reference cytoskeleton network has been based on the assumption that the rest state (free-flowing biconcave form) of the RBC is not under stress. It has been observed that a "prestress" exists in the membrane cytoskeleton of aging human erythrocytes (Mohandas and Groner, 1989). By this we mean that the normal resting state of the cytoskeleton may be in a predetermined stressed state. This effect could arise from the loss of membrane area as the erythrocyte ages. We will present a detailed investigation of the effects on the geometrical and elastic properties (due to finite deformations) of networks whose resting state may be either prestressed or stress-free.

In Sec. 3.2, we analyse the effect of finite stresses (applied

isotropically) on the geometry of the network with n_{seg} = 32, while in Sec. 3.3, the effect on the elastic properties is probed. Sec. 3.4 discusses the response of the network to stresses applied unixially and Sec. 3.5 looks into the effect of incorporating a precompression into the cytoskeletal network (changing n_{seg} from 32 to 14). The chapter ends with a summary of the results in Sec. 3.6.

3.2 Cytoskeleton network under isotropic stress - geometry

In this section, we study the effects of applying stresses to our model network for which n_{seg} = 32. To put the network under isotropic stresses in a computer simulation (that is to apply a lateral tension on the network), the value of the lateral pressure, P, is set to some non-zero values. Negative and positive values of P lead to extension and compression of the network, respectively. While under the applied stress, a simulated network is allowed to relax for several million Monte Carlo steps before data samples are recorded. The network observables that are sampled include the simulation box lengths, L_x and L_y, the average bond length of a segment in a particular configuration $<b>$, the mean in-plane area $<A>$, and also the mean displacement $<t>$ of the network above the bilayer.

Because a spectrin chain at zero stress has an end-to-end distance of approximately 70 nm, which is about 1/3 of its contour length, the cytoskeleton network may undergo considerable

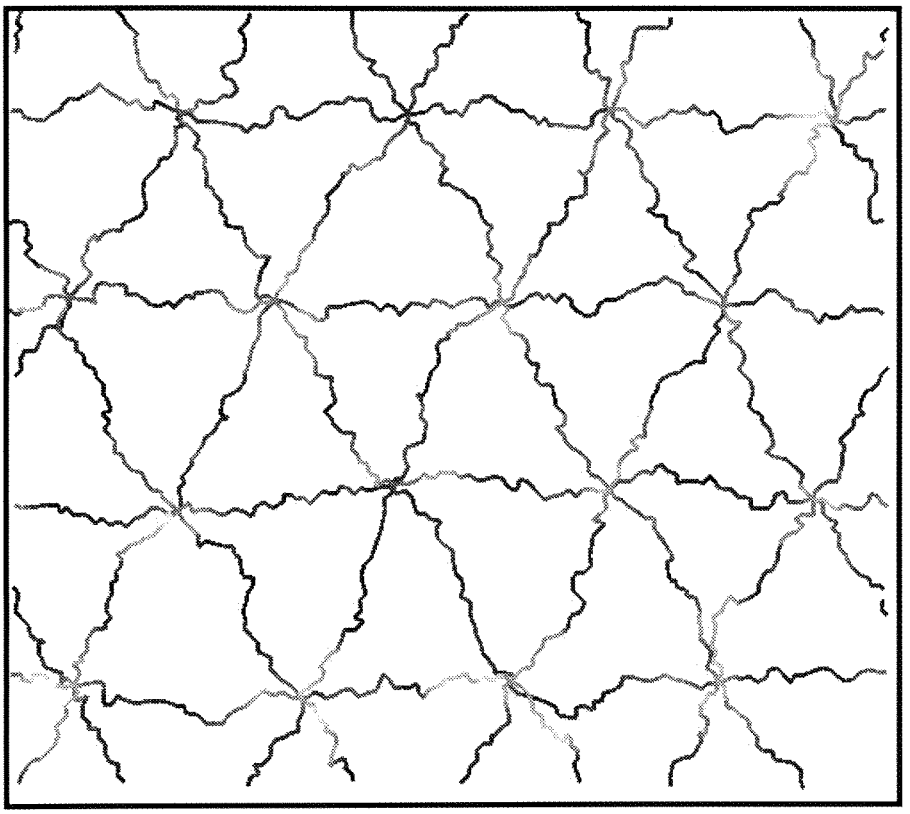

(a)

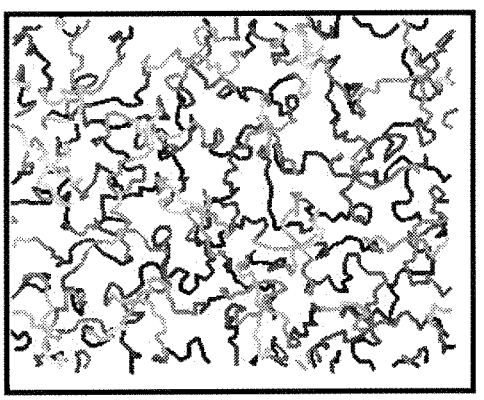

(b)

Fig. 3.1 (a) Reference Model network under extension, $-\beta P\sigma^2 = 0.2$. The chains are clearly stretched out by the tensile forces. (b) The same network under compression, $-\beta P\sigma^2 = -0.2$. Note that the chains are highly convoluted and the density of vertices is clearly much higher than in (a). ($n_{seg} = 32$).

expansion when subjected to lateral tensions. Fig. (3.1) shows two configurations drawn from the simulation at values of $\beta P\sigma^2$ equal to 0.2 (compression) and −0.2 (extension). Both diagrams are drawn to the same scale, and the difference in network density is obvious: at $\beta P\sigma^2 = 0.2$, the network is approximately 6 times as dense as it is at $\beta P\sigma^2 = -0.2$.

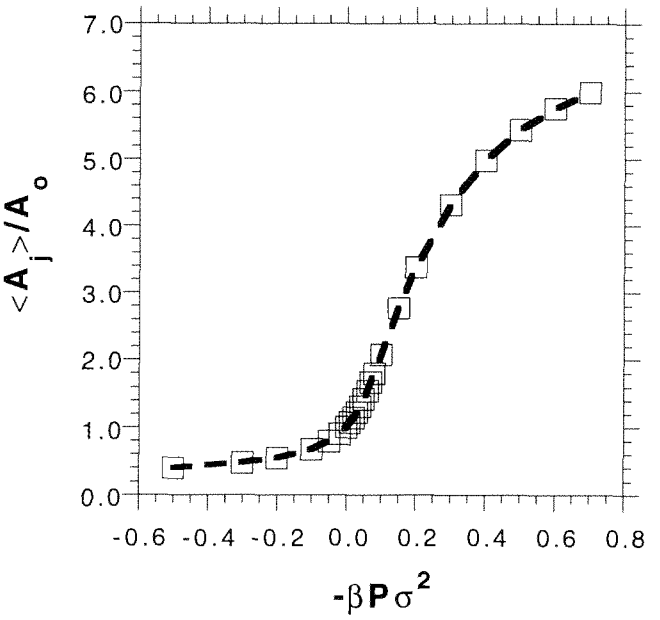

Fig. 3.2 Ratio $\langle A_j\rangle/A_0$ of the network area $\langle A_j\rangle$ to reference area A_0 (at zero stress) as a function of in-plane pressure P. Notice that the graph flattens out at both large extension ($P < -0.5$) and high compression ($P > 0.5$). ($n_{seg} = 32$).

Recent micropipette aspiration experiments on intact red cell membranes (Discher *et al.*, 1994) have shown that the area of the red cell network in reversible deformation can range from 0.5 to 4 times its unstressed area ($P = 0$), depending on the magnitude of the

aspiration pressure. Our simulations (see Fig. 3.2) cover much of this range. There are several distinctive features to Fig. 3.2. Under compression, the network area per junction vertex decreases very slowly, reflecting the importance of steric interactions between network vertex elements. At large extensions ($\beta P\sigma^2 \geq -0.7$), the ratio $<A_j>/A_o$ approaches its geometric limit of seven.

These observations can be understood in the following way. Consider first the case of the network under compression. As the compressive stress builds up, tending to "squeeze" the network, the reduction in the area is resisted by the constraint that chains are sterically forbidden to cross one another. The chains can move in the transverse direction; but, the network/bilayer attachment limits this movement (see Fig. 3.3II[b]). On the other hand, when the network is placed under a tension, it expands monotonically, although the rate of expansion (rate of increase of in-plane area with increase in applied stress) decreases. This effect is due to the individual chains reaching their contour length, equal to $n_{seg}\bullet(0.97\sigma)$. The small stress regime ($-0.08 \leq -\beta P\sigma^2 \leq 0.08$) is discussed further in Sec. 3.3.

The mean displacement $<t>$ of the network above the bilayer is shown as a function of pressure in Fig. 3.3(I). As expected, the trends in $<t>$ are the reverse of those of the mean network area per junction vertex $<A_j>$ (see Fig. 3.2): $<t>$ is largest under compression and decreases monotonically with increasing tension. For pressures more negative than $-\beta P\sigma^2 = 0.7$, $<t>$ approaches the value 0.5σ, which corresponds to approximately 3.2 nm, or a network thickness of

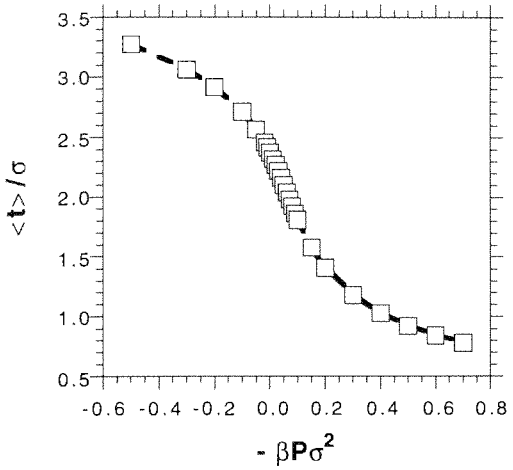

(I)

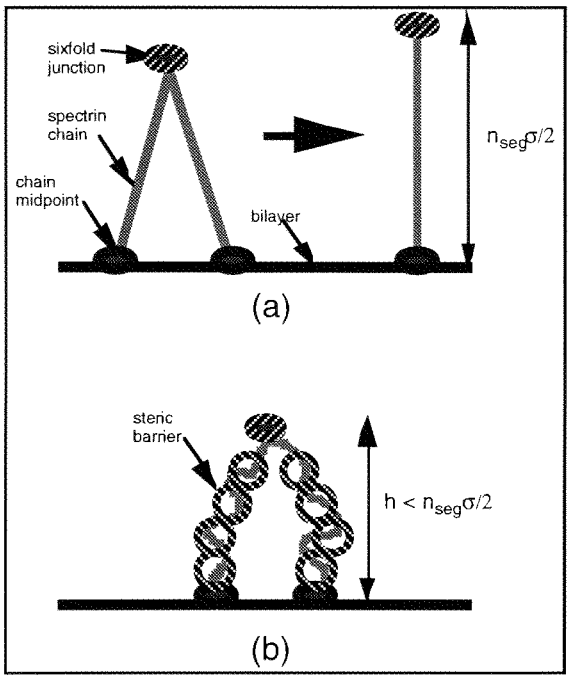

(II)

Fig. 3.3 (I) Mean network displacement $<t>$ as a function of in-plane pressure P. Notice that the graph tapers off at both large tensions and at high compressions, consistent with the behavior of Fig. 3.2. Notice also that the lower bound to $<t>$ is approximately 0.5σ or 3.2 nm. (n_{seg} = 32). (II) Diagram showing the effect of steric interactions among the chain elements on limiting the mean displacement of the chain above the bilayer. Bold horizontal line represents the bilayer. (a) When no sterics are present, the two chains (each of N links) can overlap and the thickness (equal to $2<t>$) can theoretically reach $n_{seg}\sigma/2$. (b) Circles indicate steric barriers which force the chains apart. Note that $n_{seg}\sigma/2 >$ h, where h is the displacement of the sixfold junction from the bilayer.

roughly 1σ or 6.4 nm. This lower bound on $<t>$ is due to each individual vertex of the chain, bouncing off the bilayer elastically, thus preventing them from actually reaching the bilayer (see Chapter 2). The effect of the steric barriers which prevent chains from crossing each other is illustrated in Fig. 3.3(II[b]).

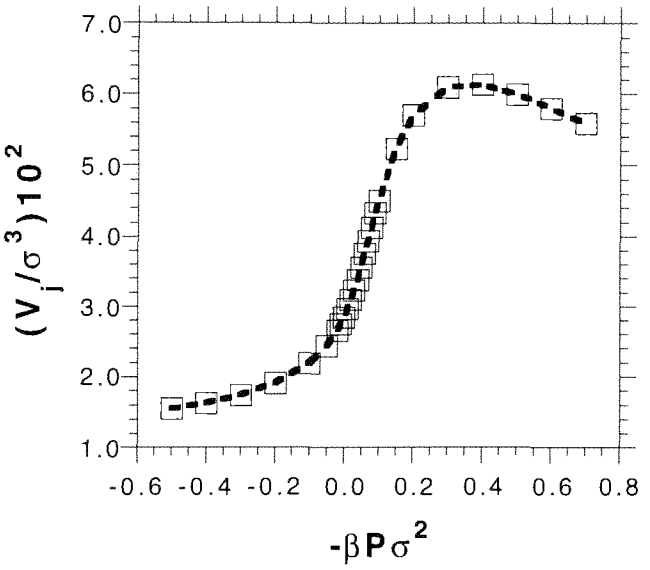

Fig. 3.4 Network volume per junction vertex V_j as a function of in-plane pressure P. The graph shows that V_j increases monotonically, from the compressed region to the extended region. It then decreases again at roughly $-\beta P\sigma^2 > 0.35$. ($n_{seg} = 32$).

A measure of the cytoskeleton network volume can be obtained by taking the product of the area per junction vertex with the network displacement t for each configuration of the sample. Fig. 3.4 clearly shows that the volume per junction vertex V_j increases as the network is extended from its equilibrium state at zero stress. The volume reaches a maximum at $-\beta P\sigma^2 \sim 0.35$ before decreasing at high tension. This indicates that, as one moves from the compressed region to the extended region, the in-plane area increases faster than the thickness $2\langle t \rangle$ can decrease.

Sec. 3.3 Effect of stress on network elastic moduli

The in-plane elastic moduli K_A and μ are extracted via fluctuations (see Appendix D) and are shown in Fig. 3.5 for the pressures that were investigated. The compression modulus K_A has a minimum around $-\beta P\sigma^2 = 0.1$, and is significantly larger when the

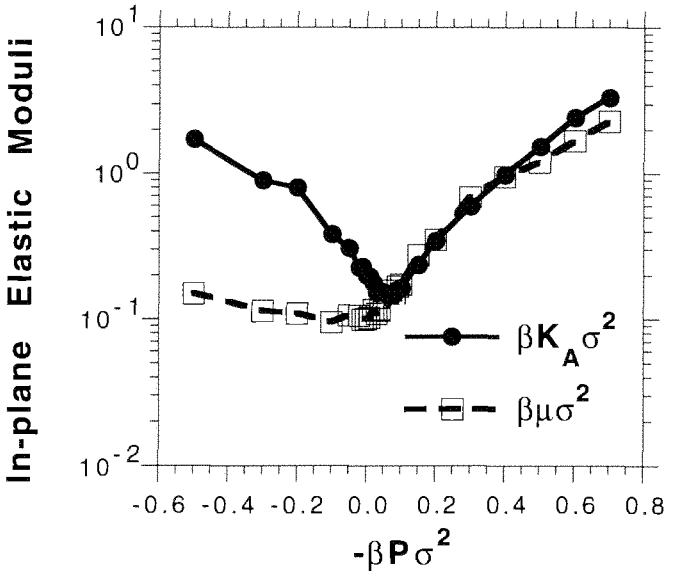

Fig. 3.5 Network in-plane elastic moduli as a function of in-plane pressure P. Note that both K_A and μ increase monotonically as the network is placed under tension. Under compression, only K_A increases significantly but not μ. (Network has $n_{seg} = 32$).

network is placed under compression or tension. When the network is compressed, steric effects become increasingly important, and, thus, resist the decrease in the in-plane area. This in turn leads to an increase in K_A. One should note that the observed increase in K_A

during compression is realized only in the simulations as described, since real membranes would crumple (or at least begin to crease) under compression. On the other hand, when the network is placed under a significant tension, the built-in tether constraints resist the network being stretched beyond $<A_j>/A_0 = 7$, where A_0 is the zero-stress network in-plane area per junction vertex. This results in an increasing K_A at large network extensions.

The shear modulus μ shown in Fig. 3.5 shares several characterstics with K_A: (a) The shear modulus increases monotonically when the network is placed under tension. This is due to the network resisting shear by the triangular tether constraints. (b) However, μ does not increase significantly over the range of compressive stress we have examined. This is not unexpected, since tether constraints are only important for in-plane deformations when the network is under tension and not compression.

Can the simulation results for in-plane geometrical and elastic properties be described in a simple way? To answer this, we consider a simple mean-field model of a two-dimensional network of springs proposed by Boal, Seifert and Shillcock (1993). In this model, the potential energy of an individual spring is given by

$$U_{HL} = (1/2)\, k\, (s - s_0)^2, \qquad (3.1)$$

where k is the spring constant, s is the variable length of the spring and s_0 is the equilibrium length of the spring. If all springs have the

same length, the geometry and in-plane elasticity of a network of two-dimensional springs is described by:

$$\langle A_j \rangle / A_o = (1 + P/\sqrt{3}k)^{-2} \tag{3.2}$$

$$K_A/k = \sqrt{3}(1 + P/\sqrt{3}k)/2 \tag{3.3}$$

$$\mu/k = \sqrt{3}(1 - \sqrt{3}P/k)/4, \tag{3.4}$$

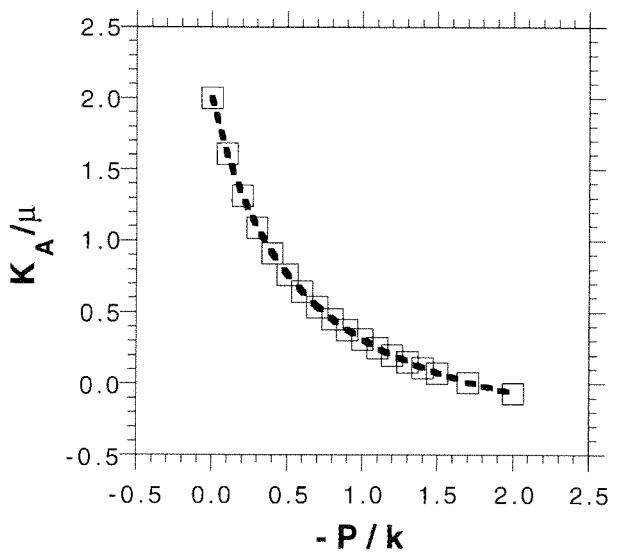

Fig. 3.6 The ratio K_A/μ as a function of the applied pressure P for a two-dimensional triangulated network of springs in the mean field limit. K_A/μ is a strictly decreasing function of $-P$ for the range of values of P shown. This implies that the Poisson ratio of such a network eventually becomes negative at large enough tensions.

where $A_o = \sqrt{3}s_o^2/2$. Eqs. (3.2) to (3.4) predict that, when the network is placed under tension: (a) The network will expand; (b) K_A

will decrease; (c) μ will increase. At zero pressure, the ratio $K_A/\mu = 2$, as expected for a harmonic network of springs. Fig. 3.6 shows that K_A/μ is a strictly decreasing function of the stress for triangular networks at low temperaure and eventually becomes smaller than 1, which implies that the Poisson ratio is negative at large tensions. These predictions are valid only in the small fluctuation limit (i.e., for a low temperature network), corresponding to the criteria that $\beta k s_0^2 \gg 1$. Another feature of this model is that it does not describe networks under moderate compression, since the ideal triangular spring network undergoes a collapse transition for $P > (\sqrt{3}\ /\ 8)k$ (Discher, Boal and Boey, 1997).

We now return to see if Eqs. (3.2)-(3.4) describe our cytoskeletal network model. At zero stress, the ratio $K_A/\mu \approx 2.4$ in the reference model (see Fig. 3.5), which is consistent with that predicted for the ideal two-dimensional spring network above. Fig. 3.7 (below) shows the behaviour of the ratio K_A/μ with respect to variation in the applied stress. K_A/μ is greater than unity for $\beta P \sigma^2 > 0$ and then approaches 1 as the network goes from the compressed state into the extended state. In the region, $0.1 \leq -\beta P \sigma^2 \leq 0.4$, K_A/μ stays around the value of (1.00 ± 0.13) before it starts increasing again for $-\beta P \sigma^2 \geq 0.4$. This implies that the Poisson ratio is initially positive at low tension and decreasing as the tension increases. It becomes (weakly) negative and then goes back to being positive again. This behavior of the Poisson ratio is shown in Fig. 3.7(b) and is expected since the Poisson ratio in two-dimensions is $(K_A/\mu - 1)/(K_A/\mu + 1)$ (see Landau and Lifshitz, 1968).

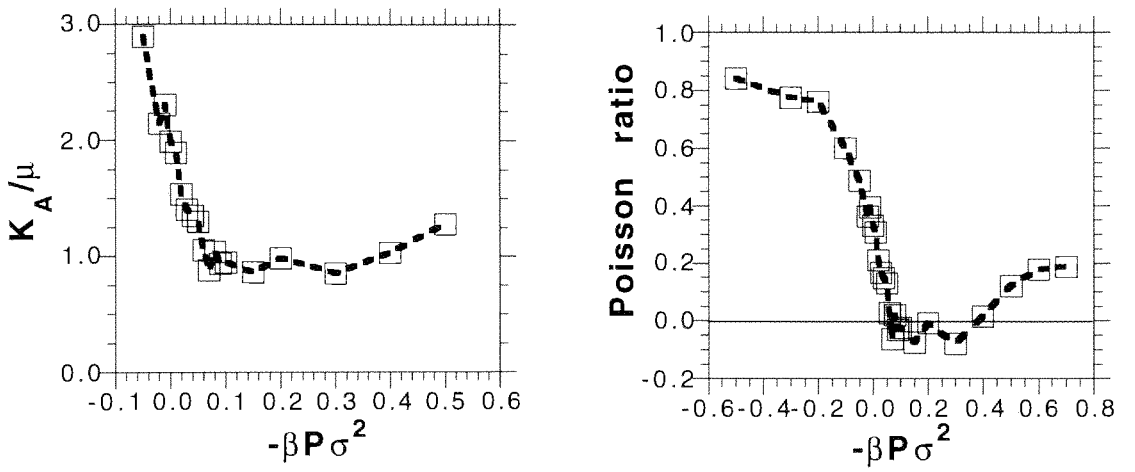

(a) (b)

Fig. 3.7 (a) K_A/μ as a function of in-plane pressure P. Note that K_A/μ starts off positive and decreases as the network goes from being compressed to being extended, eventually becomes less than one and increases again after that. (b) Poisson ratio as a function of in-plane pressure P. The horizontal bold line shows clearly that the Poisson ratio does go negative but only weakly. (n_{seg} = 32).

Fig. 3.8 shows that $<A_j>^{-1/2}$ is a linear function of the tension (to a good approximation) in the small deformation regime, which is a good indication of the harmonic response of the cytoskeletal network at small stresses. The line through the data points is a mean field fit (see Eq. (3.2)), in which the slope $(\sqrt{3}\beta k\sigma^2)^{-1}$ is observed to be approximately equal to 3.13 or, equivalently, $\beta k_{eff}\sigma^2 \approx 0.20$, where k_{eff} is the effective spring constant of an equivalent ideal triangulated network. Since σ = 6.4 nm, this implies that $k_{eff} \approx 2 \times 10^{-5}$ J/m^2.

Fig. 3.9 shows the variation of K_A and μ at small stresses. Both

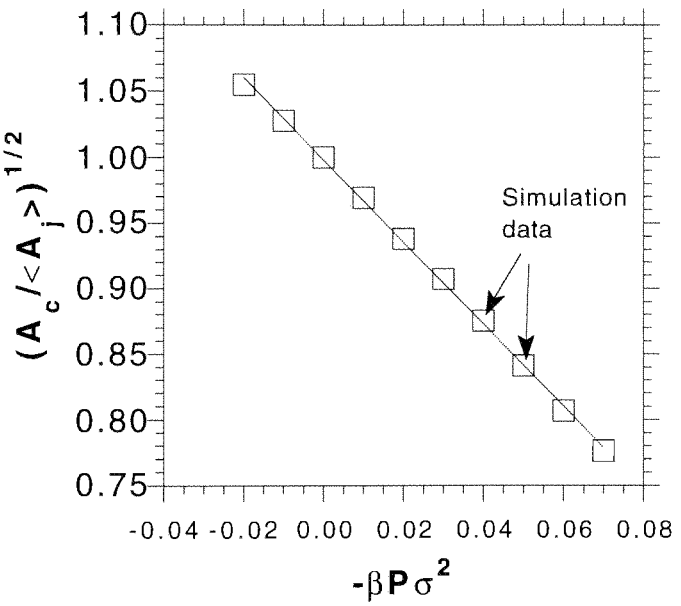

Fig. 3.8 Plot shows $\langle A_j\rangle^{-1/2}$ is a linear function of the applied pressure. The line through the data points is the mean-field fit given by Eq. 3.2. (n_{seg} = 32).

K_A and μ are observed to be approximately linear in the pressure P. The solid line is the linear fit (see Eq. (3.3)) to the K_A data and gives $\beta k_{eff}\sigma^2 \approx 0.2$, while the dashed line (see Eq. (3.4)) is the linear fit to the μ data which also gives $\beta k_{eff}\sigma^2 \approx 0.2$. These two results provide a self-consistency check for our simulation results. Furthermore, the fluctuations of the sixfold junctions around their mean positions can be compared with those of those of an equivalent two-dimensional triangulated network of springs and found to be consistent with $\beta k_{eff}\sigma^2 = 0.20$ (private communications with Boal, 1996).

The mean area per junction at zero stress A_0 is found to be $120\sigma^2$ corresponding to an interjunction length s_0 of approximately 11.8σ. Thus each chain in the network, in terms of the interjunction

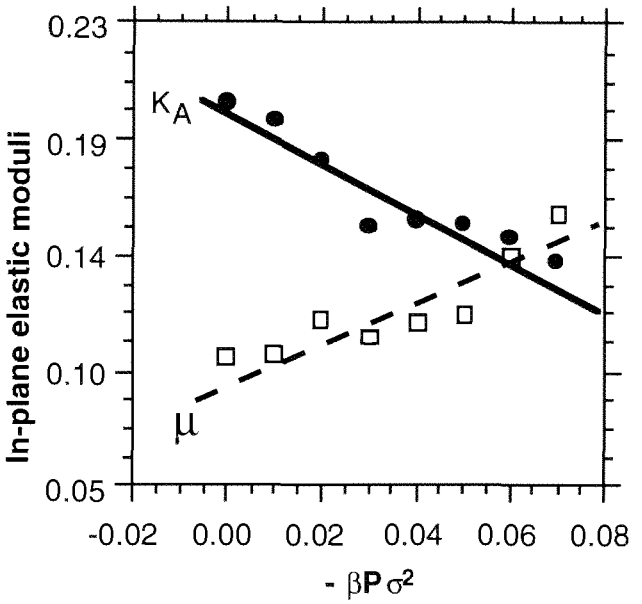

Fig. 3.9 Elastic moduli K_A and μ as a function of the pressure P. The solid and dashed lines are the mean field fits to the K_A and μ data respectively. (n_{seg} = 32).

$\beta k_{eff} s_o^2 \approx 32$. This spring constant is large and corresponds to small fluctuations in the interjunction spacings.

At large tensions, the network is observed to be stretched significantly and the transverse motion of the chains is highly restricted compared to the small stress regime. Entropic effects are, thus expected to be less important in comparison to the energetics of the chains in determining the elasticity of the network. The triangles (formed by three neighbouring sixfold junctions) are also observed to have approximately the same shape (equilateral on average; see Fig. 3.10). This observation leads to the proposition that the network at large deformations can be modeled by a two-dimensional

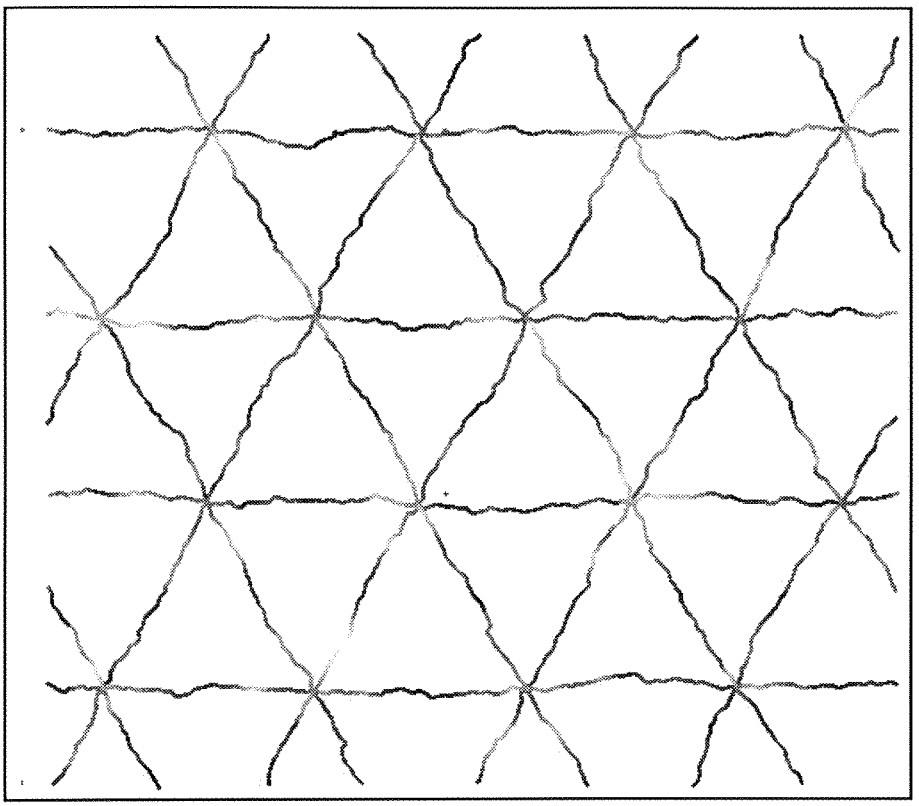

Fig. 3.10 Picture of a highly stretched network ($-\beta P\sigma^2 = 0.7$). Notice that the triangles are approximately the same equilateral shape. ($n_{seg} = 32$).

triangulated network whose junctions interact with their nearest neighbours via a square-well potential (for a review on such networks, see Boal, 1994). In a mean field approach in which all triangles have the same equilateral shape, the area $<A_j>$ at large deformations can be shown to vary (see Appendix C) with the applied stress P in the following way:

$$<A_j> \approx 1/\beta P\,[1 + \beta P A_m], \qquad (3.5)$$

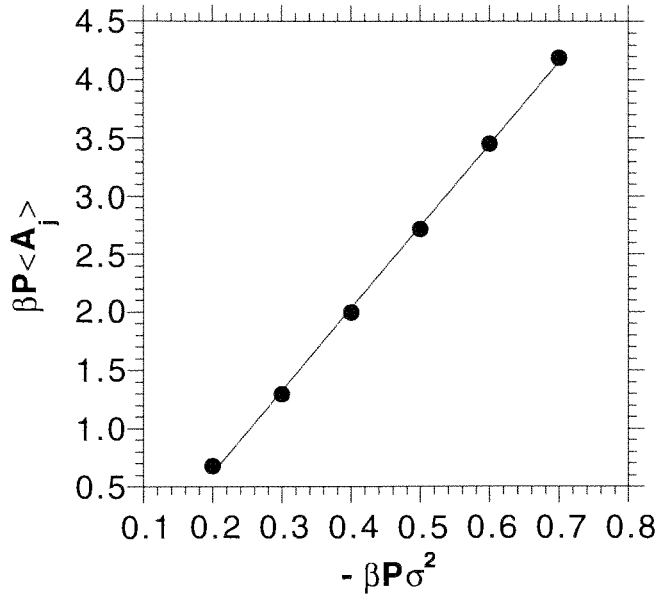

Fig. 3.11 Plot of $\beta P<A_j>$ versus $-\beta P\sigma^2$. Open squares represent the simulation data and the line running through the data points is the mean field fit where the network is assumed to be made up of identical equilateral triangles. (n_{seg} = 32).

where A_m represents the maximum area attainable by any triangle in the network and $P < 0$ represents a tension. Eq. (3.5) can be applied to the simulation data (Fig. 3.11) and yields a value for A_m of approximately 7, which is consistent with the fact that our cytoskeletal network model is built on the criterion that the ratio $<A_j>/A_c$ = 1/7.

The out-of-plane elastic moduli, the volume compression modulus K_V and the transverse Young's modulus $Y_\perp$, are shown in Fig. 3.12. The volume compression modulus K_V displays a minimum near zero stress, while increasing as the network is placed under either a tension or a compression (the origin of this behaviour is the

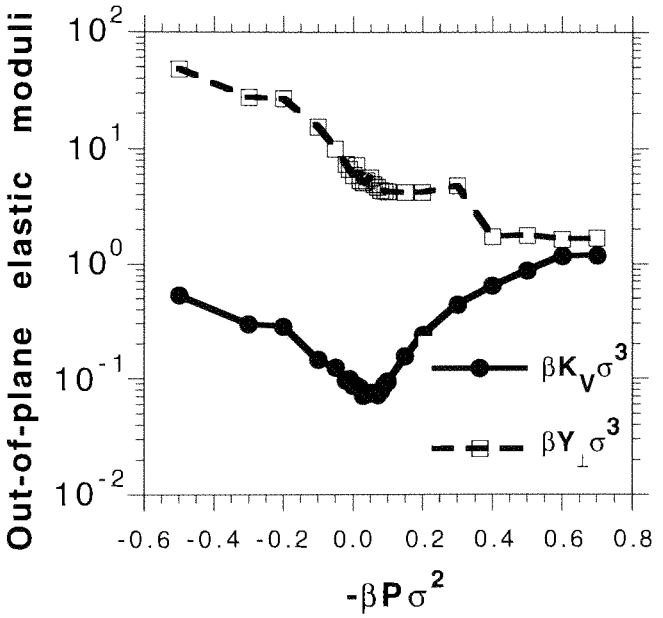

Fig. 3.12 Network out-of-plane elastic moduli as a function of in-plane pressure P. K_V has a minimum near zero stress and increases monotonically on both sides of this minimum, while $Y_\perp$ decreases monotonically with increasing $-\beta P\sigma^2$. (Data for n_{seg} = 32).

same as that of K_A under stress). Fig. 3.12 shows the transverse Young's modulus $Y_\perp$ to be significantly larger than K_V in most part of the range of P. As was explained earlier in Chapter 2, values of $Y_\perp$ extracted via a MC method (private communications with Boal, 1997), gave a mean square difference in $<t>$ to be an order of magnitude larger than that in the MD/MC case. We believe this difference to be the cause of the significantly large values of $Y_\perp$ in our simulations. The MD part of the simulation algorithm (see Chapter 2) seems to quench out the fluctuations in the mean displacement $<t>$.

Sec. 3.4 Anisotropy of the cytoskeletal network

The anisotropic response of two-dimensional triangulated networks at large deformations has been demonstrated for square-well-type interactions between network junctions (Discher *et al.*, 1997). Under substantial network deformation (when strains are about 90% of their allowed maximum), the stress/strain relation in one of the principal directions is found to be different from that in the orthogonal direction.

We have probed our cytoskeleton network for the same kind of anisotropic response. In our cytoskeleton simulations, we apply a non-zero stress in a chosen direction (x or y) and set to zero the stress in the orthogonal direction. Figs. 3.13(a) and (b) compare the two states of the network under orthogonally applied stresses (x and y directions respectively); note that the chains orthogonal to the direction of the applied stress are crumpled up significantly and forced to move into the space above the bilayer (indicated by the light shading). The lengths of the simulation box orthogonal to the applied stress, as shown in Figs. 3.13(a) and (b), are less than their respective rest-state values; that is, the network shrinks in the direction orthogonal to the applied stress. This is analogous to the scenario when one pulls hard longitudinally on a rectangular piece of rubber strip, and observes that the rubber shrinks transversely (corresponding to a positive Poisson ratio).

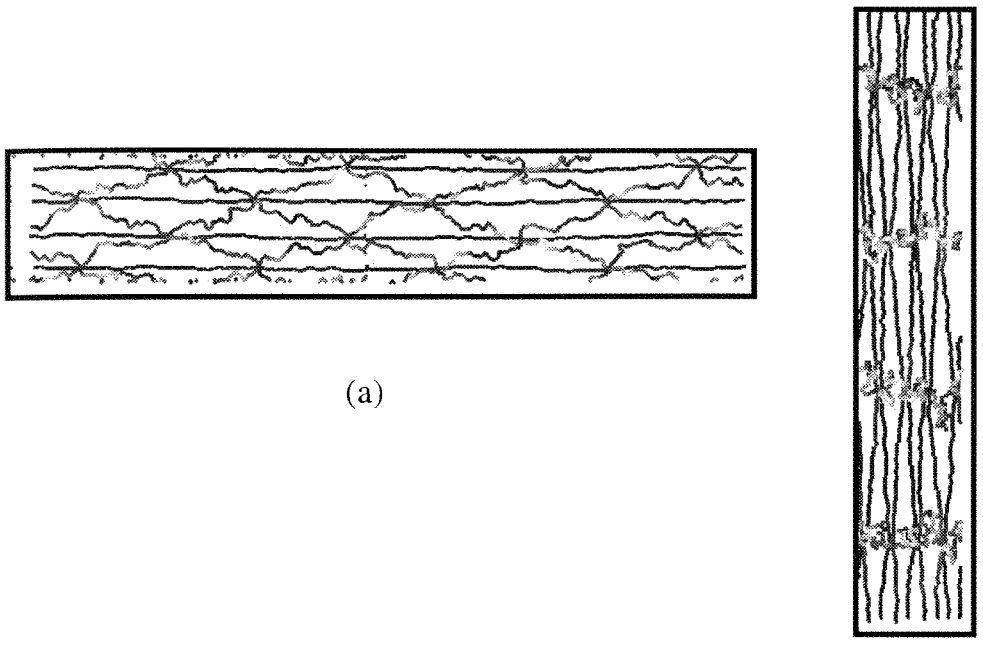

(a)

(b)

Fig. 3.13 Two states of our cytoskeleton network under orthogonally applied uniaxial stresses. (a) Stress applied only in the x-direction. (b) Stress applied only in the y-direction. Notice the chains orthogonal to the applied stress are crumpled up, while along the stress direction, the chains are well stretched out. (Data for $n_{seg} = 32$).

Fig. 3.14(a) shows the response of the cytoskeleton network over a wide range of uniaxial tensions. The strain variable $\langle L_i \rangle / \langle L_i \rangle_o$ is plotted against the uniaxial stress for two directions in the periodic system: $L_i = L_x$ or L_y. A difference in the values of $\langle L_x \rangle / \langle L_x \rangle_o$ and $\langle L_y \rangle / \langle L_y \rangle_o$ would be an indication of an anisotropic response of the network to the applied uniaxial tension. One can see from Fig. 3.14(a) that there is very little anisotropy present up to factors-of-two change in the periodic box length. After this point is reached, $\langle L_y \rangle / \langle L_y \rangle_o$ rises faster than $\langle L_x \rangle / \langle L_x \rangle_o$. This is expected from the geometry of the network. As seen in Fig. 3.14(a), the chains in the

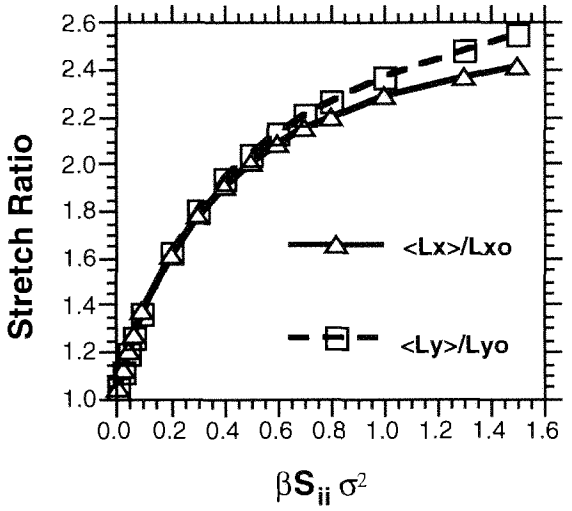

(a)

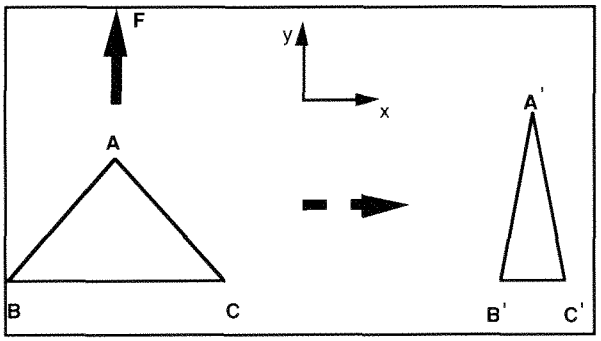

(b)

Fig. 3.14 (a) The stretch ratio $<L_i>/<L_i>_0$ (i=x or y) plotted against the uniaxially applied stress $\beta S_{ii}\sigma^2$. Note that the stretch ratio is in the same direction as the applied stress. Anisotropy appears only at stretch ratios $<L_i>/<L_i>_0 \approx 2$. (Data for $n_{seg} = 32$). (b) Diagram shows how shrinking the base BC of a triangle to B'C' (by applying a vertical force F) without changing the sides AB/AC can increase the height. This is the main reason why the stretch ratio for y-axis uniaxial tension rises faster than the corresponding stress/strain relation in the x-direction (in the region where the anisotropy is present).

direction of the x-axis are close to their maximum tether constraint and thus provide strong resistance to further extension. When the

uniaxial tension is along the y-axis, the network can extend in two ways: (1) Stretching the diagonal chains as one would expect. (2) Shrinking the lateral distance between the junctions forming the base of the triangles in the network (see Fig. 3.14(b)). Note that, due to the triangulated geometry of the network, the effect described in (2) does not cause the stretch ratio $\langle L_x \rangle / \langle L_x \rangle_o$ to increase when the uniaxial stress is applied in the x-direction.

For small uniaxial stresses, we find that the strain parameter (defined as $[\langle L_i \rangle / \langle L_i \rangle_o - 1]$) is a linear function of the applied stress $\beta S_{ii} \sigma^2$. This is shown is Fig. 3.15(a,b). The bold line is the linear fit to the simulation data at small stress. The slope of that line is the inverse of the Young's modulus (denoted by $\beta E_i \sigma^2$). The slope of the line in Fig. 3.15(a) (uniaxial tension applied along x-direction) is approximately equal to 4, which implies that $\beta E_x \sigma^2 \approx 0.25$. We can calculate the effective spring constant of the chains k_{eff}, according to

$$\beta k_{eff} \sigma^2 = \beta E_i \sigma^2 \sqrt{3}/2, \tag{3.6}$$

which gives a value for $\beta k_{eff} \sigma^2 = 0.22$. The linear fit in Fig. 3.15(b) (for tension applied along the y-direction) yields a value for $\beta k_{eff} \sigma^2 = 0.23$. These two results for k_{eff} provide a consistency check for the effective spring constant extracted from the isotropic-stress simulations in Sec. 3.2, for which $\beta k_{eff} \sigma^2 \approx 0.2$.

The Poisson ratio ρ, which provides yet another check on the

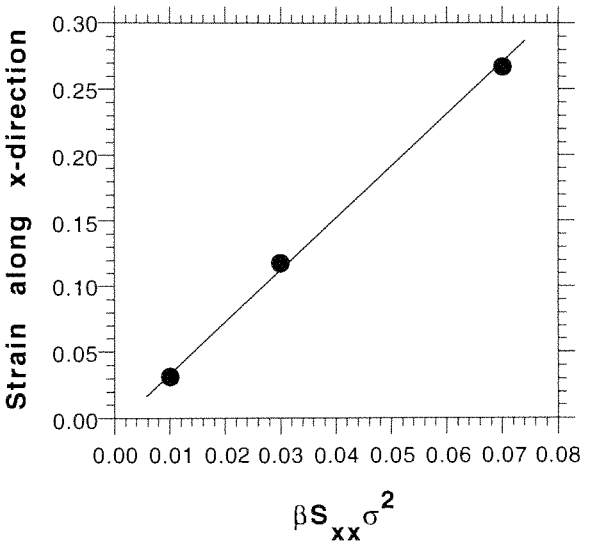

(a)

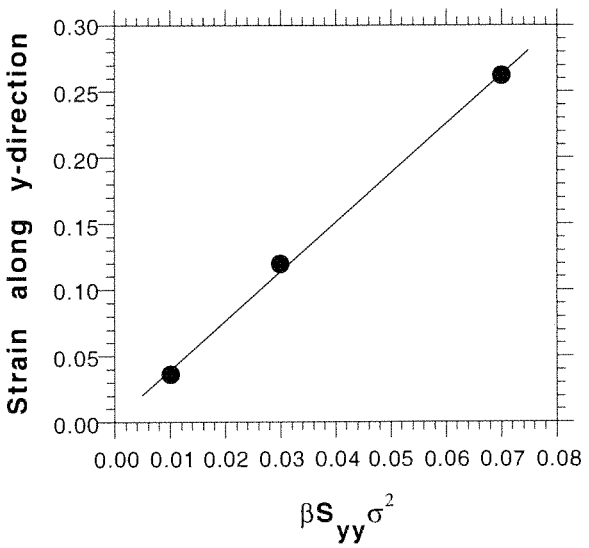

(b)

Fig. 3.15 Plot of the stress-strain relation under uniaxial stress: (a) Measured along x-direction as a function of the stress in x-direction. (b) Measured along y-direction as a function of the stress in y-direction. Note that there is little difference between the two principal directions (x and y). Slope of bold lines is the inverse of the Young's modulus.

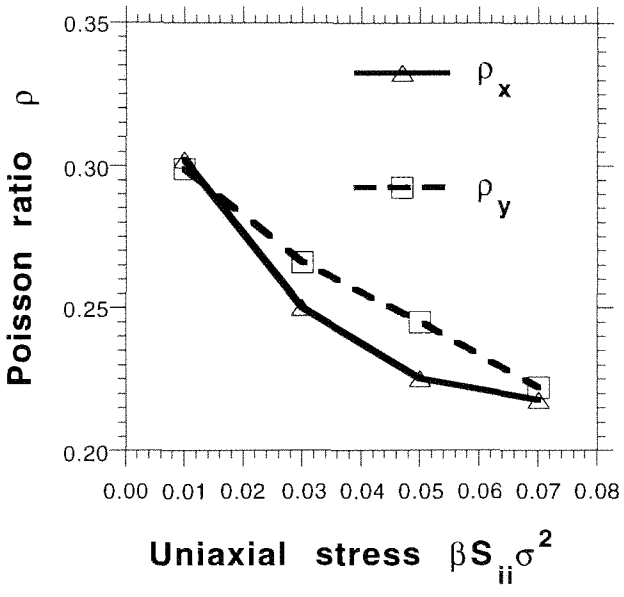

Fig. 3.16 The Poisson ratio ρ as a function of the uniaxial stress: ρ_x corresponds to a stress is along the x-axis and ρ_y denotes the Poisson ratio for a stress along the y-axis.

consistency of our simulations, can be calculated via the formula (see Lai, Rubin and Krempl, 1987), $\rho_i = (1 - \lambda_c)/(\lambda_e - 1)$, where $\lambda_c = [<L_j>/<L_j>_o - 1]$ (less than one), $\lambda_e = [<L_i>/<L_i>_o - 1]$ (greater than one), i denotes the direction (x or y) in which the uniaxial tension is applied, and j is the respectively orthogonal direction (y or x). Fig. 3.16 shows that the zero stress limit of the Poisson ratio ρ_o is approximately the same in both directions of the applied uniaxial tensions and lies in the range 0.31–0.35. This is again consistent with the isotropic-stress simulations in which the measured value of the ratio K_A/μ at zero stress corresponds to ρ_o of approximately 1/3.

Sec. 3.5 Prestress in the cytoskeletal network

It has been suggested over the past couple of decades that the red cell density grows with increasing cell age while in circulation within the human blood system (Mohandas and Groner, 1989). This led to the use of density separation of red cells (for example, ultracentrifugation) in the study of red cell aging. It has been observed (Mohandas and Groner, 1989) that, as the red cell density increases, there is a loss of membrane surface area and a corresponding decrease in cell voume (leading to an increase in cell hemoglobin concentration), which also causes the cells to be more spherical. This ultimately compromises the red cell's ability to deform. A loss of cell surface area without a corresponding loss of spectrin protein implies that the cytoskeleton in aging cells is under a compressive stress; we call such cytoskeletons "prestressed". The extent to which normal RBCs are prestressed is not known.

In this section, we explore the consequences of modifying our model network of the cytoskeleton by placing the rest state of the network under a prestress (or precompression). As was shown in Chapter 2, the ratio $A_c/\langle A_j\rangle^{ref}$ ($\langle A_j\rangle^{ref}$ is the reference rest-state area per junction vertex) increases with n_{seg}. It was determined in the stress-free model that n_{seg} must be 32 in order that $A_c/\langle A_j\rangle^{ref} = 7$. It is possible to achieve the requirement that $A_c/\langle A_j\rangle^{ref} = 7$ for $n_{seg} < 32$; but, the reference rest-state area $\langle A_j\rangle^{ref}$ must be that of a compressed or prestressed state. Corresponding to each prestress

(denoted as $-\beta \Pi_{ps} \sigma_{ps}^2$, where σ_{ps} is the lengthscale in the prestress model), there is a value of n_{seg} that satisfies $A_c/\langle A_j \rangle^{ref} = 7$. Because of the increase in statistical error when evaluating ensemble averages for small n_{seg} (< 14), we choose $n_{seg} = 14$ as a limiting case. Since the spectrin chain has a contour length of 200 nm, $n_{seg} = 14$ corresponds to assigning σ_{ps} the value 14.7 nm.

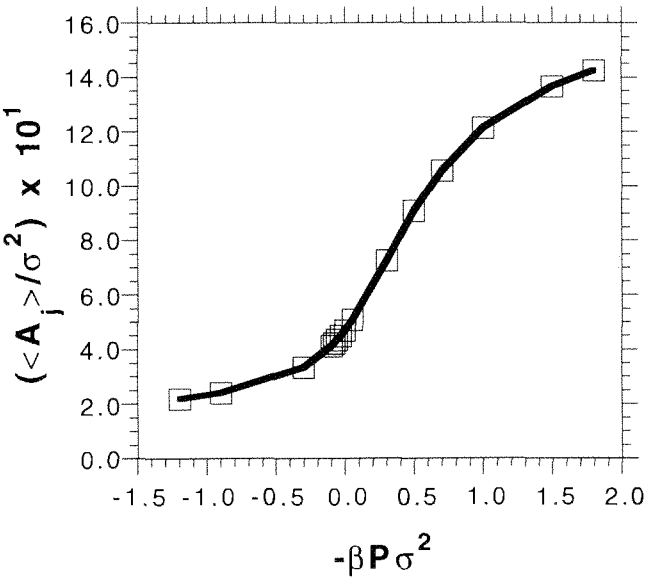

Fig. 3.17 Mean area per junction $\langle A_j \rangle$ as a function of in-plane pressure P for $n_{seg} = 14$.

To determine Π_{ps}, we need to note first that the contour area per junction A_c for $n_{seg} = 14$ is given by $(\sqrt{3}/2).(0.97 n_{seg} \sigma_{ps})^2$ or approximately 160 σ_{ps}^2. We then need to determine the mean area per junction complex of the network in the compressed state (denoted by $\langle A \rangle_{ps}$) such that the ratio $A_c/\langle A \rangle_{ps}$ has a value of approximately 7. Fig. 3.17 shows the relationship of the mean area per junction vertex as a function of the applied stress P for $n_{seg} = 14$.

We determine from Fig. 3.17 that the prestress $-\beta\Pi_{ps}\sigma_{ps}^2$ needs to be approximately equal to -1 (where the prestress rest-state area $\langle A\rangle_{ps} \approx 23\ \sigma_{ps}^2$) to achieve the ratio $A_c/\langle A\rangle_{ps} = 7$. By allowing for this readjustment in the applied stress, we define a new pressure variable, ΔP, as the difference between the externally applied pressure P and the intrinsic stress $-\Pi_{ps}$ caused by the in-plane shrinking of the bilayer

$$-\beta\Delta P\sigma_{ps}^2 = -\beta P\sigma_{ps}^2 + \beta\Pi_{ps}\sigma_{ps}^2, \qquad (3.7)$$

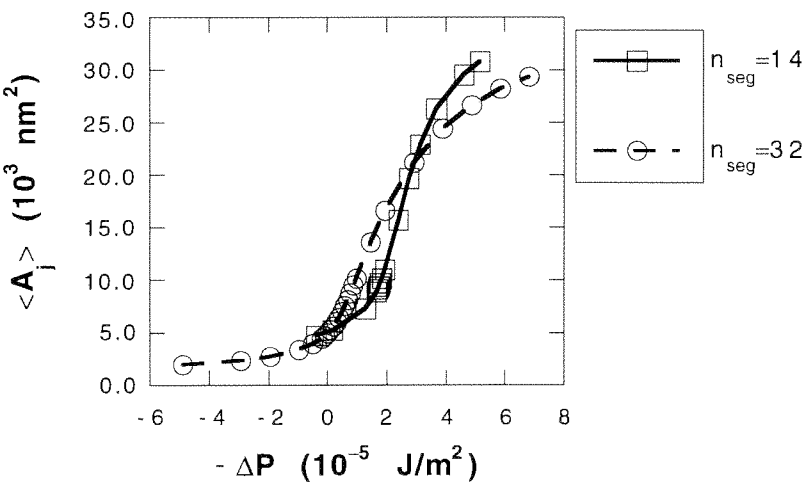

Fig. 3.18 The area per junction $\langle A_j\rangle$ as a function of the stress for $n_{seg} = 14$ (prestress incorporated) in comparison with the stress-free model ($n_{seg} = 32$). Although the two curves share the same x-axis, the $n_{seg} = 14$ case has a built-in precompression equal to 1.85 x 10^{-5} J/m^2.

where $\Delta P = P$ for $n_{seg} = 32$, since there is no precompression in the stress-free model. We find in Fig. 3.18 (which incorporates the physical unit conversions, $\sigma = 6.4$ nm and $\sigma_{ps} = 14.7$ nm), that the

prestress and stress-free cases have similar qualitative features, but differ quantitatively. The in-plane area of the prestress case rises more steeply than the stress-free case for tensions larger than 2 x 10^{-5} J/m^2.

As with the stress-free model, we can extract an effective spring constant $(k_{eff})^{ps}$ for the prestress model at small applied stresses (taken with respect to $P = 0$). This is shown in Fig. 3.19, where the bold line, which is the mean field fit to the simulation data, gives $\beta(k_{eff})^{ps}\sigma_{ps}^2 \approx 0.83$. Using the conversion $\sigma_{ps} = 14.7$ nm, we get $(k_{eff})^{ps} \approx 1.5 \times 10^{-5}$ J/m^2, which is approximately 25% smaller than that extracted from the stress-free model.

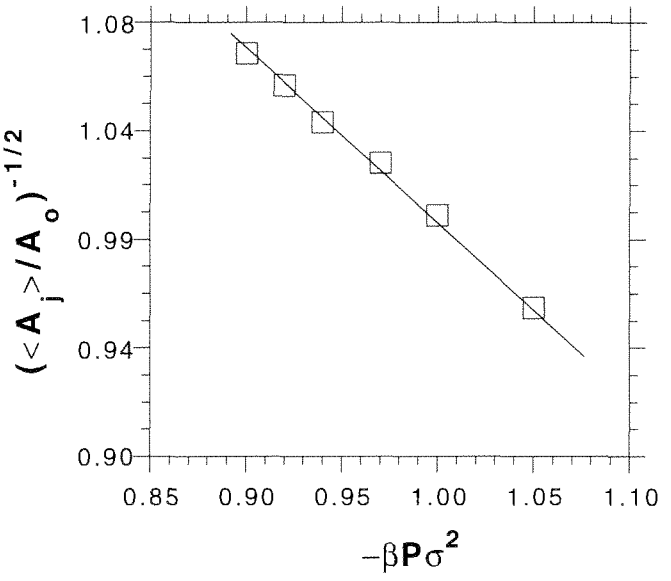

Fig. 3.19 Mean field fit (bold line) to simulation data for $n_{seg} = 14$ near $\beta P\sigma_{ps}^2 = 0$. Slope of line equals $1/(\sqrt{3}\beta k_{eff}\sigma_{ps})$.

The qualitative similarity (in the in-plane area response to stress) between the stress-free and prestress cases can also be seen in the response of the mean displacement from the bilayer $<t>$ to applied stresses, as shown in Fig. 3.20. The $<t>$ data for the n_{seg}=14 case are larger than those of the stress-free case for most of the range of ΔP. This is expected, since the prestress reference rest-state is under a precompression, while the n_{seg}=32 case rest-state is under zero stress. At large tensions ($-\Delta P > 5 \times 10^{-5}$ J/m^2), this difference in the $<t>$ data between the prestress and stress-free cases is less apparent. From Fig. 3.13, we recall that the chains in a compressed state are generally more convoluted and forced away from the bilayer. Hence, $<t>$ is expected to be larger in the prestress configuration compared to the stress-free configuration.

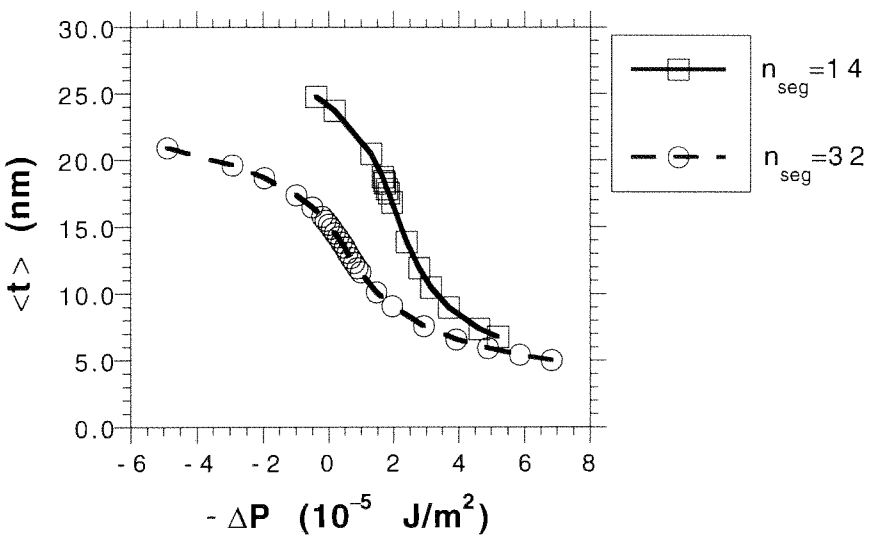

Fig. 3.20 $<t>$ as a function of the difference in stress for n_{seg} = 14 (prestress incorporated) and n_{seg} = 32 (stress-free model).

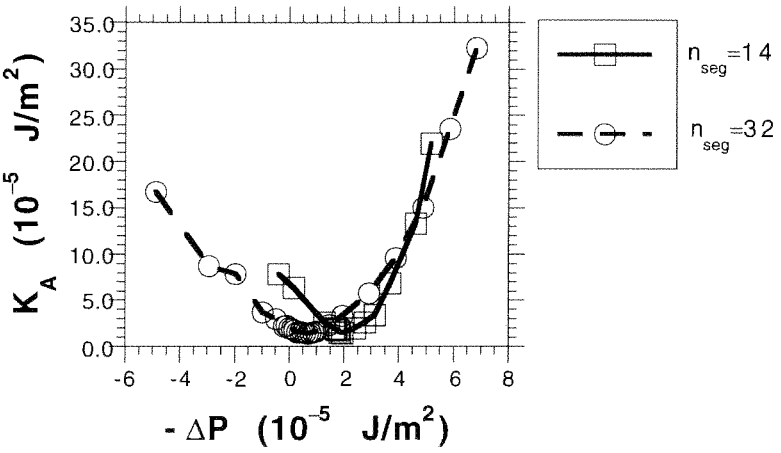

(a)

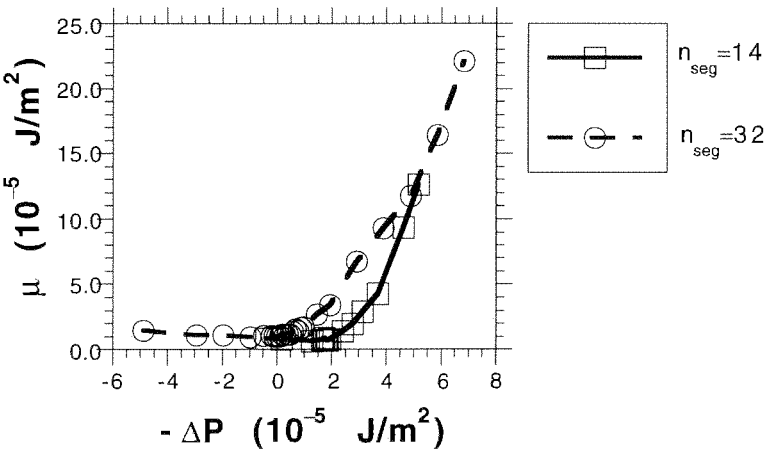

(b)

Fig. 3.21 (a) K_A as a function of stress for n_{seg} = 14 (prestress incorporated) and n_{seg} = 32 (stress-free). (b) Shear modulus μ as a function of the stress for n_{seg} = 14 (prestress incorporated) and n_{seg} = 32 (stress-free model).

We now look at the effect of precompression on the elastic moduli of the network. Fig. 3.21(a) shows that the area compression modulus K_A is generally very similar both qualitatively and quantitatively for the two models. The slightly larger values for the prestress model, in the regime where the applied stress is

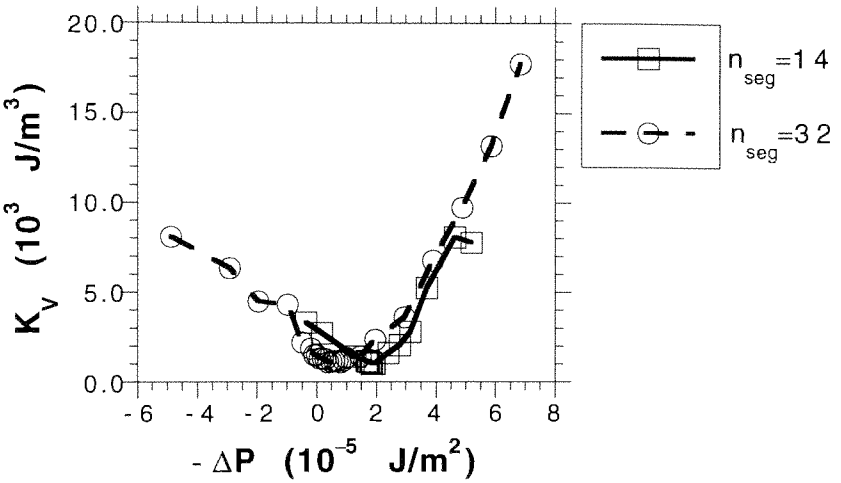

(a)

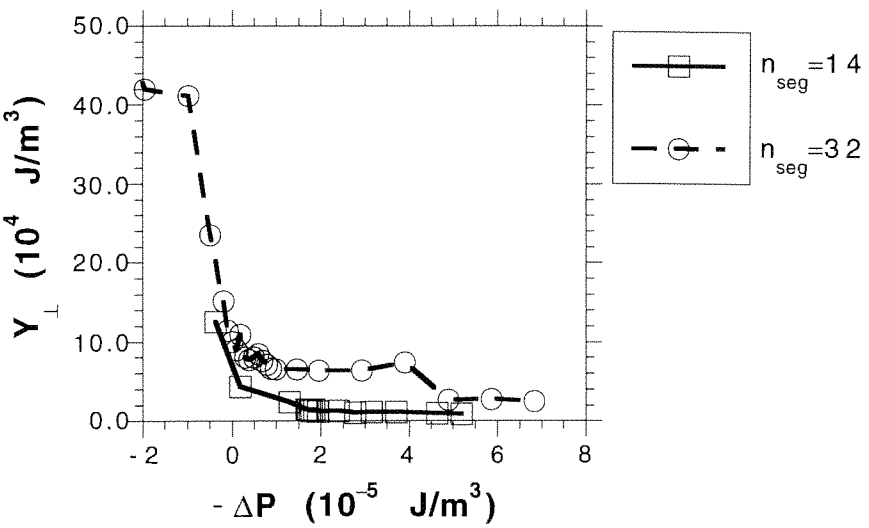

(b)

Fig. 3.22(a) K_V as a function of stress for n_{seg} = 14 (prestress incorporated) and n_{seg} = 32 (stress-free model). (b) $Y_\perp$ as a function of the stress for n_{seg} = 14 (prestress incorporated) and n_{seg} = 32 (stress-free model).

compressive, are again expected for a network under precompression. The effect of sterics in producing large K_A values during compression, is enhanced under the precompression.

Fig. 3.21b shows that the two models differ little in the behaviour of the shear modulus μ under both compression and tension. When the networks are placed under tension, the shear modulus of the stress-free and the prestress models both increase monotonically in magnitude. This is expected again, since the tether constraints offer resistance to the stretching of the chains during shearing under large tensions. Under compression, the shear modulus of both models increases only very weakly, as now, the tether constaints no longer play an important role.

The out-of-plane moduli, namely the volume compression modulus K_V and transverse Young's modulus $Y_\perp$, for the two models follow the same trends. Fig. 3.22(a) shows that the behaviour of the volume compressibility in the prestress model is again very similar to that found in the stress-free model. Fig. 3.22(b) shows that $Y_\perp$ for the two models share many of the same qualitative features, namely it increases under compression and decreases under tension (see Chapter 2 for a discussion on the magnitudes of $Y_\perp$).

Comparison with experiments

To build a full-scale model of the red cell cytoskeleton using the polymer chain model would be too computationally intensive and beyond our available computational resources. To meet this end, effective representations have been developed for the polymer chain model of the cytoskeleton (private communications, Boal and Discher, 1996). In such representations, each spectrin tetramer is replaced by

a single element (spring) subject to two- and three-body interactions. The resulting "effective" model is then used for simulating the micropipette aspiration experiments on red cells.

There is an inherent problem with using pure spring networks to represent the cytoskeleton under large scale compression and tension. Beyond some critical compressive stress, a pure spring network collapses (Discher *et al.*, 1997), while above a critical tension (where $K_A = 0$), the network expands without bounds. Neither of these cataclysmic events are seen in the physical or the model cytoskeleton. To circumvent this problem, three-body interactions must be added to the Hooke's law potential to provide lower and upper bounds to the single-plaquette area of the network.

Sec. 3.6 Summary

Chapter 3 has focused on the effects of stress on the reference network's geometrical and elastic properties. This study has been carried out by applying either isotropic or anisotropic tension/compression to the model network and analysing the network's response.

In terms of the geometry, the graph of the mean area per junction vertex $\langle A_j \rangle$ as a function of the applied stress $-P$ ($P < 0$ is tension while $P > 0$ represents compression) is "S"-like is appearance. That is, at large tensions, $\langle A_j \rangle$ asymptotes to a value given by $A_c/\langle A_j \rangle = 7$, where A_c is the contour area per junction vertex. This

asymptotic limit corresponds to the resistance to area expansion arising from the tether constraints built into the network chains. Under compression, $<A_j>$ also flattens out to some minimum value, reflecting the fact that the chains are in close proximity and steric interactions play an important role in preventing the network chains from crossing one another.

The response of the mean displacement of the network from the computational bilayer $<t>$ is correlated to the behaviour of $<A_j>$. When $<A_j>$ approaches its maximum value, $<t>$ tends towards some minimum value; and, when $<A_j>$ reaches some minimum value, $<t>$ tends towards a maximum. However, for a fixed small stress, the values of A_j and t are not particularly correlated within a given configuration. That is, the product $(A_j \bullet t)$ is not well conserved among configurations.

The area compressibility K_A increases monotonically under tension, increases under compression and has a minimum near zero stress. The shear modulus μ behaves in a similar way under tension, but rises only weakly upon compression. The ratio K_A/μ is observed to decrease monotonically with increasing tension to the value of unity (about which the ratio oscillates for a small range of the tension) and then increases again. This implies that the network has a negative Poisson ratio for some small range of the tension.

The volume compression modulus K_V behaves similarly to K_A: rising under tension, with a minimum at around zero stress, and

increasing under compression. Contrary to this, the transverse Young's modulus is observed to decrease monotonically with increasing tension to some constant value.

Treating the response of the network under stress via a simple mean field spring model, an effective spring constant k_{eff} of the network is extracted and found to be equal to 2 x 10^{-5} J/m^2 or, equivalently, $\beta k_{eff} s_o^2 = 32$, where s_o is the mean interjunction spacing of the network attachment nodes. This implies that the network junctions execute only small oscillations around their mean position, or, equivalently, the junctions are "cold".

The consequences of a prestress (or precompression) present in the rest-state of the network have been explored. The geometrical and elastic properties of the cytoskeleton are qualitatively very similar in both the precompression model and the stress-free model. One of the main differences found is that the effective spring constant in the prestress model $(k_{eff})^{ps}$ has decreased to 1.5 x 10^{-5} J/m^2 when compared to that of the $n_{seg} = 32$ network at zero stress.

The reference network has also been observed to behave anisotropically under large uniaxial tensions and is isotropic only under small tensions. This observed anisotropy is expected because of the hexagonal geometry of the network and corresponds to similar anisotropies observed for triangulated networks of springs in two dimensions.

Chapter 4
BARRIER-FREE PATH SIMULATIONS

4.1 Introduction

Although lateral diffusion of proteins in the plasma membrane is an important transport mechanism, specific confinement or restricted motion of specific membrane proteins also plays a role in the survival of the cell. Examples of membrane proteins whose motion in the lipid bilayer is restricted include: (1) In the purple membrane of *Halobacterium halobium*, the protein bacteriorhodopsin self-assembles into large aggregates (see Fig. 4.1). As one would

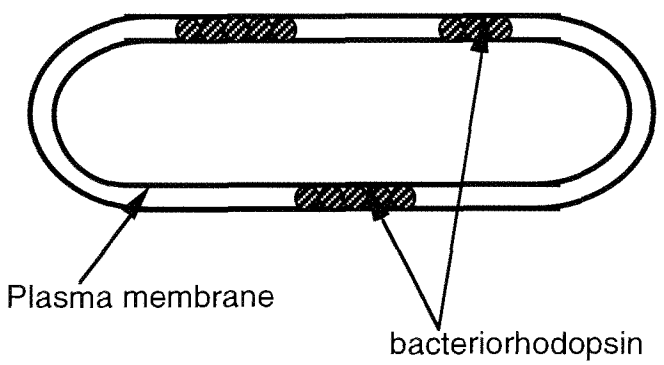

Fig. 4.1 Schematic drawing of the bacterium *Halobacterium halobium* showing the light activated proteins (a proton pump), namely bacteriorhodopsin, self-assembling into large aggregates which diffuse very slowly within the plasma membrane. (Adapted from Alberts, Bray, Lewis, Raff, Roberts and Watson, "Molecular Biology of the Cell", 1989, page 298)

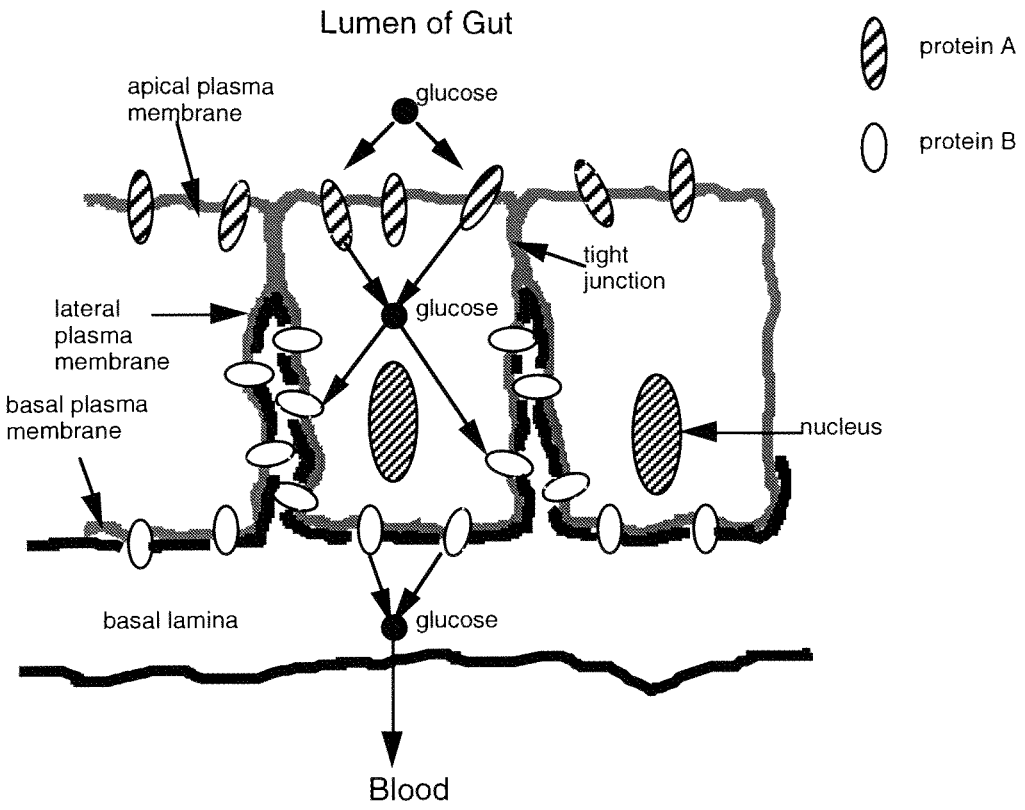

Fig. 4.2 Schematic diagram of an epithelial cell showing how a plasma membrane protein is restricted to a particular domain of the membrane. Tight junctions are thought to confine the transport proteins to their appropriate membrane domains by acting as diffusion barriers within the plasma membrane. This segregation permits nutrient transfer across the epithelial sheet from the gut lumen to the blood. As shown above, glucose is actively transported into the cell by glucose pumps (proteins A) at the apical surface and diffuses out of the cell by facilitated diffusion mediated by passive glucose carrier proteins (proteins B) in the basal plasma membrane. (Adapted from Alberts, Bray, Lewis, Raff, Roberts and Watson, "Molecular Biology of the Cell", 1989, page 298)

expect, these large aggregates diffuse very slowly. (2) In epithelial cells (lining the gut or tubules of the kidney), certain enzymes and transport proteins are confined to the apical surface of the cells, whereas others are confined to the basal and lateral surfaces. This segregation of different types of proteins is thought to be

maintained, at least in part, by the barriers set up by a specific type of intercellular junction called a tight junction (see Fig. 4.2). (3) In the red blood cell, the lateral motion of the immobile fraction of the protein band 3 is restricted by its attachment to the membrane cytoskeleton (see Fig. 4.3). This is an example of a protein whose motion is constrained by attachment to a macromolecular assembly located inside the cell.

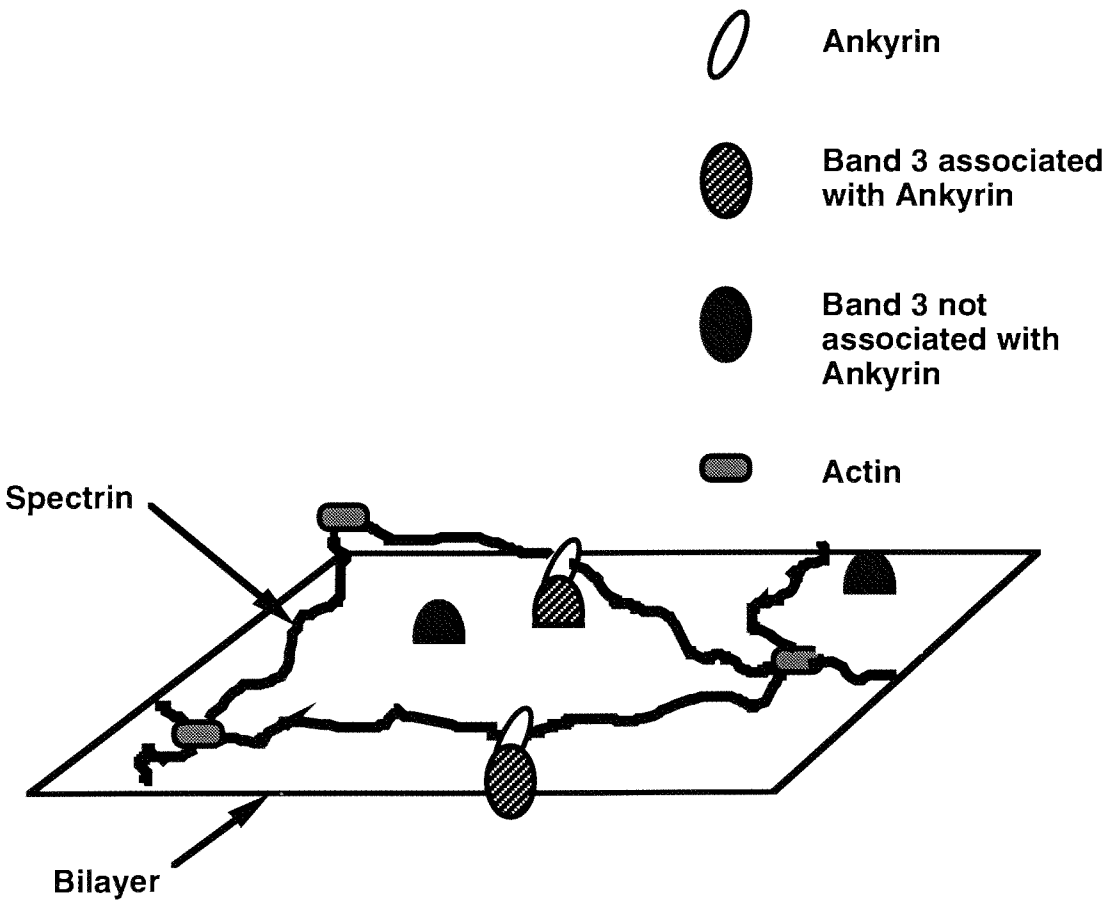

Fig. 4.3 Schematic diagram showing the association of band 3 with ankyrin, anchoring the cytoskeleton to the bilayer. These band 3 proteins are constrained in their lateral motion, while other band 3 proteins would be free to diffuse both laterally and rotationally.

Numerous FRAP and SPT experiments have been used to probe the diffusive behaviour of membrane lipids and membrane proteins (such as rhodopsin). In addition to allowing extraction of diffusion constants for proteins and lipids in the membrane, these experiments also show evidence of restricted motion of proteins in plasma membranes due to steric interaction with the associated cytoskeleton (Koppel *et al.*, 1981; Tsuji and Ohnishi, 1986; Edidin *et al.*, 1991; Kusumi and Yamamoto, 1993). SPT experiments, in particular, provide a method of probing the geometry of the network by measuring how far a protein can be dragged (by means of an optical tweezer) before the protein encounters a "barrier" in the network which causes it to be ejected from the optical trap. This distance travelled by the protein can be used to construct a barrier-free path length (BFP), which is observed to span a wide range of values depending on protein and cell type (see Chapter 1).

There are various ways in which the lateral diffusion of membrane proteins may be hindered. It has been proposed (O'Shea, 1984) that the concentration of integral membrane proteins plays a major part in contributing to the low rates of protein lateral movement. However, a computer simulation study (Pink, 1985) has shown that increasing the protein concentration (fractional area of the bilayer that is covered by proteins) from 0% to 50% leads to a decrease in the lateral diffusion coefficient of less than a factor of 5. This observation supports the opinion (Kell, 1984) that the concentration of proteins alone cannot account for the low lateral diffusion rates of membrane proteins.

FRAP experiments (Sheetz *et al.*, 1980) have shown that in the mouse spherocytic erythrocyte, which lacks the major components of a normal erythrocyte membrane matrix (composed of spectrin, actin, bands 4.1 and 4.9), membrane proteins diffuse about 50 times faster than in normal mouse erythrocytes. Thus, the low lateral mobility of the membrane proteins in normal erythrocytes may arise from the presence of the associated membrane cytoskeleton, interacting with the membrane proteins. Fowler and Bennett (1979), using a procedure designed to weaken the association of spectrin with the membrane, observed a twofold increase in the lateral mobility of band 3 compared to normal cells, which further supports the idea that interactions of membrane proteins with the cytoskeleton do play an important role in controlling the lateral mobility of proteins.

Several different models have recently been proposed to explain how the cytoskeleton might affect the diffusive behavior of membrane proteins. Zhang *et al.* (1993) proposed a "transient interaction model" (shown schematically in Fig. 4.4) to explain the reduction in the lateral mobility of proteins for which ectodomain interactions dominate the cytoplasmic interactions. In this model, there is a class of proteins, termed "post" proteins, which are tethered to and/or entrapped by the membrane cytoskeleton, much like the protein band 3 in the RBC. The ectodomains of diffusing proteins are thought to interact with the post proteins by transiently sticking to the (relatively) immobile posts.

Tsuji and Ohnishi (1986) studied the relation between band 3

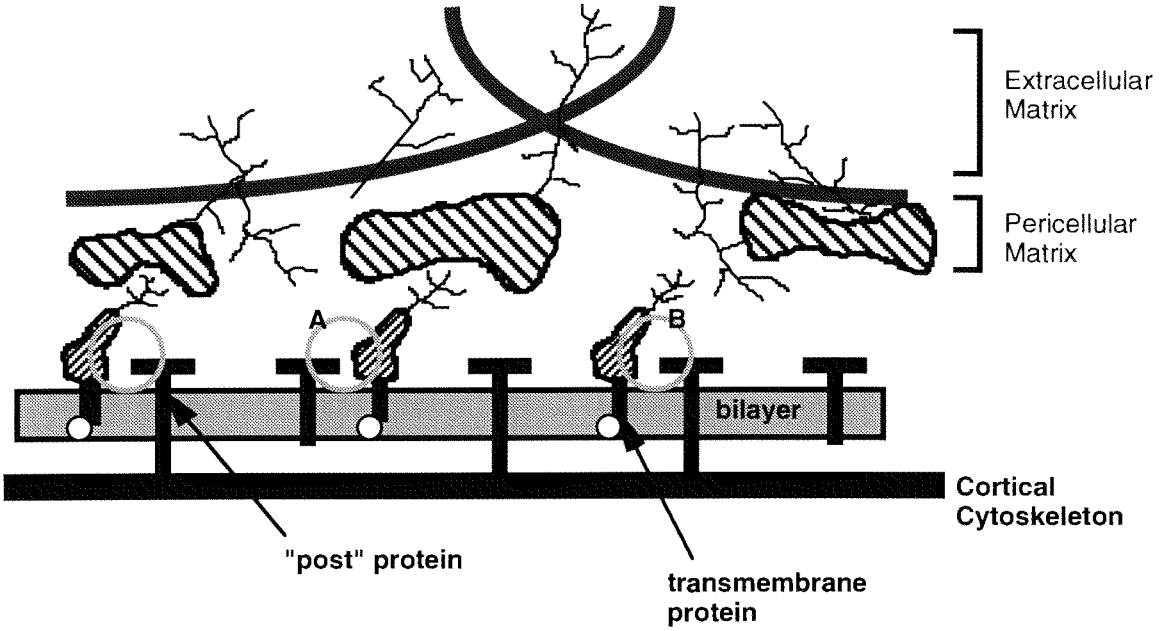

Fig. 4.4 Schematic diagram of the transient interaction model. Immediately inside the plasma membrane is the cytoskeleton while on the extracellular side of the bilayer, macromolecules in the pericellular region interact with the ectodomains of the membrane proteins. Post proteins are attached to or entrapped by the cytoskeleton. Certain proteins bind briefly to the post proteins through their ectodomains (circles A and B). (Zhang *et al.*, 1993)

lateral motion and the state of polymerization of spectrin. Using the FRAP technique, they found that the movement of the mobile fraction of band 3 (i.e. the fraction of band 3 not bound to ankyrin) was restricted by the cytoskeletal network. The restriction was found to be strongly dependent on the spectrin association state (that is, on whether the spectrin molecules are in dissociated dimers or associated tetramers). The above experimental results can be understood through a so-called membrane cytoskeleton "fence" model that incorporates the mechanisms for restriction of band 3

translational diffusion by the cytoskeletal network (Tsuji *et al.*, 1988; Kusumi *et al.*, 1993).

In the fence model, ankyrin-bound band 3 proteins have no translational mobility, while unbound band 3 proteins are able to diffuse throughout the cytoskeletal meshwork. The diffusion beyond a mesh can only take place if an opening occurs in the cytoskeletal "fence", an event which can occur in several ways: (1) The spectrin tetramer dissociates into dimers, (2) The distance between the membrane and the cytoskeleton fluctuates, opening a "gate" for the protein, and (3) the membrane skeleton dissociates from the membrane. Experiments (Sako and Kusumi, 1994) that investigate the movements of the E-cadherin (a cell-cell recognition-adhesion receptor) in the plasma membrane of a cultured mouse keratinocyte cell suggest that the plasma membrane is indeed compartmentalized into many domains (300–600 nm in diameter). This observed compartmentalization of the plasma membrane into localised domains is consistent with the predictions of the membrane-skeleton fence model.

The "discrete-barrier model" of Saxton (1990) assumes that the membrane skeleton forms an incomplete triangular lattice, in which the bonds corresponding to normal tetramers act as barriers to diffusion and the nodes correspond to actin proteins. Missing bonds correspond to defective tetramers, including missing tetramers, isolated dimers, and dimer pairs unable to associate. Changing the fraction of bonds present in the model alters the diffusive behaviour

of a protein in the lattice. As the fraction of bonds decreases, the length of diffusion paths increases, and at the percolation threshold long-range paths first appear.

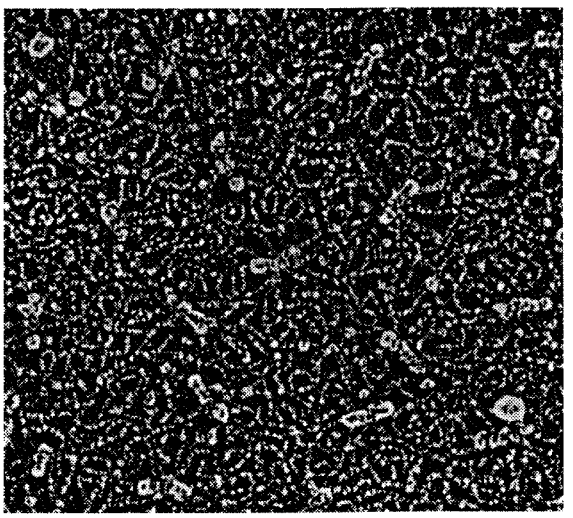

Fig. 4.5 An unexpanded human red cell skeleton imaged by transmission electron microscopy (Heuser, 1983). The spectrin tetramers are in close proximity to each other and are highly convoluted, producing a densely packed skeleton network.

Another model (Saxton, 1990) that has been proposed is the "continuous-barrier model", which assumes that the membrane protein moves through a region containing a continuous distribution of barriers. That is to say, the protein is obstructed at every point in the path. In an unexpanded RBC cytoskeleton, spectrin is observed to be highly convoluted and spectrin tetramers appear to be in close proximity to each other (see Fig. 4.5). Saxton (1990) proposed that the dense-packing of spectrin would signficantly block long-range diffusion, although short-range diffusion would still be possible (see

also Saxton, 1982/1989b).

In our study of the directed motion of proteins in the erythrocyte plasma membrane, we concentrate on the constraining effects of the cytoskeleton rather than on the steric effects of unconstrained in-plane obstacles (for example, glycoproteins and mobile fractions of the protein band 3) present in the bilayer. The rationale behind this choice is as follows: (a) Experimental observations show that diffusion coefficients in spectrin-deficient erythrocytes are as much as fifty times larger than those in normal erythrocytes (Sheetz *et al.*, 1980). (b) Simulations show that increasing the concentration of membrane proteins in the bilayer from 0%-50% only leads to a factor-of-five decrease in the diffusion coefficient of proteins (Pink, 1985). Our model also focuses on extracting BFP's, instead of diffusion coefficients, largely because BFP's are unaffected by many dynamical attributes of the cytoskeleton (for example, hydrodynamical effects) and are, thus, easier to investigate than diffusion coefficients. The system chosen for our simulations is the human erythrocyte. This choice is motivated by the availability of experimental studies on RBC elastic and geometrical characteristics, which can be used to test the simulation results (see Chapters 2 and 3).

Sec. 4.2 of this chapter presents a simulation algorithm which, in conjunction with the reference model of the erythrocyte plasma membrane discussed in Chapter 2, allows the efficient simulation of the optical tweezer experiments (Kusumi *et al.*, 1993). In Sec. 4.3, we

study how the mean free path lengths of directed protein motion vary with the dragging force and the size of the protein probe. The method of extracting a BFP length also is summarized. Sec. 4.4 describes how large protein probes can be used to give a measure of the size of a cytoskeletal "corral" (a region within which the protein is confined). In contrast to this, Sec. 4.5 studies how small protein probes can be used to extract an effective diameter for the attachment points of the network. The chapter then concludes with a summary of the results in Sec. 4.6.

4.2 The simulation technique

To simulate fully the protein-drag experiments, dynamical aspects such as hydrodynamic flow of the cytoplasm around the spectrin chains would be required. This kind of simulation is very complex to carry out and is beyond the scope of this research. We propose, instead, that experimental measurements of BFP's in the limit of small optical trapping forces are approximately equivalent to the simulation results obtained from a static cytoskeletal network at infinitesimally small forces. We need to select a representative cytoskeletal network from our simulations. We achieve this by propagating a model network and selecting a configuration whose value of A_j is within 1% of $<A_j>$, where A_j is the area per junction vertex. Rather than generating many realizations (a realization is a sample network configuration), we find it computationally more efficient to work with a single, large realization. We do not need to simulate an infinitely large system, given that the BFP's extracted

from recent SPT experiments (Kusumi *et al.*, 1993) are in the hundreds-of-nanometers range. Thus, we select a single equilibrated realization of the cytoskeleton network, which is larger than the average barrier-free path and which properly represents the geometrical properties of the network.

To simulate the protein drag experiments, a computational protein is introduced into the network realization (prepared as described above) at a randomly chosen location. The shape of the computational protein is a sphere whose center is on the xy plane representing the bilayer. The interaction V_{pq} between the protein p and an element of the cytoskeleton q is taken to be similar in form to Eq. (2.3),

$$\begin{aligned} V_{pq}(r) &= 4\mathcal{E}\,\{(S/r)^{12}-(S/r)^{6}+1/4\} && 0 < r < 2^{1/6}S \\ &= 0 && r > 2^{1/6}S, \end{aligned} \tag{4.1}$$

where S is a variable reflecting the length scale of the protein-spectrin interaction. (An effective protein radius R_E will be defined in Eq. (4.6)).

The protein is moved through the network along a straight line in a randomly chosen direction. The positions of the network elements are held fixed throughout the protein motion. The protein position is advanced in successive steps of size 0.001σ (where σ is defined in Eq. (2.3)). At each step, the force on the protein arising

from the cytoskeleton is evaluated through Eq. (4.1). Once this force from the cytoskeleton exceeds a predetermined threshold value F_o, the protein is deemed to have escaped from the trap, and the displacement d from the start of the trajectory is stored. A total of 10^5 trajectories is generated for each parameter set, S and F_o.

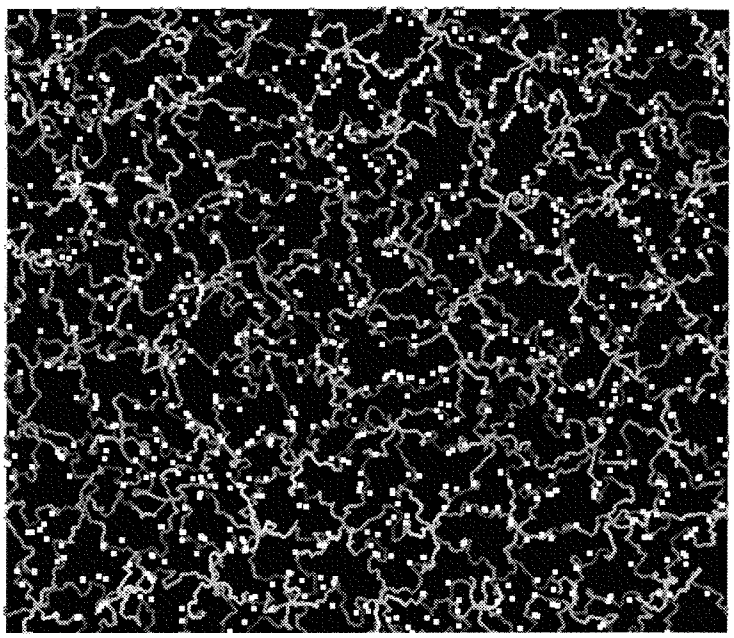

Fig. 4.6 Picture shows a view of a network realization (n_{seg} = 32) from the +z direction. The white spots indicate the respective stopping points of the computational protein, which are mostly located near the attachment points of the network to the bilayer. (A total of 10^3 trial runs is shown).

Fig. 4.6 shows a view of the network from the $+z$ direction (cytoplasmic side of the bilayer). The shaded lines indicate the position of the cytoskeleton, with elements nearer the viewer indicated by lighter shading. The stopping points of proteins with S/σ = 0.89 are shown as white disks, of diameter 0.89σ. One can see

that a large number of stopping points occur at the chain midpoints, where the chains are attached to the computational bilayer. Note that large proteins are stopped by the spectrin chains in our cytoskeleton model.

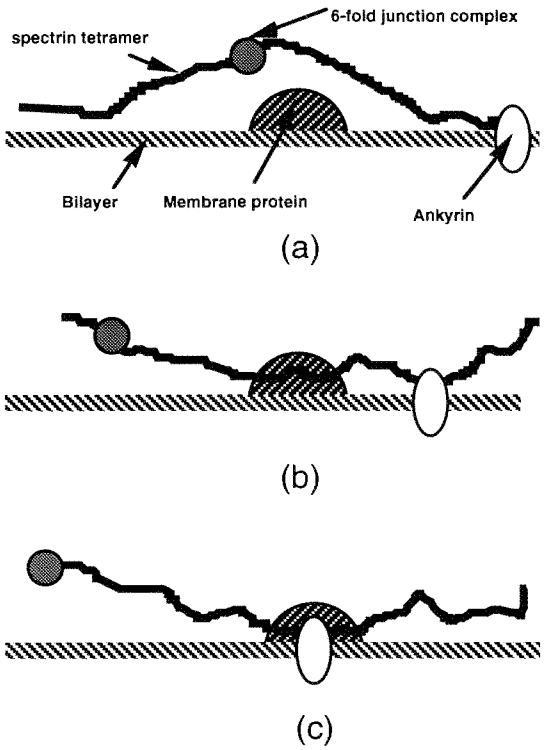

Fig. 4.7 Schematic diagram showing the different situations that might occur during a simulation run. (a) Protein slips through a gap in the network. (b) Protein is obstructed by a spectrin filament. (c) Protein is obstructed by an attachment site (ankyrin plus band 3).

The different possible situations that might arise during a simulation run (see Fig. 4.7) include: (a) A protein slips through the spectrin network, in particular the gap under the sixfold junction. The cytoplasmic domain of the protein band 3 in the erythrocyte extends perhaps 25 nm from the bilayer (Low, 1986) as indicated by

the radius of the hemisphere in Fig. 4.4 (the attachment site is not necessarily at the terminus of band 3). The average displacement of a sixfold junction from the bilayer is approximately 32 nm (see Chapter 2 for mean height of network) and the mean distance between attachment points is about 70 nm, which would make the gap wide enough for the hemispherical protein to slip through. (b) A protein encounters a spectrin tetramer, which in the picture is at a displacement above the bilayer at roughly half the radius of the hemisphere. This is possible because fluctuations in the conformations of the spectrin chains make it possible for a tetramer to come close to the bilayer. (c) A protein encounters an ankyrin attachment site, and the protein motion is blocked, much like a ball hitting a pin in a pin-ball machine.

4.3 Extraction of barrier-free path lengths

Distributions of the protein path lengths are constructed from large samples in which the initial position and direction of motion of the computational protein is randomly chosen. A distribution $P(d)$ of the displacements d for 10^5 trajectories at fixed S and F_0 is shown in Fig. 4.8. The distribution peaks at $d/\sigma = 0$ and decreases monotonically to zero at large d/σ. The distribution has most of the events concentrated at $d/\sigma < 10$, which is approximately the distance between junction vertices.

Fig. 4.8 suggests that the distribution $P(d)$ is exponential-like over much of its range and Fig. 4.9 shows this behaviour clearly on a log-linear plot. For most of the values of S and F_0, the distribution

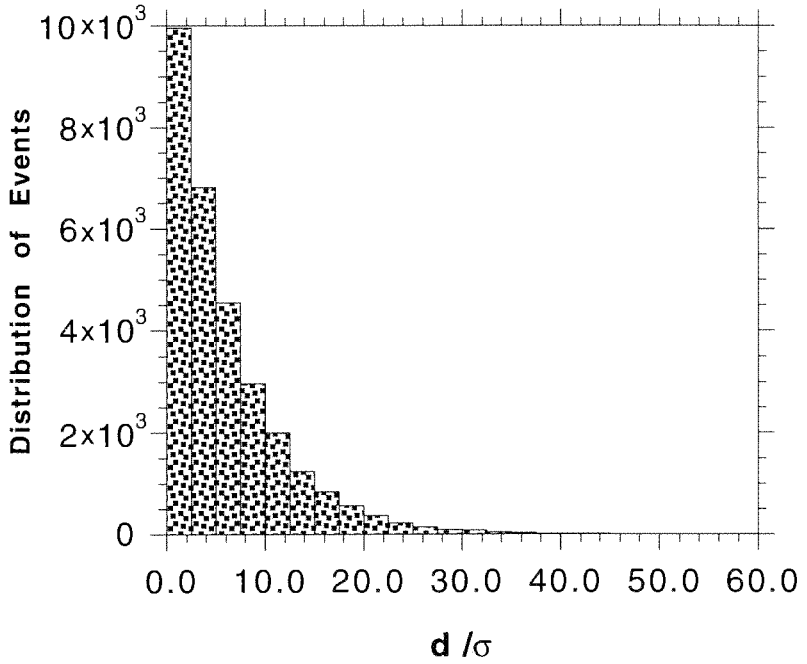

Fig. 4.8 Histogram of protein displacement d (in units of σ). A total of 100,000 data points contained in the plot are shown for $F_0\sigma/\varepsilon = 0.05$ and $S = 0.89\sigma$.

$P(d)$ can be fitted over the whole range of d with the exponential function,

$$P(d) \propto \exp(-d/\lambda). \tag{4.2}$$

From the distribution $P(d)$, we are then able to extract a mean path

length λ, which depends on the size of the threshold force F_0 and the protein size S. We find that λ obtained from the fit to the data using Eq. (4.2) is equal to $<d>$, as expected for an exponential distribution.

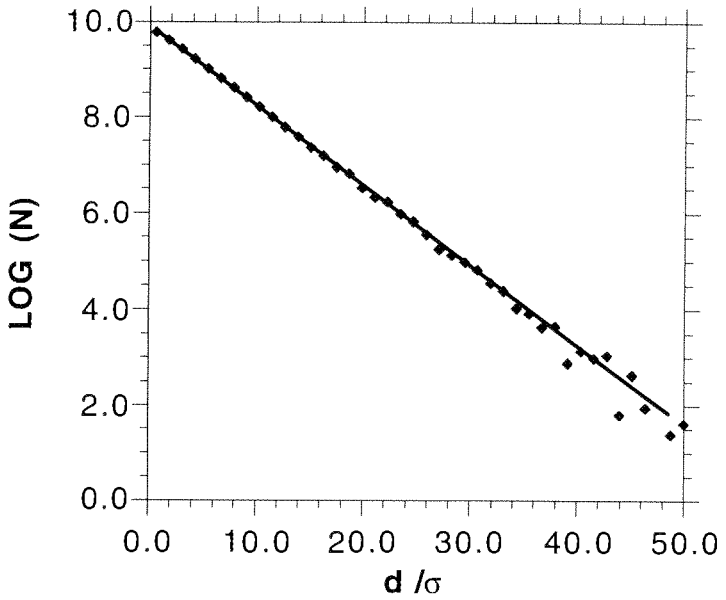

Fig. 4.9 Log-linear plot of distribution from Fig. 4.4. The linear behavior of the plot clearly indicates that the distribution is exponential in λ to a good approximation. Bold line is the best-fit line through the data points.

We might expect $P(d)$ to be exponential in analogy with classical scattering theory in two dimensions. Consider N_0 particles of radius R_1 incident on a medium with a density (number per unit area) ρ of randomly distributed scattering centers of radius R_2 (see Fig. 4.10). Then,

$$\begin{aligned} -dN(x)/N(x) &= (\rho l_w D\, dx)/l_w \\ &= \rho D\, dx \end{aligned} \qquad (4.3)$$

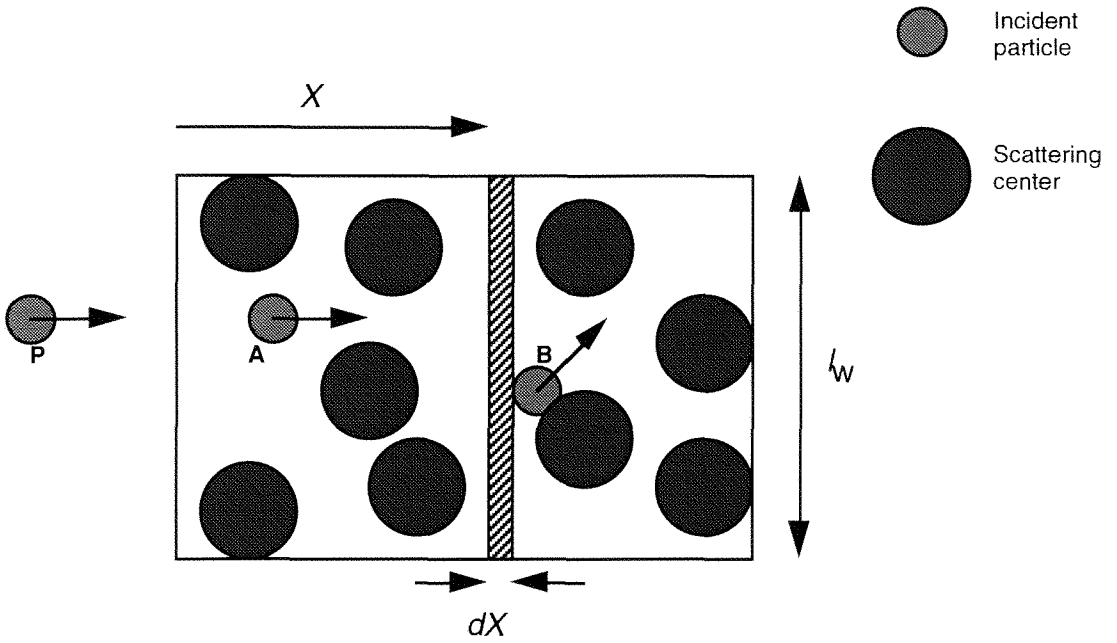

Fig. 4.10 Particle P (species 1) incident on medium containing a density ρ of scattering centers (species 2). Particle A is not scattered, while particle B is scattered and its direction of motion is changed. l_W is the width of the medium, and x is the distance travelled by a particle before it is scattered.

where $N(x)dx$ is the number of particles present in the region x and $x+dx$, $D = 2(R_1+R_2)$ and l_W is the width of the sample. Solving this differential equation gives

$$N(x) = N_0 \exp(-x/\lambda), \tag{4.4}$$

where $\lambda = 1/(\rho D)$. The motion of the particle between scattering collisions is much like the directed motion of the computational protein. The scattering of a particle off a scattering center in the medium is analogous to the protein being stopped by a steric barrier

in the network. Thus, the distribution of path lengths for the directed motion of the protein through the network is also expected to be exponential.

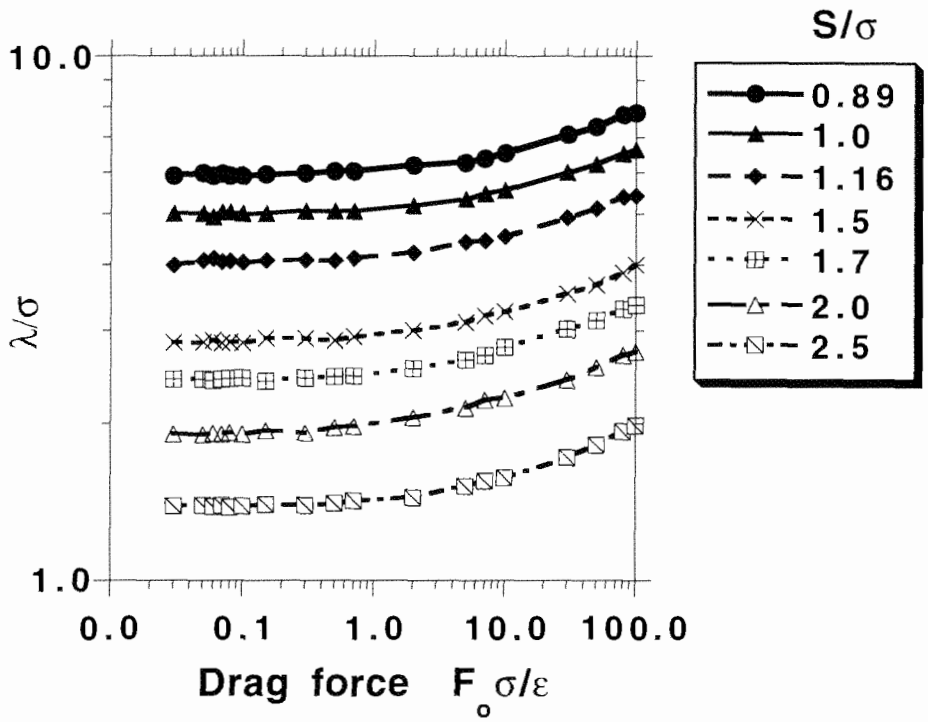

Fig. 4.11 Plot showing the variation of the mean path length of the dragged protein with the dragging force F_0. At small forces, there is little change in the mean path length, while at large forces, the mean path length increases monotonically.

Fig. 4.11 shows the relationship between the mean free path λ of the protein and the dragging force F_0 for various values of S (see Eq. (4.1)). The mean path λ can increase with F_0 because the repulsive potential in Eq. (4.1) does not have a "hardcore" limit. Thus, at large F_0, the protein is simply forced through the network. The mean path length increases monotonically with F_0 when $F_0\sigma/\varepsilon > 0.1$

for all values of S investigated. The weak dependence of λ on F_0 in the small force regime displayed in Fig. 4.11 is due to the fact that the protein is prohibited from moving the cytoskeleton out of its way in the simulations. We expect that λ is independent of F_0 for small F_0, since the guided protein is stopped as soon as it encounters the cytoskeleton.

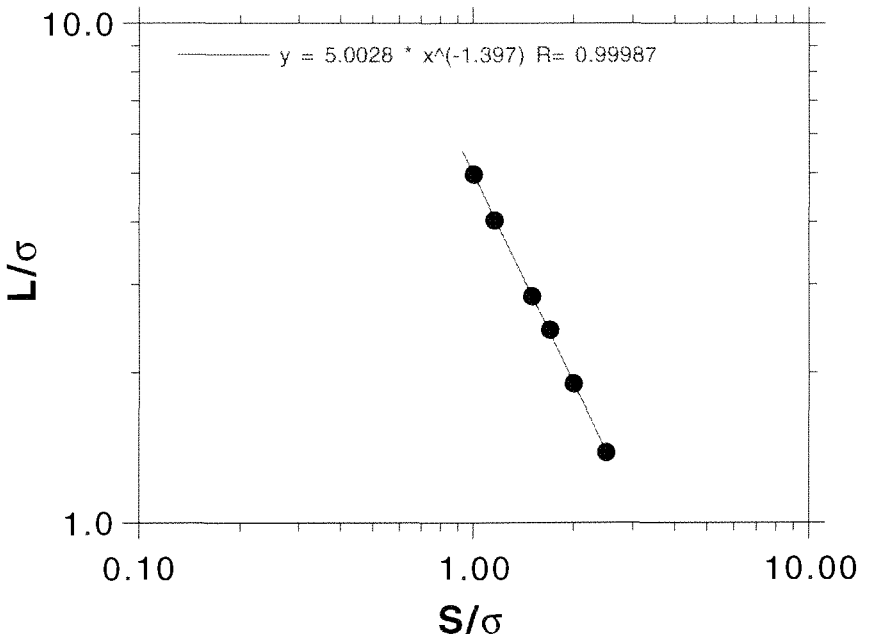

Fig. 4.12 Dependence of the barrier-free path length L on the protein size parameter S, showing that L decreases with increasing S. Note that the dependence seen here is only valid up the point where the protein size exceeds the space available for insertion in the network.

We define the barrier-free path (BFP hereafter) L as the asymptotic value of λ as $F_0\sigma/\varepsilon \rightarrow 0$. This extraction of L is carried out for several values of the protein interaction parameter S (see Fig. 4.12 above). We find that L decreases monotonically with increasing

S, reflecting the fact that proteins with larger S values encounter network steric barriers earlier than proteins with smaller S values moving along identical trajectories. We find that the variation of L with S can be fitted approximately with the following power law,

$$L/\sigma = 5.0(S/\sigma)^{-1.4}. \qquad (4.5)$$

Although Eq. (4.5) indicates that L vanishes as S approaches the geometrical length scale of an average spectrin chain (the average end-to-end distance of a spectrin tetramer in the cytoskeleton of about 12σ), in fact, the functional form of Eq. (4.5) does not apply at large S. The reason is that the cytoskeleton puts a bound on the largest protein that can be fitted into the network. That is, the protein is "corraled" at some finite value of S, and not mobile in the large S limit as implied in Eq. (4.5).

Since σ = 6.4 nm, we find that the BFP's displayed in Fig. 4.11 are approximately in the 10-50 nanometer range. At this time, there is no published data available for the barrier-free paths of directed protein motion in erythrocytes. However, our predicted BFP's for human erythrocytes are much smaller than the hundreds of nanometers observed in experiments on rat kidney fibroblastic cells (Sako and Kusumi, 1995). While most of this difference probably arises from the different cytoskeletal structures in erythrocytes and fibroblasts, there also could be differences in how experiments extract the BFP's in the zero force limit. This is a difficulty inherent

in such experiments since the proteins are sometimes "forced" through the cytoskeletal network by the optical tweezers.

4.4 Barrier-free paths of large proteins

Before discussing further the implications of the simulation results, we replace the protein interaction parameter S by a more geometrically transparent quantity. The repulsive interaction between the vertices of the cytoskeleton vanishes for $r > 2^{1/6}\sigma$ according to Eq. (2.1). This means that each vertex has a cutoff radius of $\sigma/2^{5/6}$ for the intervertex repulsive interaction. The cutoff distance for protein-spectrin interaction is $2^{1/6}S$. Thus, we define the effective guided protein radius R_E as the difference between the protein cut-off distance $2^{1/6}S$ and the spectrin-chain radius $\sigma/2^{5/6}$,

$$R_E/\sigma = 2^{1/6}(S/\sigma - 1/2). \tag{4.6}$$

In the simulation, large proteins ($R_E \geq 11$ nm) are found to be mostly confined in a local region of the network. Due to steric interactions, such proteins cannot pass out of the corral defined by the three nearest-neighbour chains which constitutes the basic triangular cell. In this way, the trajectories of large proteins are confined to lie within a single corral. Thus, L decreases with increasing R_E. The largest protein that can be inserted into the network is limited by the network geometry; that is, there is an

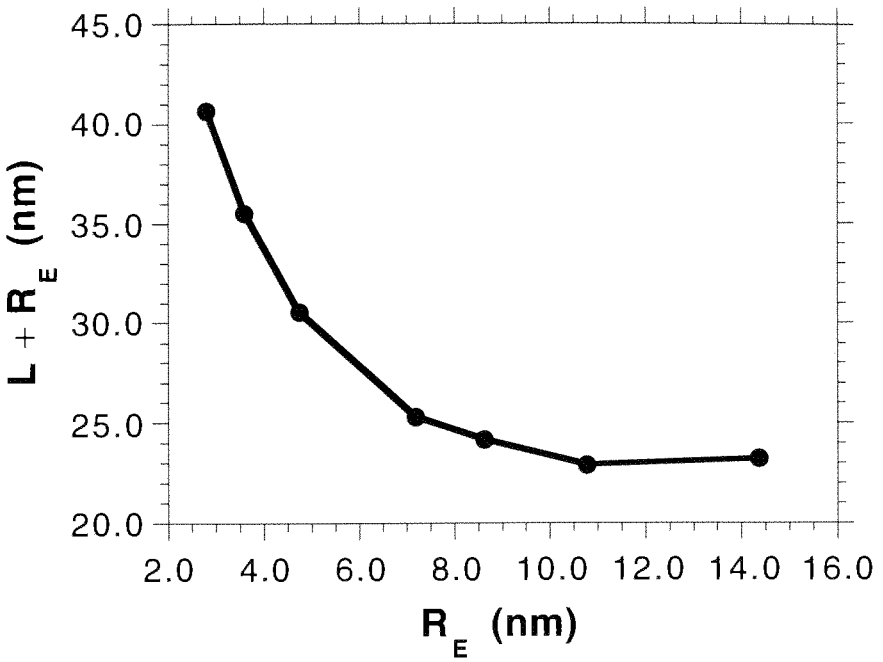

Fig. 4.13 $L+R_E$ shown as a function of the effective radius R_E. As R_E increases, $L+R_E$ decreases and reaches a minimum value of 23 nm at $R_E \approx 11\ \sigma$.

upper bound to R_E. The quantity $L+R_E$ should thus approach a constant value allowed by the corral geometry. Fig. 4.13 shows that $L+R_E$ actually reaches a minimum value of 23 nm (defined to be the mean size of a corral) and starts to increase very slightly for large proteins ($R_E > 2.5\ \sigma$). This effect can be understood as follows. As previously pointed out, large proteins have only very limited space where they can be inserted into the network and hence cannot be inserted into small corrals. Thus the BFP's of large proteins are not evaluated with the full configuration space available to small and medium sized proteins but are biased towards large corrals.

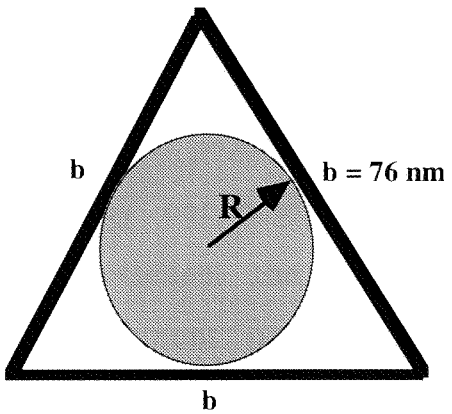

Fig. 4.14 Representation of a cytoskeletal corral by an equilateral triangle, whose sides, each of length b, reflect the average distance between the sixfold junctions of the RBC cytoskeleton network. The inscribed circle of radius R represents the largest protein that can be inserted into the triangle.

One immediate question that arises is whether this mean value of 23 nm obtained for the corral size is what one would expect from the geometry of the computational network. Suppose that we represent the average corral in the network by an equilateral triangle of side b = 76 nm, approximately equal to the average separation distance between sixfold junctions in the human erythrocyte (see Fig. 4.14). The maximum radius of an inscribed circle (representing the largest protein that can be fitted into the corral) in the triangle is thus 20 nm. This is close to the simulation value given above, showing that in the limit of large protein sizes, the effective corral radius of $L+R_E$ = 23 nm, is a reasonable reflection of the corral geometry.

4.5 Barrier-free paths of small proteins

As seen in Fig. 4.13, small proteins have much larger BFP's than larger proteins, because they encounter fewer obstacles associated with the cytoskeleton. In essence, the small proteins are affected mostly by the set of attachment points representing the ankyrin junctions. The remainder of the chain network, being further from the bilayer plane, hardly perturbs the motion of the small protein.

In this respect, the chain midpoints, to a reasonable approximation, act as a set of scattering centers or, rather, a field of barriers, to the guided protein, as it is dragged along the computational xy plane. This interpretation of the protein guided motion via two-dimensional scattering theory is consistent with the exponential distribution of path lengths in the simulation.

In view of this analogy described above, we can compare the motion of the protein to that of a point particle traversing a planar array of disks of diameter D randomly distributed with a well-defined area density ρ. In classical two-dimensional scattering theory, the absorption mean free path of the traversing particle is equal to $(\rho D)^{-1}$. With respect to the reference model, ρ is the area density of ankyrin attachment points and D is the effective diameter of ankyrin in the bilayer plane. The point to note is that, for non-zero R_E, D is affected by both the protein and ankyrin interactions. Thus, in order to make the connection to the scattering problem described

above, we determine the value of L in the $R_E \rightarrow 0$. limit This limiting value of L can be obtained graphically, as shown in Fig. 4.15. The behavior of (L^{-1}) is seen to be linear in R_E at small radii, and the zero radius limit of (L^{-1}) is 8.5 x 10^{-3} $(nm)^{-1}$ by extrapolation (or L = 118nm).

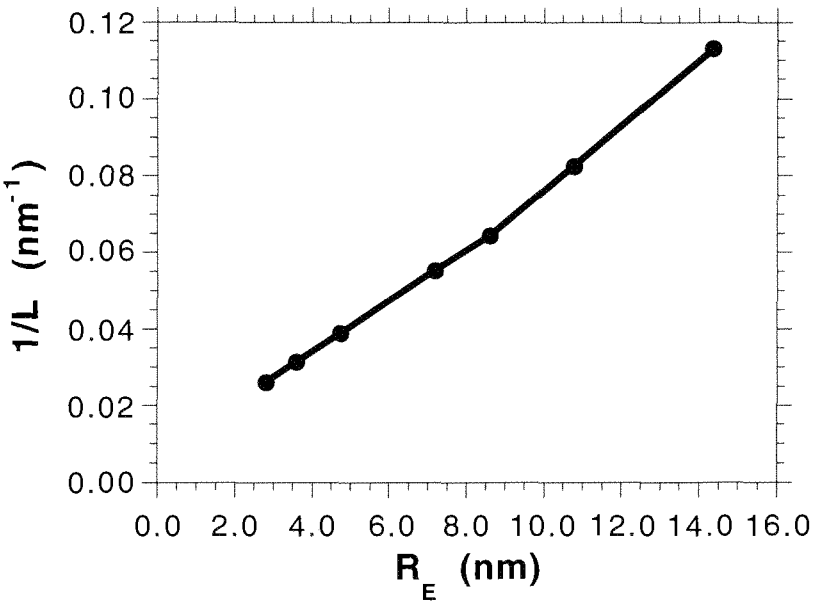

Fig. 4.15 Relationship between $1/L$ and R_E. To approach the limit of a zero-radius protein, we extrapolate L^{-1} as R_E approaches zero. In this limit of protein size, one can treat the protein drag problem much like a two-dimensional scattering problem.

The area density of ankyrin junctions in our simulation is $2(3)^{1/2}/b^2$, where b is the average distance between the sixfold junction vertices of the cytoskeleton. Taking b to be approximately 70 nm, then $\rho \approx$ 7.1 x 10^{-4} nm^{-2}. This gives D = 12 nm from the limiting value of L as R_E goes to zero, which is approximately twice

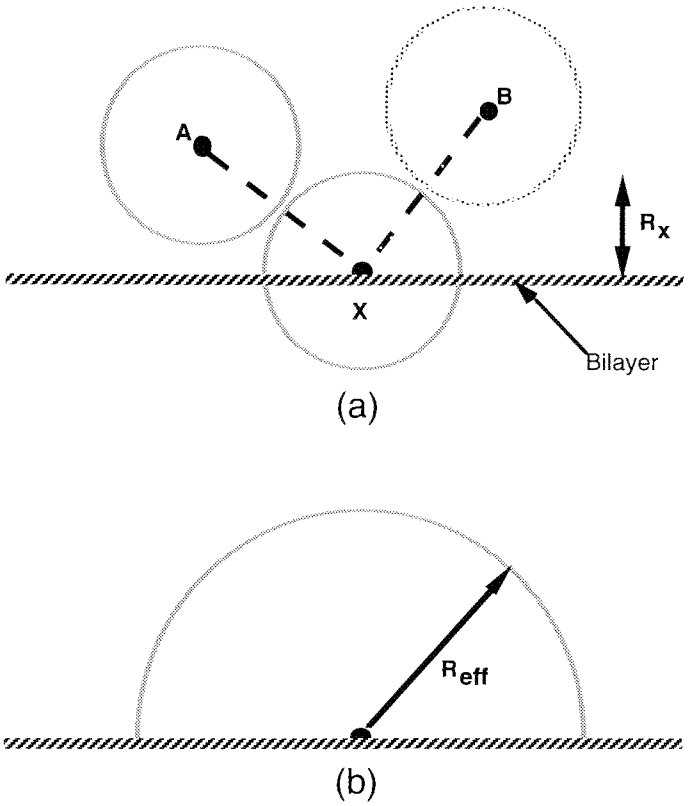

Fig. 4.16 (a) A segment of the spectrin chain. X represents the attachment point, A and B are the nearest neighbours. The circles represent the maximum extent of the repulsive interaction around each element along the chain. (b) Due to the close proximity of A and B to X, the effective steric barrier around X is increased ($R_{eff} > R_X$).

the diameter of the chains (equal to 7.2 nm). This seems counter-intuitive but the rationale behind this is as follows. Consider a particular attachment point of a chain in the reference model (see Fig. 4.16; attachment point is labeled X). The radius of the attachment point X is approximately 3.6 nm. Due to the close proximity of the two nearest neighbours, denoted by A and B in Fig. 4.16, the effective steric barrier around the attachment point X created by this close proximity of nearest neighbours is increased somewhat. Thus,

the effective mean radii of the attachment points as measured by the small protein probes is larger than the effective radius of a chain, consistent with the factor-of-two value for R_{eff}/R_x extracted in the simulation.

4.6 Summary

The simulation as described in this chapter is used to mimic the motion of proteins dragged by optical tweezers, as observed in recent SPT experiments. For most combinations of trapping force and protein sizes, the distribution of path lengths is found to be exponential. A mean path λ is extracted from the exponential distribution and is found to be relatively constant for small trapping forces. The barrier-free path L is obtained by extrapolating λ to zero trapping force F_0.

The obstacles to the directed motion of proteins in our simulations are found to be mainly the membrane/skeleton attachment sites. Thus, any temperature dependence of L (which is not investigated in our simulations) would have been weak because of the fixed concentration of the attachment sites in our cytoskeleton model. This is in contrast to the experimental results (Edidin *et. al.*, 1991) which showed that the barrier-free path of GPI-linked MHC class I proteins in murine HEPA-OVA cells is temperature-dependent.

The simulation also predicts that L decreases with increasing protein size as $L/\sigma = 5.0(S/\sigma)^{-1.4}$, where σ and S are length scales associated with the repulsive potentials within the network chains and between the protein and the chains, respectively. Large proteins are observed to be "corraled" in a region with an effective radius of 23 nm, consistent with the value of 20 nm expected from the geometry of the network.

The motion of small proteins through the network can be interpreted in terms of two-dimensional scattering. The BFP L then is equal to $(\rho D)^{-1}$, where ρ is the area density of scattering centers (ankyrin) and D is the average in-plane diameter of the junctions. In the simulation, D is found to be approximately 12 nm, which is roughly double the diameter of the polymer chain. In essence, the BFP's of small objects guided through the plasma membrane can be used to probe the in-plane sizes of some, but not all, cytoskeletal elements of the membrane.

Chapter 5
TESTS OF CYTOSKELETON/BILAYER ASSOCIATION MECHANISMS

5.1 Introduction

In Chapter 1, it was pointed out that the attachment of the RBC cytoskeleton to the bilayer of the plasma membrane is effected largely through the protein ankyrin, which binds both to spectrin and to the cytoplasmic domain of the transmembrane protein band 3 (see Fig. 5.1). Ankyrin has been determined to be a high-affinity

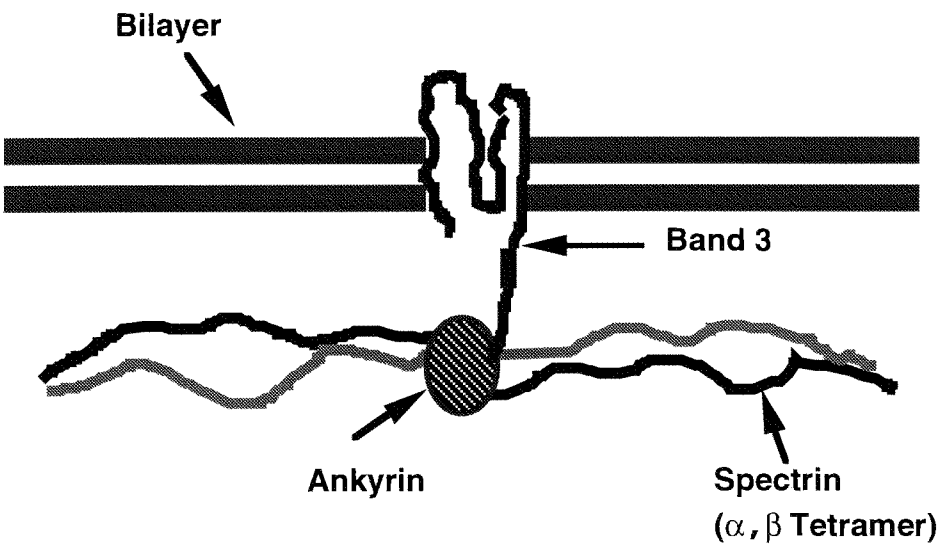

Fig. 5.1 Association of the cytoskeleton with the bilayer through the proteins band 3 and ankyrin.

membrane binding site for spectrin and band 3 (Bennett and Stenbuck, 1979a). Evidence that ankyrin provides a major membrane attachment site for spectrin in erythrocytes is based on several experiments. One such experiment (Bennett and Stenbuck, 1979b) showed that antibodies that selectively extract ankyrin prevent the binding of spectrin to membranes.

The cytoskeleton may also be attached to the bilayer through the protein band 4.1, which promotes the association of spectrin with actin (Fowler and Taylor, 1980; Ohanian *et al.*, 1985; Ungewickell *et al.* 1979), forming the sixfold junction complexes (see Fig. 5.2). Band 4.1 has been found to remain associated with membranes after

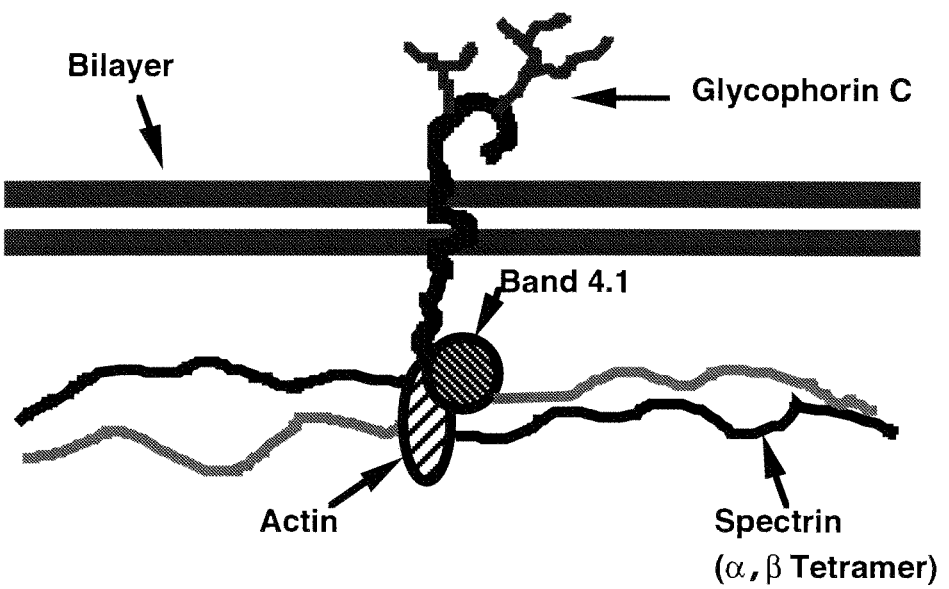

Fig. 5.2 Binding of the cytoskeleton to the bilayer effected through the protein band 4.1 and the glycoprotein glycophorin C.

removal of spectrin and actin (Bennett, 1980). This observation suggests that the protein 4.1 provides a membrane-linkage site for spectrin-actin complexes.

Several protein candidates for a membrane-binding site for protein band 4.1 have been proposed. These include the membrane protein glycophorin A (based on experiments on the binding of band 4.1 to glycophorin A liposomes (Anderson and Lovrien, 1984)) and also the membrane proteins glycoconnectin or glycophorin C (Mueller and Morrison, 1981). It has been found that the interaction between protein 4.1 and glycophorin A is not one of physiological importance, in that erythrocytes lacking glycophorin C exhibit a reduction in membrane mechanical stability, while glycophorin-A-deficient cells remain normal (Reid *et al.*, 1987).

From the experimental observations mentioned above, a question arises: does the cytoskeleton attach itself primarily through band 3, or are the attachments through the proteins band 3 and band 4.1 equally important? To address this question, then, we probe the relationship between the geometrical and elastic properties of the cytoskeletal network and the different bilayer binding sites that the network might have. In this chapter, three alternate mechanisms of cytoskeleton attachment are described within the context of the reference model developed in Chapter 2. The two mechanisms investigated in this chapter (in addition to the midpoint attachment of Chapter 2, referred to as case I) are: (1) Attachment of the sixfold junction complexes to the computational bilayer (case II). (2)

Attachment at both the midpoints and the sixfold junctions (case III). In both mechanisms, the binding sites are free to move in the bilayer.

In Sec. 5.2, we present the dependence of the geometrical properties (such as the equilibrium network area and the mean displacement of network from the bilayer) on the attachment sites. This is followed in Sec. 5.3 by a discussion of how the elastic properties (such as compression and shear moduli) are affected by alternate binding mechanisms. Sec. 5.4 demonstrates the attachment-dependence of barrier-free paths. Finally, the chapter concludes with a summary of the results in Sec. 5.5.

5.2 Effects of alternate attachment points on network geometry

The reference model developed in Chapter 2 has the midpoint of the network chains tacked to the computational xy plane. Here, we study two different cases. In the first case, only the sixfold junction complexes are tacked to the computational xy plane, leaving all other constituents of the network free to move about in the space above the xy plane. This is to simulate binding of the network skeleton to the bilayer only through the protein band 4.1. In the second case, the network is tacked at both the sixfold junctions (protein 4.1) and the midpoint of the network chains (protein ankyrin). Except for the network attachment points, the simulation is carried out in a similar

fashion as was described in Chapter 2: that is, a mixed MC/MD simulation of polymer chains.

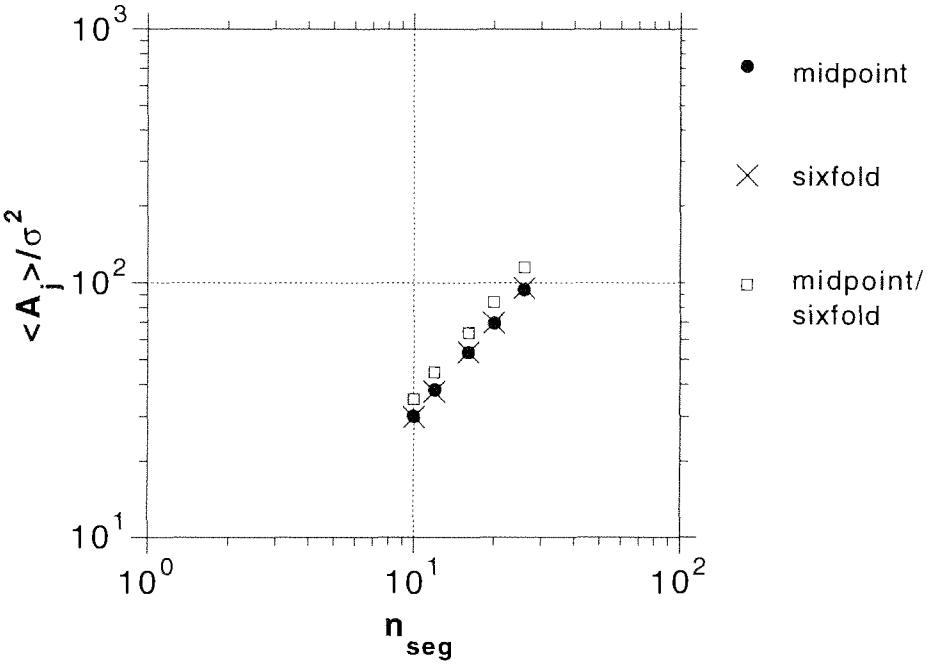

Fig. 5.3 The network area per junction vertex $<A_j>$ as a function of n_{seg} for three different ways of binding the network to the computational bilayer. As expected, simply changing the binding site from the chain midpoints to the sixfold junctions has virtually no effect on $<A_j>$. When the network is bound at both sites simultaneously, the network expands (for a given value of n_{seg}). This is in part due to the increase in steric interactions among the chains.

The observables measured are the average network area and displacement from the bilayer plus the in-plane and out-of-plane elastic moduli. First, we evaluate the effect of having alternate binding sites on the dependence of the network area per junction vertex $<A_j>$ on the number of segments per chain n_{seg}. Fig. 5.3 shows

this dependence, in comparison with the result obtained in Chapter 2. The power-law relations between $<A_j>$ and n_{seg} for the two new association geometries are as follows:

(a) Membrane skeleton tacked at the sixfold junctions (case II):

$$<A_j>/\sigma^2 \approx 2.0\, n_{seg}^{1.20}. \qquad (5.1)$$

(b) Membrane skeleton tacked at both the midpoints and sixfold junctions (case III):

$$<A_j>/\sigma^2 \approx 2.0\, n_{seg}^{1.24}. \qquad (5.2)$$

Comparison of Eqs. (2.6) and (5.1) shows that the scaling behavior of the network area is not altered by changing the binding site from the chain midpoints (case I) to the sixfold junctions. On the other hand, when the network associates with the bilayer at both the midpoints and sixfold junctions, the exponent of the power law increases slightly. This difference is also evident in Fig. 5.4, where the ratio of the contour area per junction vertex A_c to the average area per junction vertex $<A_j>$ is plotted as a function of n_{seg}. The power law dependence of $A_c/<A_j>$ on n_{seg} is as follows: (a) Sixfold junction tacking (case II)

$$A_c/<A_j> \approx 0.45\, n_{seg}^{0.78}. \qquad (5.3)$$

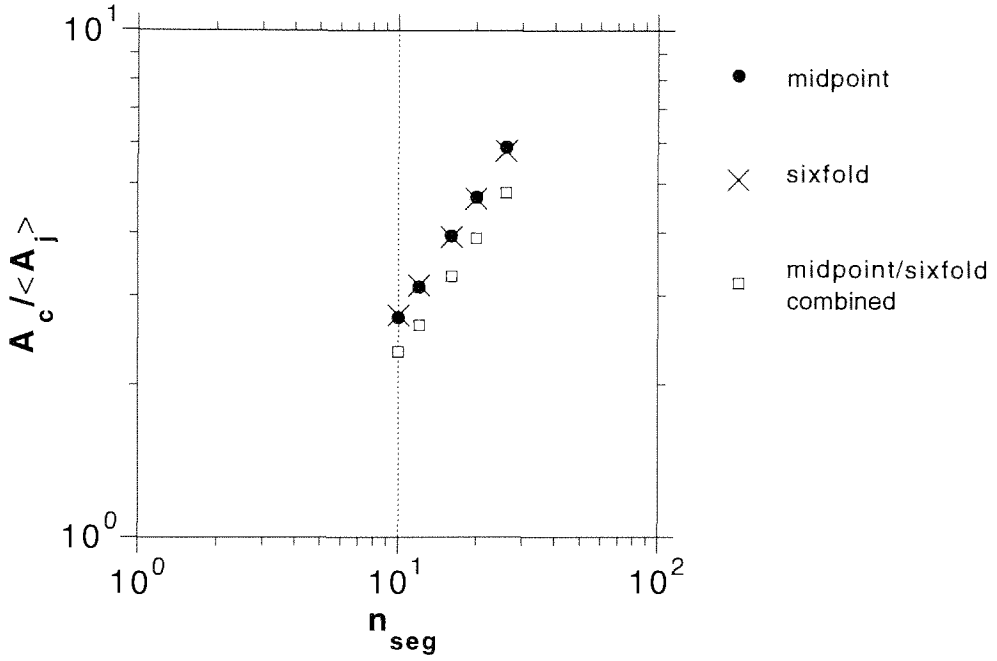

Fig. 5.4 Ratio of areas $A_c/<A_j>$ as a function of n_{seg}. Note that when the network is tacked either at the midpoint or at the sixfold junctions, the scaling behavior is very similar. In the case where the network is bound to the membrane at both the sixfold junctions and midpoints, $A_c/<A_j>$ increases more slowly as a function of n_{seg} and it is also lower than the other two cases.

(b) Tacking at both the midpoints and the sixfold junctions (case III):

$$A_c/<A_j> \approx 0.4\, n_{seg}^{0.76}. \qquad (5.4)$$

Eq. (5.3) shows that the number of segments n_{seg} required for the network to achieve $A_c/<A_j> \approx 7$ (as demanded experimentally) is 32, in the case of the attachment solely at the sixfold junctions. This is seen clearly in Fig. 5.4, where the data for cases I and II are very

similar. In case III, the required n_{seg} has jumped to the much larger number 42 (from Eq. 5.4). This increase of approximately 30% in n_{seg} indicates that the network chains of case III are generally stiffer than than those found in case I and II (when the comparison is made at fixed n_{seg}). To see why this is so, we compare the three cases under the condition that n_{seg} be the same. The greater number of membrane attachment sites in case III, in contrast to cases I and II, constitutes a larger number of constraints placed on the network. This leads to a reduction in the configuration space available to the chains in case III, which correspondingly forces the network to lie closer to the bilayer (see Figs. 5.5 and 5.6(a,b)). In order for the network in case III to be able to shrink from its contour area by a factor 7, the network must become "floppier" and, hence, n_{seg} must increase (see discussion in Chapter 2).

Since n_{seg} is the same for case I and II, the length scales σ for the two cases are equal and take the value 6.4 nm (see Chapter 2). On the other hand, in case III, n_{seg} equals 42 and, from the RBC spectrin contour length of approximately 200 nm, this gives $\sigma \approx 4.9$ nm.

The mean displacement $<t>$ of the network from the bilayer in all three cases reflects the behaviour of the average network area. Fig. 5.5 shows the variation of the mean displacement $<t>$ with n_{seg}. The $<t>$ data in cases I and II are again seen to be very similar, in contrast to the data for case III. The mean displacement $<t>$ for case III is seen to be markedly lower for the other two cases. This reflects

the fact that the number of membrane-binding sites is much larger in case III. The scaling behavior of $<t>$ for case II is given by

$$<t>/\sigma \approx 0.12\, n_{seg}^{0.9} \tag{5.5}$$

and for case III, by

$$<t>/\sigma \approx 0.06\, n_{seg}^{0.9}. \tag{5.6}$$

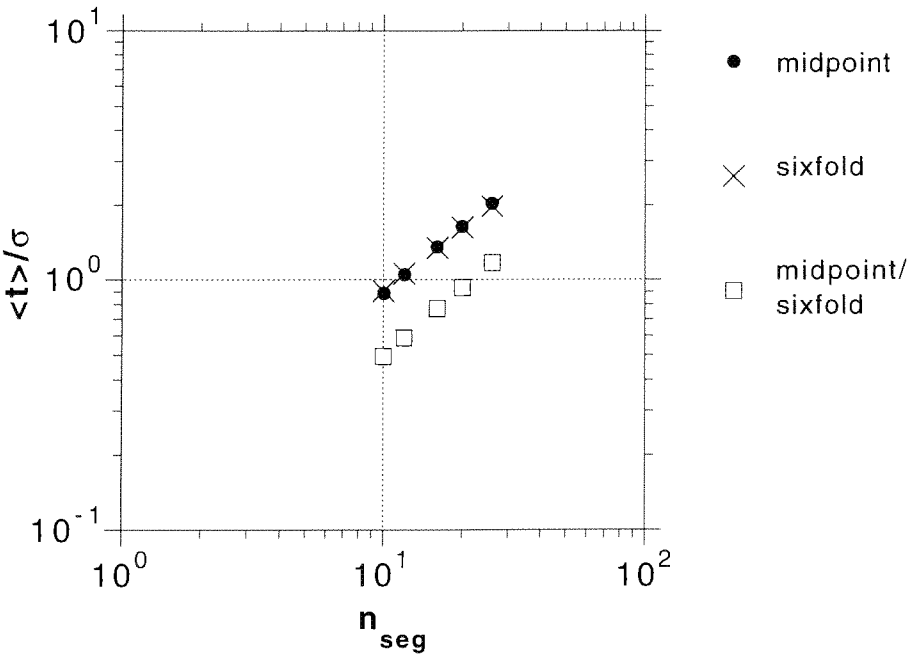

Fig. 5.5 The mean displacement $<t>$ as a function of n_{seg}. The behaviour seen in cases I and II is similar. The data in case III rise at about the same rate as the other two cases but are lower in value. From this, we see that the network in case III is markedly "flatter" than in case I and II.

Using the values of σ and n_{seg} calculated for cases II and III respectively, together with Eqs. (5.5) and (5.6), we find the mean displacement $<t>$ for case II to be $\approx$ 17 nm, the same as in case I, while for case III $<t>$ is predicted to be approximately 8.5 nm.

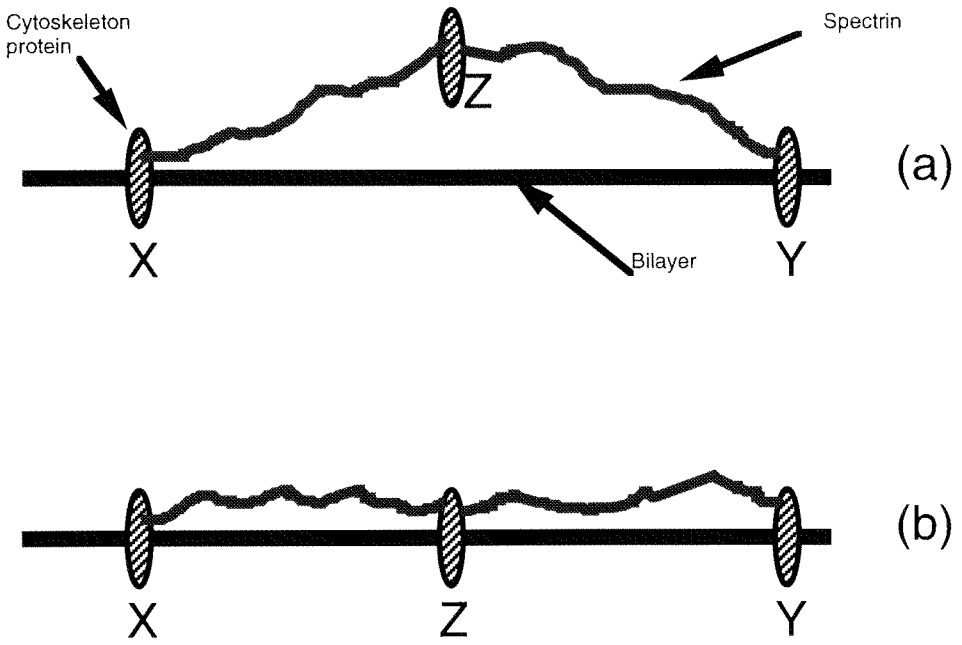

Fig. 5.6 (a) and (b) illustrate network attachment for cases I and III respectively. Notice that the network height in (b) is lower than in (a).

Fig. 5.6 above shows schematically what happens when the network is forced to be tacked down at additional locations along the chain. In Fig. 5.6(a), network chains are tacked down at proteins X and Y. Thus, effectively, the two chains XZ and ZY form a single long chain "XY", of some average length, say l_a. On the other hand, in Fig. 5.6(b), we have two distinct chains, each of length l_b, where $l_a > l_b$.

Clearly, the mean height of the chains in (b) is going to be smaller than in (a). Notice also that the chains XZ and ZY in Fig. 5.6(a), in comparison to those in Fig. 5.6(b), have more freedom to move horizontally and vertically, which undoubtedly affects the elastic behaviour of the chains (a point which will be taken up in Sec. 5.3).

5.3 Effects of attachment on network elasticity

We noted in Chapter 1 that the cytoskeletal network has been experimentally observed to bear a significant part of the extensional elasticity of the RBC. In Chapter 2, our investigation into the geometrical and elastic properties of the RBC cytoskeleton was based on the reference network being attached to the bilayer through the midpoint of the chains via ankyrin. As mentioned in Sec. 5.1, it has been confirmed that ankyrin is the primary binding protein tying the network to the bilayer; but, binding through other proteins (band 4.1) is also possible. If it is true that the network does attach itself to the bilayer through band 4.1, then the immediate question that arises is what effect this would have on the elastic properties of the network.

Considering the three cases, I, II and III, as described in Sec. 5.1, we first look at the in-plane elastic moduli, K_A (area compressibility) and μ (shear modulus). Fig. 5.7 shows the dependence of the in-plane moduli on n_{seg}. In case II, we find that

K_A and μ are described approximately as

$$\beta K_A^{II}\sigma^2 \approx 144\, n_{seg}^{-2.0} \tag{5.7}$$

$$\beta \mu^{II}\sigma^2 \approx 24\, n_{seg}^{-1.7} \tag{5.8}$$

and, in case III, we have approximately

$$\beta K_A^{III}\sigma^2 \approx 156\, n_{seg}^{-1.9} \tag{5.9}$$

$$\beta \mu^{III}\sigma^2 \approx 37\, n_{seg}^{-1.7}. \tag{5.10}$$

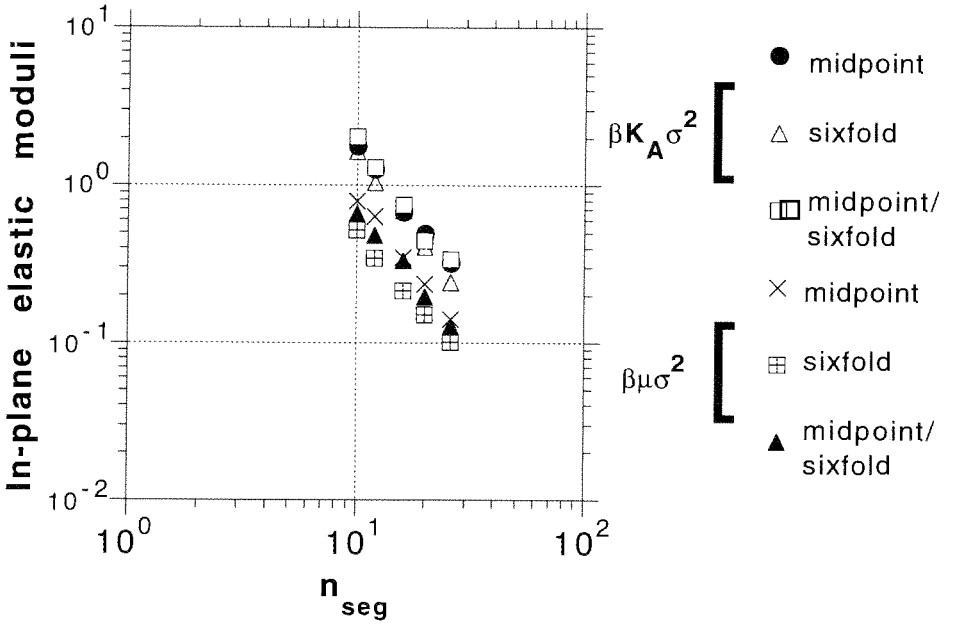

Fig. 5.7 The in-plane elastic moduli, K_A and μ as a function of n_{seg} for all cases. In cases II and III, the moduli are seen to decrease as n_{seg} increases, similar to case I.

The simulation predictions for the in-plane elastic moduli relevant to the human erythrocyte cytoskeletal network are shown in Table 5A.

Case	K_A (J/m^2)	μ (J/m^2)
I	1.8 x 10^{-5}	7.7 x 10^{-6}
II	1.6 x 10^{-5}	6.7 x 10^{-6}
III	2.2 x 10^{-5}	9.9 x 10^{-6}

Table 5A Comparison of the in-plane elastic moduli, K_A (area compressibility) and μ (shear modulus), for cases I, II and III, where n_{seg} and σ are selected in each individual case to model the human erythrocyte cytoskeletal network. The uncertainties in the predicted moduli are approximately 20%.

The first thing to notice from the data presented in Table 5A above is that the ratio K_A/μ is approximately equal to 2 for both cases II and III (much as in case I; see Chapter 2). This predicted value for the ratio has been verified experimentally for the human erythrocyte cytoskeleton (see Chapter 2). Thus, the simulation predicts that changing the membrane coupling mechanism of the network affects mostly the absolute magnitudes of the in-plane elastic moduli but not the ratio K_A/μ. The magnitudes of the moduli K_A and μ for both cases are also in agreement with the values measured in micropipette aspiration experiments (for K_A, see Evans and Waugh, 1977; for μ, see Evans *et. al.* , 1984).

The other piece of information that can be extracted from Table

5A is that the effect of switching the binding site from the midpoint (case I) to the sixfold junction (case II) is that the elastic moduli agree within statistical errors. On the other hand, if one were to bind the network to the bilayer at both the midpoints and sixfold junctions (case III), the moduli are found to be $\approx$ 22% larger for K_A and about 30% larger for μ (when compared to case I). This is consistent with the fact that the network in case III is displaced a lesser amount from the bilayer and, thus, the chains have less configuration space into which to unwind (due to steric interaction with the computational bilayer). Thus, the network in case III is expected to be more rigid than in cases I and II.

We now look at the dependence of the transverse or out-of-plane elastic moduli, K_V (volume compressibility) and $Y_\perp$ (transverse Young's modulus), on n_{seg}, which are shown in Fig. 5.8. In case II, the volume compression modulus is given approximately by

$$\beta K_V^{II} \sigma^3 \approx 1431 n_{seg}^{-2.85} \tag{5.11}$$

and, for the transverse Young's modulus,

$$\beta Y_\perp^{II} \sigma^3 \approx 96 n_{seg}^{-0.9} \tag{5.12}$$

and, for case III, we found that

$$\beta K_V^{III} \sigma^3 \approx 2566 n_{seg}^{-2.8} \tag{5.13}$$

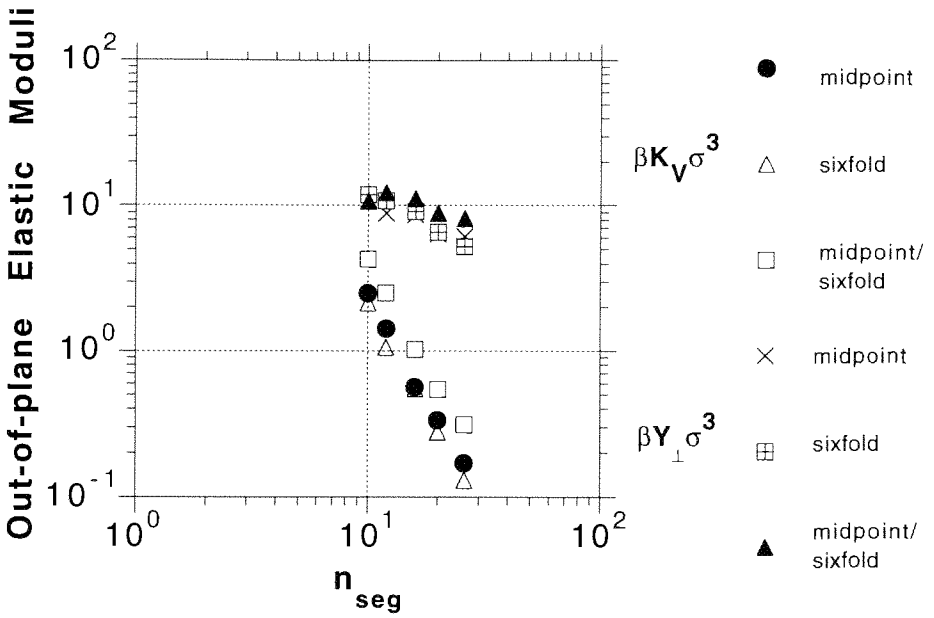

Fig. 5.8 The out-of-plane elastic moduli, K_V and $Y_\perp$ as a function of n_{seg}. The plot shows that the network in case III is somewhat stiffer in the transverse direction as compared to cases I and II.

$$\beta Y_\perp^{III} \sigma^3 \approx 29 n_{seg}^{-0.4}. \qquad (5.14)$$

As in Table 5A, the transverse elastic properties of the human RBC cytoskeleton can be extracted from fluctuations and are shown in Table 5B below. It is clear from Table 5B that the network in case III is significantly more rigid in the transverse direction, as compared to cases I and II. We find that K_V^{III} is roughly twice the value of K_V^{I} and $Y_\perp^{III}$ is roughly 2.5 times the value of $Y_\perp^{I}$. This difference is, again, attributable to the fact that the chains in case III are close to the computational bilayer and, hence, resist strongly the stresses applied

vertically to the network because of sterics. (See Chapter 2 for discussion on the significance of the large values extracted for $Y_\perp$).

Case	K_V (J/m^3)	$Y_\perp$ (J/m^3)
I	1.4 x 10^3	8.7 x 10^4
II	1.2 x 10^3	6.7 x 10^4
III	2.6 x 10^3	2.3 x 10^5

Table 5B Comparison of the out-of-plane elastic moduli, K_V (volume compressibility) and $Y_\perp$ (transverse Young's modulus), for cases I, II and III, where n_{seg} and σ are selected in each individual case to model the human erythrocyte cytoskeletal network. The uncertainties in the moduli are about 20%.

5.4 Effects on barrier-free paths of proteins

In Secs. 5.2 and 5.3, we looked at how various cytoskeleton/bilayer coupling mechanisms affect the geometry and elasticity of the network. In this section, we study how incorporating different network/bilayer coupling mechanisms would affect the barrier-free paths of computational "proteins" randomly inserted in the network.

Except for some changes of the location of the binding sites of the network, the simulation carried out in this investigation is similar to the one described in Chapter 4. That is, a hemispherical protein is

randomly placed inside a reference network and given a preselected random direction along which it is to be dragged. The reference configuration, although spatially fixed, is sufficiently large so that it provides a representative sample of cytoskeleton configurations. The protein interacts sterically with elements of the network and is deemed to be stopped in its track when the total force (arising from the network) acting on the protein is greater than or equal to the dragging force F_0. The results for cases II and III will be presented separately and compared.

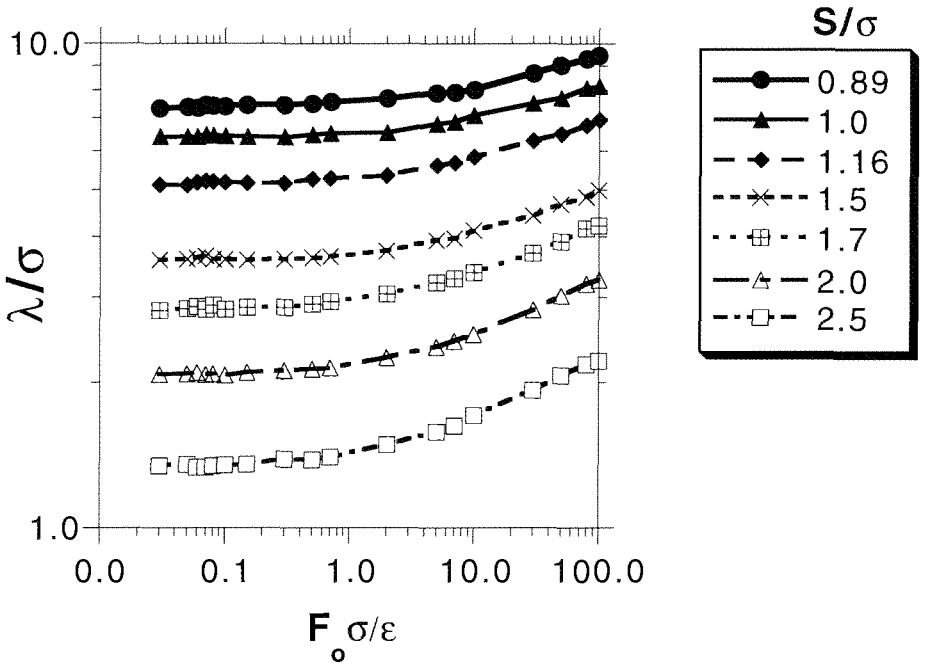

Fig. 5.9 Plot showing the variation of the mean path length of the dragged protein with the dragging force F_0 for case II. At small forces, there is little change in the mean path length, while at large forces, the mean path length increases monotonically.

First, we look at case II, where the cytoskeleton is coupled to the bilayer at the sixfold junctions (band 4.1). The variation with F_o of the mean paths of the computational protein is shown in Fig. 5.9. The mean paths are slightly larger than those observed in case I but are still in the 10-50 nm range (given that σ = 6.4 nm). At small values of F_o, there is little change in the mean path λ; but, beyond some threshold value $F_o \approx 0.1\ \sigma/\varepsilon$, λ increases monotonically. These observed characteristics of directed protein motion are very similar to those seen in case I.

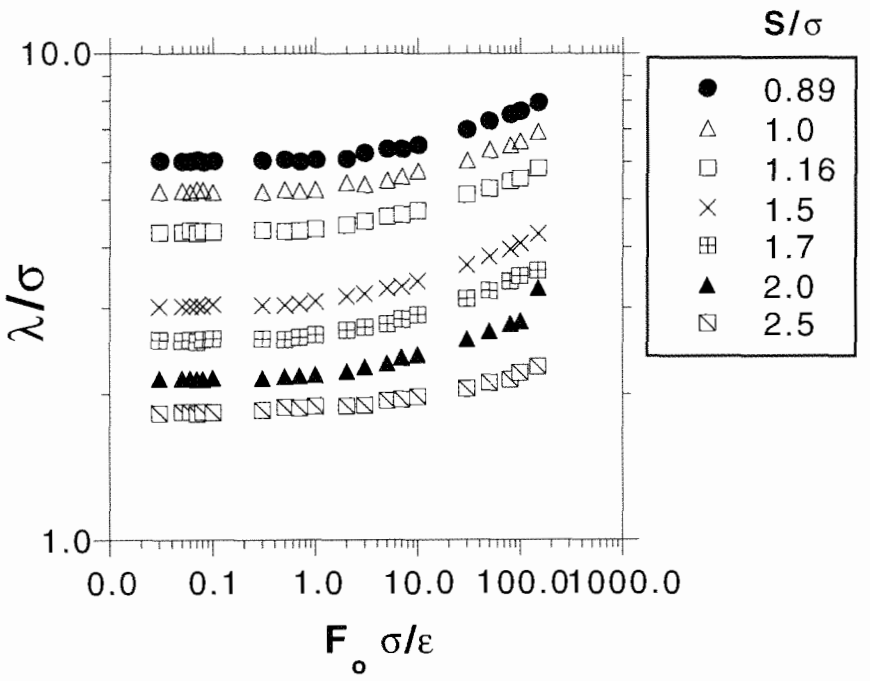

Fig. 5.10 Plot showing the variation of the mean path length of the dragged protein with the dragging force F_o for case III. There is little difference in the qualitative features but the mean-free paths are quantitatively smaller than in cases I and II when the physical value of σ is taken into account.

Now consider case III in Fig. 5.10. The first thing to notice in Fig. 5.10 is that λ/σ is larger than in cases I and II. However, since σ is smaller in case III (when converted to nanometers), λ is actually smaller than it is in the other two cases. In fact, the range of values for λ is around 9–30 nm. This is reasonable, if we recall that the network in case III has a smaller mean displacement from the bilayer $<t>$ and, hence, the steric hindrance to the directed motion of the computational protein is increased. In addition, the computational protein in case III encounters more in-plane obstacles (attachment sites). Another thing to notice in Fig. 5.10 is that the threshold force F_0, beyond which λ increases monotonically, is larger than in case I and is approximately equal to 1.0 σ/ε. This, again, reflects the tight coupling of the network to the computational bilayer and the smaller $<t>$ in case III, which results in a larger dragging force required to move the protein through the network.

The barrier-free path length L for the three cases was extracted and plotted against the parameter S, which is a measure of the protein size (for a description of the method of extraction for the barrier-free path L and the simulation parameters used, see Chapter 4). Fig. 5.11 shows this comparison on a log-log plot. The scaling behavior for case II is given by

$$L/\sigma = 6.5\ (S/\sigma)^{-1.5}, \tag{5.15}$$

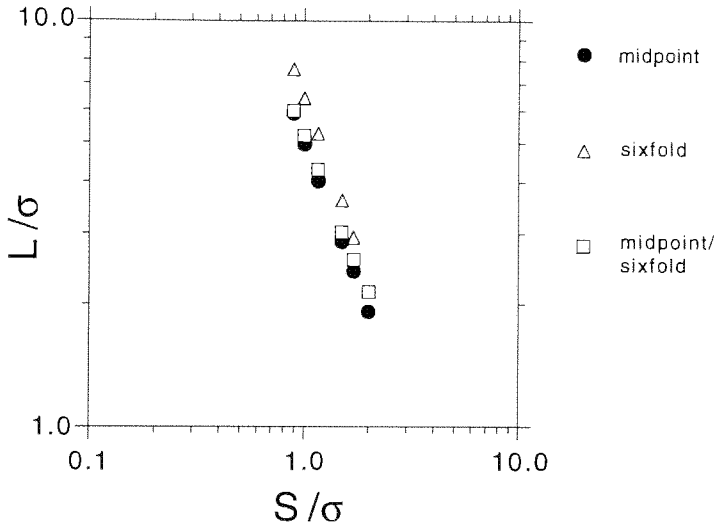

Fig. 5.11 Plot showing the variation of the barrier-free path L with S, which is a measure of the size of the computational protein. The three cases show similar behavior, that is, as S increases, L decreases like a power law.

and, for case III,

$$L/\sigma = 5.2\ (S/\sigma)^{-1.3}. \tag{5.16}$$

Fig. 5.11 shows that, in general, the barrier-free path L for case II is larger than for cases I and III, as expected. This is mainly due to the smaller number of attachment sites encountered by the protein in case II. This is consistent with Chapter 4, where we observed that the stopping points for the protein tend to be at the attachment sites.

The differences in barrier-free paths for the three cases are further seen in Fig. 5.12, which is a plot of $L+R_E$ versus R_E. The first thing to notice is that, in both cases II and III, $L+R_E$ decreases as R_E

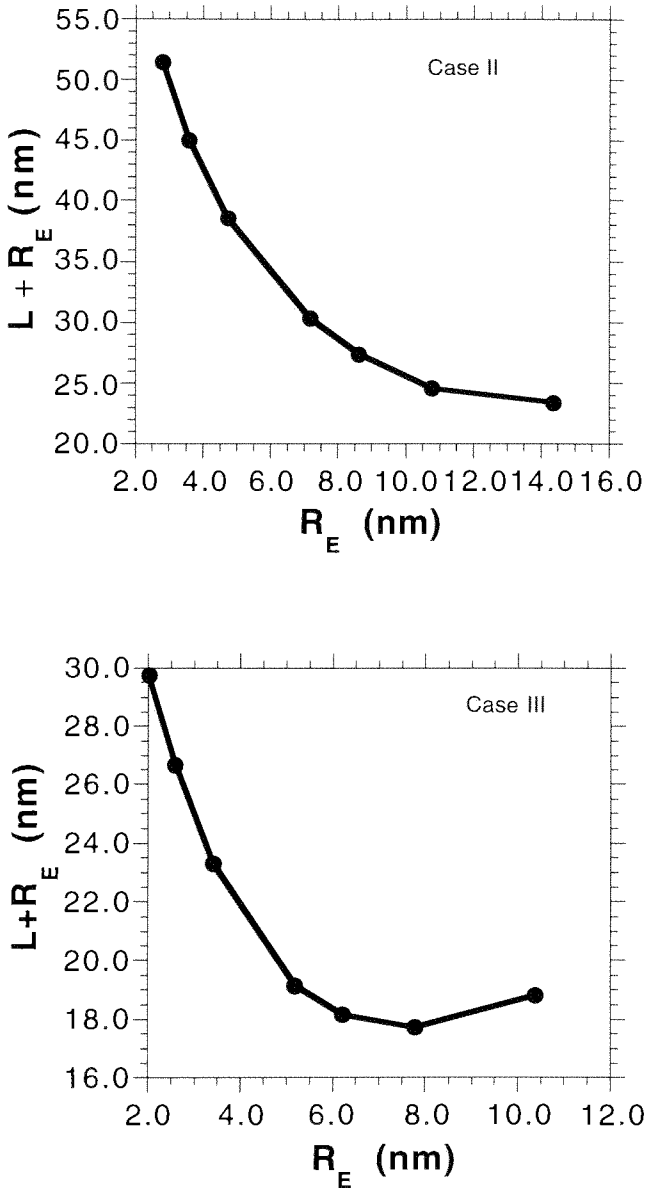

Fig. 5.12 L_e+R_e as a function of R_e for cases II and III. Notice that the two graphs have the same downward sloping trend for L_e+R_e. The corral size is clearly smaller in case III than in case II.

increases, dropping to some minimum value, which occurs when the protein is corraled (similar to case I, see Chapter 4). The difference

comes in the minimum value of $L+R_E$: (a) Case II, $(L+R_E)_{min} \approx 23$ nm, which is in agreement with that observed in case I (see Chapter 4). (b) Case III, $(L+R_E)_{min} \approx 18$ nm. This slight difference is mainly due to the smaller $<t>$ in case III (less chance of larger proteins slipping under the chains) and in a small part due to the larger diameter of the attachment sites (extracted later on in this section).

The corraling effect in case III is also seen to occur at a much smaller protein radius as compared to cases I and II. This can be understood in the following way. Recall Fig. 5.6(a), which was a schematic representation of the situation in cases I and II, and Fig. 5.6(b) for case III. The fluctuations of the displacement of the chains above the bilayer is larger in cases I and II than in case III, which is confirmed by the predicted mean displacement of the network. This in turn means that the computational protein in cases I and II, on average, slips under "fences" or chains more readily and, hence, leads to a larger BFP (and also to a larger mean corral size), as compared to case III. The smaller number of in-plane obstacles (attachment points) in cases I and II also contributes to the observed difference from case III.

We now turn to look at the effect of different membrane coupling mechanisms on the predicted size of the in-plane obstacles (attachment sites). Fig. 5.13 shows a plot of $1/L$ versus R_E for case II and III. From extrapolating $1/L$ by having $R_E \rightarrow 0$, as described in Chapter 4, we find for case II that $L_o \approx 132$ nm and for case III $L_o \approx 65$ nm. The values of L_o allow us to predict the effective

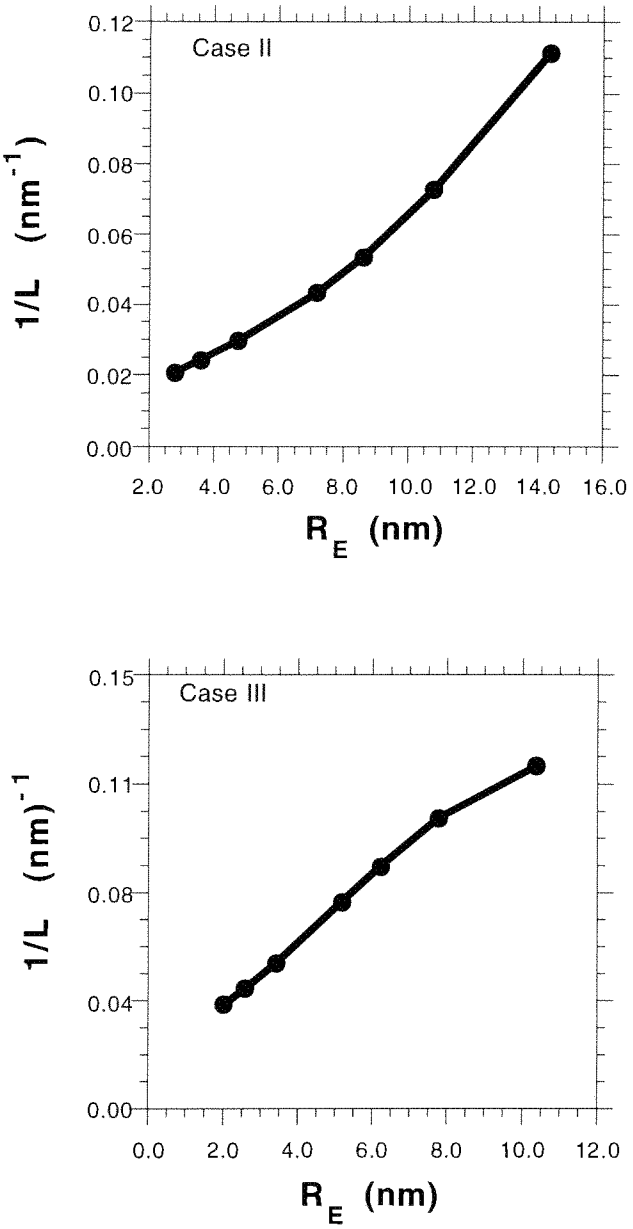

Fig. 5.13 Plot of $1/L$ versus R_E for cases II and III. The limiting value of $1/L$ is obtained by extrapolating R_E to zero.

diameters of in-plane obstacles.

Case II. The area density of attachment points $\rho_{II} = (2/\sqrt{3})/b^2$,

where b is the average end-end distance of the spectrin chain, taken to be 70 nm. This yields for the effective diameter of the attachment site $D_{II} \approx$ 32 nm. This is more than twice the value predicted in case I. Since we are dealing with proteins with infinitesimal radii, the mean displacement of the network is not a factor affecting the BFPs of the protein. It is, rather, the attachment site which is the major factor here. The much larger diameter of the in-plane junction site can be understood in the following way. Since there are six nearest neighbours for each sixfold junction complex, the effective steric barrier around a sixfold junction complex extends further along the bilayer plane than in case I for the midpoint attachment site, which has only two nearest neighbours.

Case III. Here, the density is $\rho_{III} = (8/\sqrt{3})/b^2$ and, thus, $D_{III} \approx$ 16 nm. This value for the diameter is intermediate between that of cases I and II. In case III, there are two types of attachment sites involved in coupling the network to the bilayer; 75% of the total number of attachment sites are chain midpoints, while the remaining 25% are sixfold junctions. Taking this into account, one can obtain an estimate of D_{III} in the following way:

$$\begin{aligned} D_{III} &= 0.75D_I + 0.25D_{II} \\ &\approx 0.75(12 \text{ nm}) + 0.25(32 \text{ nm}) \\ &\approx 17 \text{ nm} \end{aligned} \tag{5.17}$$

This estimate for D_{III} is in agreement with the value obtained in the

simulation and is, thus, a self-consistency check on the simulations. What D_{III} tells us here is that the computational protein sees an environment of scattering centers (attachment sites) which reflects the weighted average of the diameters of each type of scattering center present.

5.5 Summary

In this chapter we looked at the effects on the geometry and elasticity of the network of having different cytoskeleton/membrane coupling mechanisms. In Sec. 5.1, we found that the mean network area per junction vertex $<A_j>$ is unchanged when the attachment site is simply switched from the chain midpoint (case I) to the sixfold junction complex (case II). The mean displacement above the bilayer $<t>$ is also unchanged and is predicted to be approximately equal to 17 nm. On the other hand, when the network is attached at both the midpoints and sixfold junctions (case III), $<A_j>$ is larger than in cases I and II for a fixed value of n_{seg}, and $<t>$ falls to 8.5 nm.

The in-plane elastic moduli K_A (area compressibility) and μ (shear modulus) for case II are found not to differ significantly from that of case I; while, in case III, the moduli are found to be significantly larger than in case I. This effect is confirmed by the measurement of the out-of-plane moduli, K_V (volume compressibility) and $Y_\perp$ (transverse Young's modulus). It was found that K_V^{III} is approximately twice that of K_V^{I} and that $Y_\perp^{III}$ is about 2.5

times that of $Y_{\perp}^{I}$. It is proposed that a marked increase in the number of membrane linkages leads to an increase in membrane cytoskeletal rigidity.

We also investigated how alternate membrane coupling mechanisms affect the barrier-free paths of proteins in a directed-motion simulation. The barrier free paths and the sizes of the corrals for case I and case II are found to be in close agreement with each other. On the other hand, the predicted diameter of the attachment site for case II is more than twice that of the attachment site in case I. The predictions for case III are as expected: (1) BFPs are smaller, in the 10-30 nm range. (2) Corral size is also smaller, diameter $\approx$ 18 nm. (3) The effective diameter of the attachment sites (as "seen" by the computational protein) lies somewhere between that of cases I and II, near 16 nm. This is in agreement with estimate ($\approx$ 17 nm) obtained through a calculation which uses a weighted average of the mean diameters of the attachment sites of cases I and II. These effects as described are due mainly to the different number and location of the linkages of the membrane to the bilayer.

Chapter 6
CONCLUSION

6.1 Elasticity and geometry of the erythrocyte cytoskeleton

This research has been focused on the study of two main properties of the RBC membrane cytoskeleton, namely, geometry and elasticity. The cytoskeleton has been modeled as a triangulated network of polymer chains attached to the computational xy plane representing the lipid bilayer. Several mechanisms were investigated for attachment of the cytoskeleton to the bilayer; we placed the greatest emphasis on a reference model in which the attachment is at the midpoint of the polymer chains, representing the ankyrin junctions (referred to as case I). The different attachment mechanisms that were considered are summarised in Table 6A below.

Case I	Attachment through the midpoints of the polymer chains.
Case II	Attachment through the sixfold junction complexes.
Case III	Attachment through both the chain midpoints and the sixfold junction complexes.

Table 6A. The three different cytoskeleton/membrane attachment mechanisms investigated in our simulations.

Each polymer chain in our model network has n_{seg} segments between the sixfold junctions. The range $14 \leq n_{seg} \leq 32$ was investigated here.

We consider first the attachment of the network to the bilayer at the chain midpoint, namely case I. The polymer chains in the rest-state network are observed to be highly convoluted in the space above the computational bilayer, as expected from their highly flexible nature. This is consistent with experimental observations of spectrin tetramers in intact red cell cytoskeletons. Using the measured spectrin contour length and the experimental observation that the ratio of A_c (contour area per junction vertex) to $<A_j>$ (average area per junction vertex) is approximately seven, we are able to fix n_{seg} and the length of each segment in the chain. With the two model parameters fixed, the model then makes absolute predictions for the elastic constants and geometry of the cytoskeleton. For example, we predict the mean thickness of the cytoskeleton to be approximately equal to 32 nm, a prediction for which there is currently no experimental data available for comparison.

When the model network is placed under both isotropic compression and tension, $<A_j>$ is "S"-like in appearance as a function of the applied stress, flattening out at large tensions and compressions. At large tensions, the response of the model network is found to be approximated reasonably well by a network of equilateral triangles with inter-nodal square-well interactions. Near

zero stress, we observe that the response of the network is analogous to that of a two-dimensional network of springs with an effective spring constant $\beta k_{eff} s_0^2 = 32$, which is a large value, corresponding to small fluctuations in the interjunction spacings. This implies that the model cytoskeleton behaves like a low-temperature network of nodes near zero stress. Full-scale models, using a triangular two-dimensional network of nodes with two- and three-body interactions, will be used in future studies to simulate the micropipette aspiration experiments on red cells and, thus, to achieve a deeper understanding of the RBC elastic response.

Near zero stress, the ratio of the compression modulus K_A to the shear modulus μ in case I is $\approx 2.4 \pm 10\%$, which is in agreement with known experimental data from micropipette aspirations of red cells. Furthermore, the normalised in-plane elastic moduli, $\beta K_A \langle A_j \rangle$ and $\beta \mu \langle A_j \rangle$ (Waugh and Evans, 1979) are also in approximate agreement with one set of experimental measurements. Both K_A and μ increase under tension, which is expected on the basis of the built-in tether constraints in the model. The Poisson ratio is found to decrease monotonically under tension, becomes negative (very weakly) at modest tension, and then increases again at large tensions. This phenomenon of a negative Poisson ratio has also been observed in computer simulations of two-dimensional networks of springs under tension (Boal *et al.*, 1993).

The out-of-plane response (in all three cases), indicated by the volume compressibility and transverse Young's modulus, is found to

be significantly stiffer with the smooth BKF potential of our model compared to those observed in bead-and-tether model simulations utilising square-well potentials. The "quenched" out-of-plane fluctuations in a mixed microcanonical/canonical ensemble (used in our simulations) seems to be the cause of the transverse Young's modulus being one order of magnitude larger than the volume compressibility; this is not observed in pure MC simulations (private communications with Boal, 1997).

Attaching the model network to the computational bilayer through the sixfold junctions (case II), instead of the midpoint of the chains, did not alter the response of the network signficantly. In fact, the elastic moduli decreased only slightly, while the geometrical response was almost unchanged (mean displacement $\approx$ 16 nm). When the network was attached at both the chains' midpoints and the sixfold junctions (case III), the scaling behaviour of the geometrical observables (for example, $<A_j>$ and network displacment) are very similar to those of cases I and II, while the elastic moduli are significantly stiffer. The network in case III also lies closest to the computational bilayer (mean displacement $\approx$ 8.5 nm).

Under uniaxial tensions, the network is found to respond anisotropically (in all three cases). That is, the strain response of the network in the x-direction for a uniaxial stress in the x-direction is not the same as that for the corresponding situation along the y-direction. This behavior arises from the inequivalent geometry along

perpendicular axes drawn through the network. On the other hand, the network behaves much like that of a two-dimensional network of springs at small uniaxial tensions with an effective spring constant k_{eff} which is essentially the same as that extracted from isotropic stress tests described earlier. The Poisson ratio, in the limit that the tension goes to zero, has a value of 1/3, consistent with that expected from a two-dimensional network of springs at zero temperature.

The possibility of a built-in precompression (or prestress) in the rest-state of the RBC cytoskeleton has also been probed. We found that geometrical and elastic responses of the network modified by a prestress is very similar to those without a prestress, once the results are converted to physical units.

Some of the ingredients that were left out in our model which might be important to the complete description of the physical cytoskeleton, include: (1) spectrin-lipid binding at points other than the ones investigated (Everaers *et. al.*, 1996); (2) ionic interactions between spectrin chains (Stokke *et. al.*, 1986); (3). geometric irregularities in the coordination number and the possible existence of spectrin hexamers (Steck, 1989); (4) association-dissociation equilibrium states between tetramers and dimers (Tsuji *et. al.*, 1988).

6.2 Barrier-free paths

The other part of this research involved studying the effects of the network on the path lengths for directed motion of objects embedded in the computational bilayer, which is analogous to experiments in which proteins are dragged through the membrane via a laser-trapping device.

The simulations showed that small "proteins" have significantly larger barrier-free path lengths than large proteins, which are generally corralled (locally restrained) by the polymer chains. This is true for all of cases I, II and III; but, the barrier-free paths in case III are the smallest among the three cases. We also found that knowing the barrier-free paths of small proteins allowed the extraction of the mean diameter of an attachment point, when the directed motion of the protein is interpreted as a scattering mean free path. On the other hand, the directed motion of large proteins provides information about the size of the corrals (regions in which the cytoskeleton restricts protein movement).

Overall, the simulations provide a model in the context of which to probe the geometry and elasticity of biological membrane systems. Further refinements, such as inclusion of hydrodynamic effects and dynamic bilayer-cytoskeleton detachment/re-attachment processes, which are beyond the scope of this current research, can be added to study the effects of a dynamically fluctuating

cytoskeletal network on the diffusion properties of membrane proteins.

Appendix A: Effective spring constant of an ideal polymer chain

In three dimensions, the distribution function $p(r_{ee})$ for the end-to-end distance r_{ee} of an ideal polymer chain (that is, a chain without self-avoidance) is gaussian in shape and is given by

$$p(r_{ee}) \sim \exp\left(-3r_{ee}^2/(2n_{seg}b^2)\right), \tag{A.1}$$

where n_{seg} represents the number of segments of the chain and b is the average bond length of each segment. Note that $p(r_{ee})$ can also be written as

$$p(r_{ee}) = \frac{\Omega(r_{ee})}{\left(\sum_{r_{ee}} \Omega(r_{ee})\right)}, \tag{A.2}$$

where $\Omega(r_{ee})$ is the number of distinct configurations with end-to-end distance r_{ee}. The entropy S_E of the chain associated with this distribution is

$$S_E = k_B \ln[\Omega(r_{ee})], \tag{A.3}$$

which, when combined with Eq. (A.2), gives

$$S_E = S_o - 3k_B r_{ee}^2/(2(n_{seg}b)^2), \qquad (A.4)$$

where S_o is a constant. The free energy $F(r_{ee})$ of the chain, at a fixed value of r_{ee}, is related to S_E by

$$F(r_{ee}) = E - TS_E \qquad (A.5)$$

where E, the chain energy, is assumed to be a constant, independent of chain conformation. Putting Eq. (A.4) into Eq. (A.5), we get,

$$F(r_{ee}) = F_o + 3(k_B T)r_{ee}^2/(2(n_{seg}b)^2), \qquad (A.6)$$

where all constant terms are absorbed into F_o. Now, taking the derivative $-\partial F/\partial r_{ee}$ (with respect to r_{ee}) of the free energy in Eq. (A.6), of the chain gives us the entropic force f that acts on the chain. That is,

$$(\partial F/\partial r_{ee}) = k_{eff} \bullet r_{ee}, \qquad (A.7)$$

where the effective spring constant k_{eff} is, according to Eq. (A.6),

$$k_{eff} = 3k_B T/(n_{seg}b)^2. \qquad (A.8)$$

Appendix B: Normalised shear modulus for a network of ideal polymer chains

Consider an ideal chain with n_{seg} segments (or $n_{seg}+1$ vertices) with an average bond length b. From the discussion in Appendix A, we know that such a chain resists stretching with an effective spring constant k_{eff} of

$$\beta k_{eff} = 3/(n_{seg}b)^2 \qquad \text{(B.1)}$$

where β is the inverse temperature $(k_B T)^{-1}$ and k_{eff} is the effective spring constant of the ideal chain. The end-to-end distance $<r_{ee}>$ is related to n_{seg} by

$$<r_{ee}>^2 = b^2 n_{seg} \qquad \text{(B.2)}$$

(see Doi and Edwards, 1978), so

$$\beta k_{eff} = 3/<r_{ee}>^2. \qquad \text{(B.3)}$$

The shear modulus μ for a triangulated network at zero temperature and stress is related to k_{eff} (Boal *et. al.*, 1993) by

$$\mu = (\sqrt{3}/4)k_{eff}. \qquad \text{(B.4)}$$

Combining Eqs (B.3) and (B.4), we find

$$\beta\mu = 3\sqrt{3}/(4\langle r_{ee}\rangle^2). \tag{B.5}$$

The area A_j per junction vertex of a triangulated network is given by

$$A_j = (\sqrt{3}/2)\langle r_{ee}\rangle^2, \tag{B.6}$$

so that

$$\beta\mu = 9/(8A_j). \tag{B.7}$$

Replacing A_j^{-1} by ρ_{density}, which is the number of network nodes (sixfold junctions) per unit area, we get

$$\mu \approx \rho_{\text{density}} k_B T. \tag{B.8}$$

We note the similarity between this expression and the volumetric compression modulus $K_V = \rho k_B T$ of an ideal gas.

Appendix C: Derivation of Eq. (3.5)

Consider a two-dimensional triangulated network with square-well interactions between the nodes. In the mean field approach, or at large applied tension, the network triangles are approximately equilateral. A plaquette consisting of two adjacent equilateral triangles with sides s (containing a single vertex) has an area per junction vertex $A_j = (\sqrt{3}/2)s^2$, and a maximum area per junction vertex $A_m = (\sqrt{3}/2)s_m^2$, where $0 \le s \le s_m$. The mean area of a plaquette $<A>$ is given by

$$< A > = \frac{\int_0^{A_m} A\, e^{-\beta P A}\, dA}{\int_0^{A_m} e^{-\beta P A}\, dA} . \qquad \text{(C.1)}$$

The denominator of Eq. (C.1) can be evaluated as

$$\begin{aligned} \int_0^{A_m} e^{-\beta P A}\, dA &= \frac{-1}{\beta P}\int_0^{-\beta P A_m} e^{x}\, dx \\ &= \frac{-1}{\beta P}\left(e^{-\beta P A_m} - 1\right) . \end{aligned} \qquad \text{(C.2)}$$

The numerator of Eq. (C.1) is calculated to be

$$\begin{aligned}\int_0^{A_m} A\, e^{-\beta PA}\, dA &= \frac{1}{(\beta P)^2}\int_0^{-\beta PA_m} x e^{x}\, dx \\ &= \frac{1}{(\beta P)^2}\left[(-\beta PA_m)e^{-\beta PA_m} - e^{-\beta PA_m} + 1\right] .\end{aligned} \tag{C.3}$$

Combining the results in Eqs. (C.2) and (C.3), we arrive at the general formula for $<A>$,

$$\begin{aligned}<A> &= \frac{1}{\beta P}\left[1 - \frac{\beta PA_m e^{-\beta PA_m}}{1 - e^{-\beta PA_m}}\right] \\ &= \frac{1}{\beta P}\left[1 + \frac{\beta PA_m}{1 - e^{\beta PA_m}}\right] .\end{aligned} \tag{C.4}$$

In the limit of large tensions, i.e., when P is large and negative, we arrive at the approximation,

$$<A> \approx \frac{1}{\beta P}\left[1 + \beta PA_m\right], \tag{C.5}$$

which is Eq. (3.5).

Appendix D: Fluctuation formulae for elastic moduli

The fluctuation formulae for the extraction of elastic moduli are as follows:

(a) In-plane area compressibility K_A:

$$\beta K_A = \langle A \rangle / (\langle A^2 \rangle - \langle A \rangle^2), \tag{D.1}$$

where $\langle A \rangle$ is the mean in-plane area of the network.

(b) Shear modulus μ :

We define the in-plane Young's moduli along the x-axis and y-axis, Y_x and Y_y respectively, as,

$$\beta Y_x = (\langle A \rangle (\langle L_x^2 \rangle / \langle L_y \rangle^2 - 1))^{-1} \tag{D.2}$$

$$\beta Y_y = (\langle A \rangle (\langle L_y^2 \rangle / \langle L_y \rangle^2 - 1))^{-1}. \tag{D.3}$$

where L_x and L_y are the simulation box lengths along the x and y directions respectively. We then define the mean in-plane Young's modulus $Y_M = (Y_x + Y_y)/2$ and the shear modulus is calculated from

$$\beta \mu = Y_M \bullet K_A / (4K_A - Y_M). \tag{D.4}$$

(c) The volume compressibility K_V:

$$\beta K_V = \langle V \rangle / (\langle V^2 \rangle - \langle V^2 \rangle). \tag{D.5}$$

where V is the volume of the network given by the product $A \bullet t$, and t is the configurational mean of the network displacement from the bilayer.

(d) The transverse Young's modulus $Y_\perp$:

$$\beta Y_\perp = (\langle t \rangle / (\langle t^2 \rangle - \langle t \rangle^2)) / \langle A \rangle. \tag{D.6}$$

(For a further review of the fluctuation formulae, see Boal, 1994).

Bibliography

Allen, M. P., and D. J. Tildesley 1987. Computer simulation of liquids. Oxford Science Publications. p. 80.

Anderson, R. A., and R. E. Lovrien 1984. Glycophorin is linked by band 4.1 protein to the human erythrocyte membrane skeleton. *Nature Lond.* 307:655-658.

Axelrod, D. 1983. Lateral motion of membrane proteins and biological function. *J. Membr. Biol.* 75:1-10.

Bennett, V. 1980. Spectrin-based membrane skeleton: a multipotential adaptor between plasma membrane and cytoplasm. *Physiol. Rev.* 70:1029-1065.

Bennett, V. 1985. The membrane skeleton of human erythrocytes and its implications for more complex cells. *Annu. Rev. Biochem.* 54:273-304.

Bennett[a], V., and P. J. Stenbuck 1980. Association between ankyrin and the cytoplasmic domain of band 3 isolated from the human erythrocyte membranes. *J. Biol. Chem.* 255:6424-6432.

Bennett[b], V., and P. J. Stenbuck 1979. Identification and partial purification of ankyrin, the high affinity membrane attachment site for human erythocyte spectrin. *J. Biol. Chem.* 254:2533-2541.

Bishop, M., M. H. Kalos, and H. L. Frisch. 1979. Molecular dynamics of polymeric systems. *J. Chem. Phys.* 70:1299-1304.

Boal, D. H. 1994. Computer Simulation of a model network for the erythrocyte cytoskeleton. *Biophys. J.* 67:521-529.

Boal, D.H., U. Seifert and J. C. Shillcock 1993. Negative Poisson ratio in two-dimensional networks under tension. *Phys. Rev. E* 48:4274-4283.

Boal, D. H., U. Seifert and A. Zilker 1992. Dual network model for red blood cell membranes. *Phys. Rev. Lett.* 69:3405-3408.

Branton, D., C. M. Cohen and J. Tyler 1981. Interaction of cytoskeletal proteins on the human erythrocyte membrane. *Cell* 24:24-32.

Byers, T. J., and D. Branton 1985. Visualization of the protein associations in the erythrocyte membrane skeleton. *Proc. Natl. Acad. Sci. U.S.A.* 82:6153-6157.

Canham, P. M. 1970. The minimum energy of bending as a possible explanation of the biconcave shape of the human red blood cell. *J. Theor. Biol.* 25:61.

Cherry, R. J. 1979. Rotational and lateral diffusion of membrane proteins. *Biochim. Biophys. Acta* 559:289-327.

de Gennes, P. G. 1979. Scaling concepts in polymer physics. Cornell University Press. Chapter 1.

de Gennes, P. G. and C. Taupin 1982. Microemulsions and the flexibility of oil/water interfaces. *J. Phys. Chem.* 86:2294-2304.

Discher, D., D. H. Boal and S. K. Boey 1997. Phase Transitions and anisotropic responses of planar triangular nets under large deformation. *Phys. Rev. E* (in press).

Discher, D., N. Mohandas and E. A. Evans 1994. Molecular maps of red cell deformation: hidden elasticity and *in situ* connectivity. *Science* 266:1032-1035.

Doi, M. and S. F. Edwards 1986. The theory of polymer dynamics. Oxford Science Publications. Chapter 1.

Edidin, M., S. C. Kuo and M. P. Sheetz. 1991. Lateral movements of membrane glycoproteins restricted by dynamic cytoplasmic barriers. *Science* 254:1379-1382.

Elgsaeter, A., B. T. Stokke, A. Mikkelsenand D. Branton 1986. The molecular basis of erythrocyte shape. *Science* 234:1217-1223.

Engelhardt, H. and E. Sackmann 1988. On the measurement of shear elastic moduli and viscosities of erythrocyte plasma membranes by transient deformation in high frequency electric fields. *Biophys. J.* 54:495-508.

Edidin, M., S. C. Kuo, and M. P. Sheetz. 1991. Lateral movements of membrane glycoproteins restricted by dynamic cytoplasmic barriers. *Science* 254: 1379-1382.

Evans, E. A. 1973. A new material concept for the red cell membrane. *Biophys. J.* 13:926-939.

Evans, E. and W. Rawicz 1990. Entropy-driven tension and bending elasticity in condensed-fluid membranes. *Phys. Rev. Lett.* 64:2094-2097.

Evans, E. A. and R. Skalak 1979. Mechanics and thermodynamics of biomembranes. *CRC Crit. Rev. Bioeng.* 3:181-418.

Evans, E., and R. M. Hochmuth 1978. Mechano-chemical properties of membranes. *Curr. Top. Membr. Transp.* 10:1-64.

Evans, E. and R. Waugh 1977. Osmotic correction to elastic area compressibility measurements on red cell membrane. *Biophys. J.* 20:307-313.

Evans, E. A., N. Mohandas and N. Leung 1984. Static and dynamic rigidities of normal and sickle erythrocytes. *J. Clin. Invest.* 73: 477-488.

Everaers, R., I. S. Graham, M. J. Zuckermann and E. Sackmann 1996. Entropic elasticity of end adsorbed polymer chains: The spectrin network of red blood cells as C^*-gel. *J. Chem. Phys.* 104:3774-3781.

Fairbanks, G., T. L. Steck and D. F. H. Wallach 1971. Electrophoretic analysis of the major polypeptides of the human erythrocyte membrane. *Biochemistry* 13:5514-5521.

Fowler, V. and V. Bennett 1978. Association of spectrin with its membrane attachment site restricts lateral mobility of human erythrocyte integral membrane proteins. *J. Supramol. Struct.* 8:215-221.

Fowler, V. M., and D. L. Taylor 1980. Spectrin plus band 4.1 cross-link actin. Regulation by micromolar calcium. *J. Cell. Biol.* 85:361-376.

Gennis, R. B. 1989. Biomembranes. Molecular Structure and function. Springer-Verlag. p. 91-93.

Ghosh, R. N., and W. W. Webb 1994. Automated detection and tracking of individual and clustered cell surface low density lipoprotein receptor molecules. *Biophys. J.* 66:1301-1318.

Gompper, G. and D. M. Kroll 1991. Fluctuations of a polymerized membrane between walls. *J. Phys. I France* 1:1411-1432.

Gross, D. and W. W. Webb 1986. Molecular counting of low-density lipoprotein particles as individuals and small clusters on cell surfaces. *Biophys. J.* 49:901-911.

Grest, G. S. and K. Kremer 1986. Molecular dynamics simulation for polymers in the presence of a heat bath. *Phys. Rev. A.* 33:3628-3631.

Hansen, J. C., R. Skalak, S. Chien and A. Hoger 1996. An elastic network model based on the structure of the red blood cell membrane skeleton. *Biophys. J.* 70:146-166.

Heuser, J. E. 1983. Procedure for freeze-drying molecules adsorbed to mica flakes. *J. Mol. Biol.* 169:155-195.

Hochmuth, R. M. 1987. Properties of red blood cells. *In* Handbook of Bioengineering. R. Skalak and S. Chien, editors.

Jacobson, K., E. Elson, D. Koppel and W. W. Webb 1982. Fluorescence photobleaching in cell biology. *Nature* 295:283-284.

Jacobson, K., A. Ishihara and R. Inman 1987. Lateral diffusion of proteins in membranes. *Annu. Rev. Physiol.* 49:163-175.

Johnson, R. M., G. Taylor and D. B. Meyer 1980. Shape and volume changes in erythrocyte ghosts and spectrin-actin networks. *J. Cell Biol.* 86:371-376.

Kantor, Y., M. Kardar and D. R. Nelson 1986. *Phys. Rev. Lett.* 57:791.

Kell, D. B. 1984. Diffusion of protein complexes in prokaryotic membranes: fast, free, random or directed? *Trends Biochem. Sci.* 9:86-88.

Krough, A. 1959. The Anatomy and Physiology of Capillaries, p. 8. New York: Hafner. 422pp.

Kusumi, A., Y. Sako, and M. Yamamoto. 1993. Confined lateral diffusion of membrane receptors as studied by single particle tracking (nanovid microscopy): effects of calcium-induced differentiation in cultured epithelial cells. *Biophys. J.* 65:2021-2040.

Lai, W. M., D. Rubin and E. Krempl 1987. Introduction to continuum mechanics. Pergamon Press. p. 122.

Landau, L. D., and E. M. Lifshitz 1968. Theory of Elasticity. Addison-Wesley. Chapter 1.

Lange, Y., R. A. Hadesman and T. L. Steck 1982. Role of the reticulum in the stability and shape of the isolated human erythrocyte membrane. *J. Cell Biol.* 92:714-721.

Le-Doussal, P., and L. Radzihovsky 1992. Self-consistent theory of polymerized membranes. *Phys. Rev. Lett.* 69:1209-1212.

Liu, S. C., L. H. Derick and J. Palek 1987. Visualization of the hexagonal lattice in the erythrocyte membrane skeleton. *J. Cell Biol.* 104:527-536.

Mohandas, N. and E. Evans 1994. Mechanical properties of the red cell membrane in relation to molecular structure and genetic defects. *Annu. Rev. Biophys. Biomol. Struct.* 23:787-818.

Mohandas, N and W. Groner 1989. Cell membrane and volume changes during red cell development and aging. *Ann. N.Y. Acad. Sci.* 554:217-224.

Mueller, T. J., and M. Morrison 1981. Glyco-connectin (PAS2), a membrane attachment site for the human erythrocyte cytoskeleton. In: *Erythrocyte Membranes 2: Recent Clinical and Experimental Advances*, edited by Kruckeberg W. C., J. W. Eaton and G. J. Brewer, New York:Liss, p. 95-112.

Nigg, E. A., and R. J. Cherry 1980. Anchorage of a band 3 population at the erythrocyte cytoplasmic membrane surface: protein rotational diffusion measurements. *Proc. Natl. Acad. Sci. USA.* 77:4702-4706.

Ohanian, V., L. Wolfe, K. John, J. Pinder, S. Lux and W. Gratzer 1984. Analysis of the ternary interaction of the red cell membrane skeletal proteins spectrin, actin and 4.1. *Biochemistry* 23:4416-4420.

O'shea, P. S. 1984. Lateral diffusion: the archipelago effect. *Trends Biochem. Sci.* 9:378.

Petersen, M. A., H. Strey and E. Sackmann 1992. Theoretical and phase contrast microscopic eigenmode analysis of erythrocyte flicker: amplitudes. *J Phys. II* (France) 2:1273-1285.

Pink, D. A. 1985. Protein lateral movement in lipid bilayers. Simulation studies of its dependence upon protein concentration. *Biochim. Biophys. Acta.* 818:200-204.

Poo, M.-M., and R. Cone. 1974. Lateral diffusion of rhodopsin in the photoreceptor membrane. *Nature* 247:438-441.

Reid, M., J. Chasis and N. Mohandas 1987. Identification of a functional role for human erythrocyte sialoglycoproteins beta and gamma. *Blood* 69:1068-1072.

Sackmann, E., H-P. Duwe and H. Engelhardt 1986. Membrane bending elasticity and its role for shape fluctuations and shape transformations of cells and vesicles. *Faraday Discuss. Chem. Soc.* 81:281-290.

Sako, Y., and A. Kusumi. 1994. Compartmentalized structure of the plasma membrane for receptor movements as revealed by a nanometer-level motion analysis. *J. Cell. Biol.* 125:1251-1264.

Sako, Y., and A. Kusumi. 1995. Barriers for lateral diffusion of transferrin receptors in the plasma membrane as characterized by receptor dragging by laser tweezers: fence vs. tether. *J. Cell Biol.* 129:1559-1574.

Saxton, M. J. 1982. Lateral diffusion in an archipelago. Effects of impermeable patches on diffusion in a cell membrane. *Biophys. J.* 39:165-173.

Saxton[a], M. J. 1989. The spectrin network as a barrier to lateral diffusion in erythrocytes. A percolation analysis. *Biophys. J.* 55:21-28.

Saxton[b], M. J. 1989. Lateral diffusion in an archipelago. Distance dependence on the diffusion coefficient. *Biophys. J.* 56:615-622.

Saxton, M. J. 1990. The membrane skeleton of erythrocytes: models of its effects on lateral diffusion. *Int. J. Biochem.* 22:801-809.

Saxton, M. J. 1995. Single-particle tracking: effects of corrals. *Biophys. J.* 389-398.

Schofield, A. E., M. J. A. Tanner, J. C. Pinder, B. Clough, P. M. Bayley, G. B. Nash, A. R. Dluzewski, D. M. Reardon, T. M. Cox, R. J. M. Wilson and W. B. Gratzer 1992. Basis of unique red cell membrane properties in hereditary ovalocytosis. *J. Mol. Biol.* 223:949-958.

Schmid-Schönbein, H., H. heidtmann and R. Grebe 1986. Spectrin, red cell shape and deformability. II. The antagonistic action of spectrin and sialic acid residues in determining membrane curvature in genetic spectrin deficiency in mice. *Blut.* 52:149-164.

Sheetz, M. P. 1983. Membrane skeletal dynamics: role in modulation of red cell deformability, mobility of transmembrane proteins, and shape. *Semin. Hemat.* 20:175-188.

Sheetz, M. P., M. Schindler, and D. E. Koppel. 1980. Lateral mobility of integral membrane proteins is increased in spherocytic erythrocytes. *Nature.* 285:510-512.

Steck., T. L. 1989. Red cell shape. *In* Cell shape: Determinants, Regulation and Regulatory Role. W. Stein and F. Bronner, editors. Academic Press, New York. 205-246.

Stokke[a], B. T., A. Mikkelsen and A. Elgsaeter 1986. The human erythrocyte membrane skeleton may be an ionic gel. III. Micropipette aspirations of unswollen erythrocytes. *J. Theor. Biol.* 123:205-211.

Stokke[b], B. T., A. Mikkelsen and A. Elgsaeter 1986. Some viscoelastic properties of human erythrocyte spectrin-actin networks end-linked in vitro. *Biochim. Biophys. Acta.* 816:111-119.

Strey, H., M. Peterson and E. Sackmann 1995. Measurement of erythrocyte membrane elasticity by flicker eigenmode decomposition. *Biophys. J.* 69:478-488.

Tsuji, A., K. Kawasaki, S. Ohnishi, H. Merkle and A. Kusumi. 1988. Regulation of band 3 mobilities in erythrocyte ghost membranes by protein association and cytoskeletal meshwork. *Biochemistry.* 27:7447-7452.

Ungewickell, E., P. M. Bennett, R. Calver, V. Ohanian and W. B. Gratzer 1979. In Vitro formation of a complex between cytoskeletal proteins of the human erythrocyte. *Nature Lond.* 380:811-814.

Waugh, R. and P. Agre 1988. Reductions of erythrocyte membrane viscoelastic coefficients reflect spectrin deficiencies in hereditary spherocytosis. *J. Clin. Invest.* 81:133-141.

Waugh, R. and E. A. Evans 1979. Thermoelasticity of red blood cell membrane. *Biophys. J.* 26:115-131.

Webb, W. W., L. S. Barak, D. W. Tank and E. S. Wu. 1982. Molecular mobility on the cell surface. *Biochem. Soc. Symp>* 46:191-205.

Wood, W. W. 1968. Monte Carlo calculations for hard disks in the isothermal-isobaric ensemble. *J. Chem. Phys.* 48:415-434.

Zhang, F., G. M. Lee, and K. Jacobson. 1993. Protein lateral mobility as a reflection of membrane microstructure. *BioEssays*. 15:579-588.

Zilker, A., M. Ziegler and E. Sackmann 1992. Spectral analysis of erythrocyte flickering in the $0.3-4-\mu m^{-1}$ regime by microinterferometry combined with fast image processing. *Phys. Rev.* A. 46:7998-8001.